University of Chicago

Doctoral Thesis

First EDM Measurement of Radium

Author:
Richard Haywood Parker

Supervisor:
Dr. Zheng-Tian Lu

A thesis submitted in fulfilment of the requirements
for the degree of Doctor of Philosophy

in the

Unversity of Chicago
Physics Department

July 2015

"Doubt is not a pleasant condition, but certainty is absurd."

Voltaire

UNIVERSITY OF CHICAGO

Abstract

Physics Department

Doctor of Philosophy

First EDM Measurement of Radium

by Richard Haywood Parker

The radioactive radium-225 (^{225}Ra) atom is a favorable case to search for a permanent electric dipole moment (EDM). Due to its strong nuclear octupole deformation and large atomic mass, ^{225}Ra is particularly sensitive to interactions in the nuclear medium that violate both time-reversal symmetry and parity. We have developed a cold-atom technique to study the spin precession of ^{225}Ra atoms held in an optical dipole trap, and demonstrated the principle of this method by completing the first measurement of its atomic EDM, reaching an upper limit of $|d(^{225}\mathrm{Ra})| < 5.0\times10^{-22}$ e·cm (95% confidence).
This work is supported by DOE, Office of Nuclear Physics (DE-AC02-06CH11357).

Acknowledgements

First and foremost I would like to thank my advisor Zheng-Tian Lu for allowing me to join the radium project and helping to guide me in my years as a graduate student. He has taught me a great deal, and provided me with many opportunities to go to conferences and give presentations. Prof. Lu was always optimistic the project would be successful, even when the rest of us were doubtful.

I would also like to thank Peter Mueller, whose technical expertise is astounding. On multiple occasions simply his presence in the lab was sufficient to fix a problem we had; and when it wasn't, he was always ready and able to help. I would also like to thank Roy Holt, who assisted us greatly in our vacuum improvements and who was always able to brighten up our weekly meetings. John Greene was absolutely invaluable to our experiment, helping us with every radium load and being very willing to work with us when there were problems.

Before officially working on the radium experiment I briefly worked with Brent Graner and Wolfgang Korsch building two Rb magnetometers for a later stage of the project. Brent and Wolfgang were both very patient with me when I still knew very little about AMO, and helped me get my "sea legs".

My first coworkers on the radium experiment were Will Trimble and Ibrahim Sulai. Will could always get us to laugh with his quirky sense of humor, but he also had a deep knowledge of quantum mechanics and was very willing to help me understand things. Ibrahim was the senior graduate student when I joined, and knew every knob in the lab. His advice on laser cooling and trapping radium form the core of my current knowledge of the experiment.

Kevin Bailey and Tom O'Connor are incredible engineers, designing our experiment with much greater skill than I ever could have. Whenever I needed something from them, whether it was a thermal control system for a fiber or a detailed diagram of our appratus to put in a talk, both Kevin and Tom were always very willing and eager to assist.

The second team I worked with was Matt Dietrich and Mukut Kalita. Matt has an impressive knowledge of physics and a clever mind; he came up with many ideas when were struggling to transfer atoms between two ODTs. Matt has been very helpful even after he left, regularly attending meetings by phone or assisting by email. Mukut worked with me until I graduated, and his work building a turn-key high-voltage electrode system and an upgraded beam fluorescence analysis code made all our lives much easier.

I only spent two years with Nathan Lemke, but he was a very fun person to have around, and very agreeable. I fondly remember his willingness to provide ice cream for

the graduate students when we needed it. Our current postdoc is Michael Bishof, and I thank him for working hard in the lab, especially at a time when I was too busy to be of much help. And I would like to thank Jaideep Singh, who figured out how to get one of our papers published. His work on our Labview timing software is directly responsible for our first observation of radium nuclear spin precession.

I would also like to thank David Potterveld, who helped us set up our "control room" and who worked hard on a detailed Monte Carlo simulation to diagnose problems in our trapping efficiency. Timothy Chupp deserves special recognition for doing the analysis to determine the impact of radium EDM experiments at a variety of sensitivities. I also thank Wei Jiang, who often helped me come up with ideas when we were having trouble.

I also acknowledge my thesis committee: Professors Cheng Chin, Ed Blucher, and Richard Hill for providing helpful feedback during the two meetings I had with them, and for taking the time to read my thesis.

Finally, I would like to thank my mother and father for their encouragement and support, especially when success wan't very certain. Zhijun has been immensely caring and understanding, especially when I working very long hours during the radium runs, and I am grateful for her love, strength, and faith in me. And I would like to thank MeToo, whose regular attempts to delete my thesis encouraged me to make many backups.

This work was supported by the Department of Energy.

Contents

List of Figures

List of Tables

Abbreviations

EDM	**E**lectric **D**ipole **M**oment
MOT	**M**agneto **O**ptical **T**rap
ODT	**O**ptical **D**ipole **T**rap
ULE	**U**ltra **L**ow **E**xpansion
PDH	**P**ound **D**rever **H**all
CP	**C**harge conjugation and **P**arity
CPT	**C**harge conjugation, **P**arity, and **T**ime reversal
MDM	**M**agnetic **D**ipole **M**oment
QCD	**Q**uantum **C**hromo **D**ynamics
UCN	**U**ltra **C**old **N**eutrons

Dedicated to Zhijun, whose strength and love made this thesis possible

Chapter 1

Introduction

Big things have small beginnings [1]. In physics, a few minor unexplained phenomena have the potential to completely change how we look at the universe. In Lord Kelvin's famous speech in 1900, he explained that all the physical laws governing the thermodynamics and energy of the universe were explained, except for two "dark clouds": the failure of the Michelson-Morley experiment to detect the luminous ether, and the ultraviolet catastrophe. These two "minor" issues would eventually give birth to General Relativity and Quantum Mechanics, respectively. Our current knowledge of the interactions of fundamental particles is encapsulated in the Standard Model, and as before we are well aware of the limitations of the theory − many mysteries exist, such as a suitable description of quantum gravity, the matter-antimatter asymmetry in the observed universe, and the strong CP problem. Experiments studying fundamental symmetries lie at the frontier of modern physics, hoping to yield the next leap in our understanding of the world around us.

This thesis describes one such experiment on fundamental symmetries, namely the search for a non-zero EDM. Chapters 1-3 will explain the motivation of EDM experiments, provide a brief explanation of how a general EDM measurement is performed, and detail the various advantages and disadvantages to attempting an EDM measurement with ^{225}Ra. Chapters 4-6 describe the experimental apparatus and procedure, both for laser cooling and trapping of ^{225}Ra, and using the trapped atoms for nuclear spin precession experiments. Chapters 7-9 report the results of the EDM measurement of ^{225}Ra, detailing

[1] Quote from Lawrence of Arabia

both the statistical and systematic uncertainties, and briefly explain the consequences of the experiment in the broader context of tests of fundamental symmetries. Finally, Chapter 10 presents five planned upgrades intended to improve the EDM sensitivity of the proof-of-principle experiment by many orders of magnitude.

This thesis is written to serve not just as an overview for the experiment, but partly as a manual for the next generation of scientists who will use the apparatus and improve it. The intent is to preserve some of the important institutional knowledge, by discussing not just our successes but also some of our failures. To this end, several computer programs are included in the appendices that were used in the first phase of the experiment, and may prove useful in the future.

Chapter 2

Motivation for EDM Experiments

This chapter details the motivation for EDM experiments; introducing fundamental symmetries and explaining the consequences of their violation. An overview of various EDM measurements is included at the end of the chapter to provide context for the reader.

2.1 Symmetry and Symmetry Violation

2.1.1 C Violation

Charge conjugation reverses the sign of all charges. This includes electric charge, lepton number, baryon number, and strangeness. A variable is said to conserve C-symmetry if the physical laws are invariant under application of the charge conjugation transformation. A particularly informative example is the photon, which has a charge parity of -1 because the charge conjugation operator reverses the sign of electric fields. In the Standard Model, electromagnetism, gravity, and the strong interaction all preserve charge conjugation symmetry, but C-symmetry is violated in the weak interaction. Application of the charge conjugation operator turns, for example, a left-handed neutrino into a left-handed anti-neutrino, as charge conjugation does not affect chirality. The weak interaction couples only left-handed particles and right-handed antiparticles, and therefore is said to "maximally violate" C-symmetry.

2.1.2 P Violation

A parity transformation is the reversal of sign of a spatial coordinate. In three dimensions, this transformation takes $x \to -x$, $y \to -y$, and $z \to -z$. A variable is said to be P-even or P-odd based on how it changes under application of the parity operator. Examples of P-even variables include time, mass, energy, magnetic field, and angular momentum, while examples of P-odd variables include position, velocity, acceleration, force, electric field, helicity, and the Poynting vector. To determine the parity of electric dipole moments, the topic of this thesis, we consider the Hamiltonian for the interaction of an EDM with an electric field:

$$H_{EDM} = -\vec{d} \cdot \vec{E} = -\frac{d}{J} \vec{J} \cdot \vec{E} \tag{2.1}$$

where $d = |\vec{d}|$ and $J = |\vec{J}|$. The electric field is odd under parity, and the angular momentum is even, so the EDM is odd under parity. To see why EDMs violate parity symmetry (which is not the same thing as being parity odd), we consider a particle with an EDM parallel to the particle's magnetic dipole moment (MDM). If we apply the parity operator, the MDM will be unaffected, but the EDM will reverse in direction. Therefore the two vectors are now antiparallel, and we can use the relative sign of the EDM and MDM to determine whether or not the parity operator has been applied. Thus EDMs violate parity symmetry.

In the Standard Model, parity is conserved in electromagnetism, gravity, and the strong interaction. In the 1950's the suggestion was made by Lee and Yang to test parity violation in the weak interaction. The proposal was taken up by C. S. Wu, and in 1957 the group found the first clear evidence of parity violation [1]. The experiment studied the beta decay from polarized Cobalt-60 nuclei, and found an assymetry between decays parallel and anti-parallel to the nuclear spin. Although Wu wished to keep the results private until the group was ready, the results were nonetheless revealed to the Columbia physics department. A group composed of R. L. Garwin, L. Lederman, and R. Weinrich rapidly performed a measurement of meson decays and found similar results [2]. The two papers were published in the same journal.

2.1.3 CP Violation

CP refers to the simultaneous application of charge conjugation and parity. After the discovery of parity violation in 1957 described above, it was proposed by Lev Landau [3] that CP is the actual conserved symmetry of the universe. The first discovery of CP violation was found in 1964 in the decay of neutral kaons [4]. Neutral kaons, with $K^0 = d\bar{s}$ and $\bar{K}^0 = s\bar{d}$ where d is the down quark and s is the strange quark, can be considered in terms of two eigenstates of CP, K_1 with $CP = +1$ and K_2 with $CP = -1$:

$$|K_1\rangle = \frac{|K^0\rangle - |\bar{K}^0\rangle}{\sqrt{2}} \quad , \quad |K_2\rangle = \frac{|K^0\rangle + |\bar{K}^0\rangle}{\sqrt{2}} \tag{2.2}$$

$$CP\,|K_1\rangle = |K_1\rangle \quad , \quad CP\,|K_2\rangle = -\,|K_2\rangle \tag{2.3}$$

The two eigenstates are called K_S (K-short) and K_L (K-long), and if CP symmetry holds then $K_S = K_1$ and $K_L = K_2$. K_1 decays primarily into two pions, which is even under CP, and K_2 decays primarily into three pions, which is odd under CP. The experiment showed that these two states are not quite eigenstates; i.e. that $K_L = K_2 + \epsilon K_1$ and $K_S = K_1 + \epsilon K_2$. In particular, the group measured 45 ± 10 $K_2 \to \pi^+ + \pi^-$ decays of the 22,700 K_2 decays, about 0.2% [5]. This decay was said to be an indication of indirect CP violation because the violation was observed in the way the kaons mixed with each other, rather than in the way that they decayed, and therefore could be explained not by CP violation in the weak interaction but by some other force, termed "superweak". Direct CP violation in the decay of kaons into two pions was predicted to be much smaller, and was conclusively demonstrated in 1999 by the KTEV and NA48 experiments [6, 7]. Soon after, direct CP violation was also discovered in B meson decays [8, 9], and in 2011 CP violation was reported in D meson decays [10].

CP violation has important consequences for our current understanding of the universe. One issue is the observed matter-antimatter asymmetry in the universe; to create the observed imbalance the Sakharov conditions must be satisfied. One of those conditions is the existence of CP violation in the early universe. CP violation has been found in the quark sector, and may exist in the strong and lepton sectors as well, but too few mechanisms of CP violation are known at present to explain the observed matter-antimatter

asymmetry. There are theories that get around this issue, for example proposing that the matter-antimatter asymmetry happened to be the "initial condition" of our universe, but it remains an unsolved problem, and encourages researchers to search for new mechanisms of CP violation.

Another issue is that there is (at present) no experimental evidence of CP violation in quantum chromodynamics. As there is no known reason why CP-symmetry would be violated in the weak sector but not the strong sector, this is considered a "fine-tuning" issue and referred to as the Strong CP problem. Theories have been proposed to explain this, notably the Peccei-Quinn theory which posits axions as new scalar particles and allows the CP violation parameters in the QCD Lagrangian to be zero. However, without experimental data this remains an open question in modern particle physics.

2.1.4 T Violation

Time-reversal symmetry refers to the effect of time reversal on a given variable. T-even variables include position, acceleration, force, and electric field, while T-odd variables include velocity, linear and angular momentum, and magnetic field. To determine the behavior of electric dipole moments under time reversal, we again consider the Hamiltonian for the interaction of an EDM with an electric field:

$$H_{EDM} = -\vec{d} \cdot \vec{E} = -\frac{d}{J}\vec{J} \cdot \vec{E} \tag{2.4}$$

The electric field is even under time reversal, while the angular momentum is odd, so EDMs are T-odd. To see why EDMs violate time-reversal symmetry, we again consider a particle with an EDM parallel to the particle's magnetic dipole moment (MDM). If we apply the time reversal operator, the MDM will be reverse in direction, but the EDM will be unaffected. As in the parity case, the two vectors are now antiparallel, thus EDMs violate time reversal symmetry.

Note that an induced EDM, for example the one a water molecule gets when an external electric fied is applied, does not violate T-symmetry. Direct T-violation (distinct from CP violation) has been measured in the decays of kaons and B mesons [11, 12].

2.1.5 CPT Violation

The simultaneous application of charge-conjugation, parity, and time-reversal operators is known as CPT symmetry. Unlike each of the previously discussed symmetries, CPT is a consequence of Quantum Field Theory. The CPT theorem relies on the assumption that both the theory is Lorentz invariant and the vacuum is Lorentz invariant, and therefore tests of Lorentz violation are often related to tests of CPT symmetry. To date CPT symmetry remains a "good" symmetry, and many experiments are currently searching for CPT violation.

As explained in the previous section, EDMs violate T-symmetry, and therefore under the assumption that CPT is a good symmetry that means EDMs also violate CP symmetry. Therefore EDMs are a way to "hunt" for new sources of CP violation, and test theories that predict new mechanisms of CP violation.

2.2 Molecular EDMs and Dumbbells

A common source of confusion, especially for students new to the concept of EDMs in the context of fundamental symmetries, is that EDMs are familiar from classical electrodynamics, but were introduced without any discussion of CP violation. Polar molecules, whether heteronuclear diatomic molecules or more complicated molecules like water and ammonia, are said to have permanent EDMs, which one can find in various texts. These EDMs can be quite large, on the order of 10^{-8} e·cm, but don't violate P or T symmetries. The reasons for this are subtle. For concreteness, we consider the ammonia molecule, NH_3, which has a symmetrical top geometry. Defining k to be the quantum number associated with the projection of the rotational angular momentum on the symmetry axis, we have non-degenerate parity states given by

$$|\Psi_{\pm}\rangle = \frac{1}{\sqrt{2}}(|k\rangle \pm |-k\rangle) \tag{2.5}$$

An EDM can be aligned with or against k, but as $|k\rangle$ and $|-k\rangle$ are present here with equal weights, the EDM of each state $|\Psi\rangle$ is zero. When a small electric field is applied, the energy of the interaction will be small compared to the energy splitting between the

symmetric and antisymmetric parity states, and the molecule will acquire an induced electric dipole moment; *i.e.* the Stark effect will be quadratic in the applied electric field. When the electric field is increased, such that the interaction energy is large compared to the splitting between the opposite parity states, the Stark effect will become linear. In this regime, the molecule can be said to have a "permanent" EDM. But this is qualitatively different to the EDM that arises in the discussion of CP violation; in that case the Stark effect is linear for small electric field.

Another common example of an EDM is that of an electrostatic dumbbell, in which equal and opposite charges are attached to a rod, fixed by some separation. By definition this configuration has an electric dipole moment. We can write the state $|+\rangle$ to be one in which the positive charge is up, and $|-\rangle$ in which the positive charge is down. We will therefore have opposite parity states given by

$$|\Psi_{\pm}\rangle = \frac{1}{\sqrt{2}}(|+\rangle \pm |-\rangle) \tag{2.6}$$

In this case, however, the two parity states are degenerate. So we exclude this as a possible source of T violation by emphasizing that a *non-degenerate* state that possesses an intrinsic EDM violates T symmetry.

2.3 General Discussion of EDM Measurements

Having briefly described why a search for a permanent electric dipole moment is useful, we now discuss the basic idea behind measuring an EDM. Consider a neutral particle (neutron, atom, molecule, etc.) in its ground state with a total angular momentum of $F = 1/2$ for simplicity. Let the particle sit in an external magnetic field $\vec{B} = B_0\hat{z}$, such that the magnetic moment $\vec{\mu}$ precesses about the z axis (this is explained further in Chapter 6). If the particle is placed in a uniform (in both space and time) electric field $\vec{E}$, parallel to the external magnetic field for convenience, the atom will only couple to the electric field through the EDM $\vec{d}$, as it has no monopole moment. In particular, if the magnetic moment of the particle is perpendicular to the fields, the precession frequency will be given by

$$\hbar\omega_{\pm} = 2\mu B \pm 2dE$$

This is to say that just as the magnetic field couples to the magnetic (dipole) moment and causes a vector shift in the ground state magnetic sublevels, an EDM allows there to be a vector shift due to a DC electric field. The signal that contains the EDM is simply the difference in measured precession frequencies for different electric field conditions, the most common being a reversal of the electric field polarity:

$$\omega_{+} - \omega_{-} = \frac{4dE}{\hbar} + \frac{4\mu\delta B}{\hbar}$$

where δB introduces fluctuations in the ambient magnetic field. Recognizing that the EDM is expected to be extremely small, we see immediately that EDM experiments will generally demand large electric fields to maximize the change in precession frequency due to an EDM, and will also require a uniform and stable magnetic field environment, to prevent fluctuations in μB from dominating. We also immediately see that the signal will be given by a term linear in electric field, which will naturally reduce the number of possible systematic effects to those that allow the electric field (or the high voltage electronics that create it) to create a ground state vector shift. The statistical sensitivity of EDM measurements is determined by their ability to measure small frequency differences.

2.4 Current Best Limits from EDM Measurements

2.4.1 Neutron EDM

The first EDM experiment was performed on the neutron [13], by Ramsey and Purcell, with the first limit placed in 1957 [14]. Their initial sensitivity allowed them to constrain the neutron EDM to $|d_n| < 10^{-20} e\cdot$ cm. After many decades the limit has been reduced by 6 orders of magitude, currently at $|d_n| < 2.9 \times 10^{-26} e\cdot$ cm [15]. Initially, beams of thermal neutrons were used; later, beams of cold neutrons were built. By the 1970's the motion of atoms in the beam became a limiting systematic (this effect is discussed in Chapter 8), so after that ultracold neutrons (UCN) were employed, and continue to be

the technique used currently. Unlike a beam, ultracold neutrons can be enclosed in a macroscopic bottle, permitting long interrogation times and much lower velocities. The current limit was placed by a collaboration centered at the ILL in France, although there are other neutron EDM groups at the Spallation Neutron Source in the U.S. and the Paul Scherer Institute in Switzerland.

Neutron EDM experiments are primarily sensitive to CP violating effects in the hadronic sector, particularly EDMs in quarks and gluons. A major advantage neutron EDM measurements have over atomic and molecular experiments is that no atomic or molecular structure calculations are needed in the analysis.

2.4.2 Electron EDM

Electron EDM measurements are typically done with paramagnetic species; i.e. species with an unpaired valence electron, to avoid suppressing the effect. Electron EDM measurements have been performed in cesium [16], thallium [17], YbF [18], and solid-state systems [19]. Because electron EDMs do not arise until the four-loop level in the Standard Model, the predicted EDM of the electron is very small, at the 10^{-38} $e\cdot$ cm level.

Current-generation electron EDM searches typically make use of polar molecules rather than atoms. In a polar molecule, an external electric field creates an enhanced internal electric field (on the scale of 100 GV/cm), resulting in a large improvement in EDM sensitivity. The current best limit is placed with a ThO beam, by the ACME collaboration between Harvard and Yale [20]. That limit is $|d_e| < 8.7 \times 10^{-29} e\cdot$ cm. The experiment takes advantage of an Ω-doublet in ThO to suppress systematic effects, as the effective internal electric field can be reversed without reversing the laboratory electric field.

2.4.3 Diamagnetic Atom EDM

The EDM of an atom is related to the CP violating parameters by the relation

$$d_{atom} = \alpha_{Schiff} S + \alpha_e d_e + \alpha_T C_T + \alpha_S C_S$$

Here d_e is the EDM of the electron, C_T is a tensor CP-violating electron-nucleon coupling, and C_S is a scalar CP-violating electron-nucleon coupling. Each α represents

the sensitivity to the corresponding parameter, from atomic and/or nuclear structure calculations. S is the Schiff moment, described in more detail in Chapter 3, and can be further subdivided into contributions from the EDM of the neutron (d_n) and proton (d_p), as well as scalar and vector pion-nucleon couplings g_π^0 and g_π^1 respectively:

$$\alpha_{Schiff} S = \alpha_n d_n + \alpha_p d_p + \alpha_0 g_\pi^0 + \alpha_1 g_\pi^1$$

So here we see one complication that arises from a measurement of an atomic EDM: significant theoretical work is required to place limits on underlying CP-violating parameters (i.e. the calculations of the various α coefficients). For a diamagnetic atom, in which the valence electrons are all paired, the sensitivity to an electron EDM is greatly reduced compared to a paramagnetic atom. The atomic EDM is dominated by nuclear contributions, and often approximated only with pion-nucleon couplings. The current limit on a diamagnetic atom comes from the measurement of ^{199}Hg at the University of Washington, which reached a limit of $3 \times 10^{-29} e\cdot$ cm, roughly 4 orders of magnitude larger than the Standard Model prediction for that species [21].

2.4.4 Other EDM Limits

The three sectors listed above represent the most active areas of research, but are by no means the only EDM sectors under study. Experiments have placed limits on the EDMs of the proton [22] (from the ^{199}Hg measurement), muon [23], tau [24], Λ_0 [25], electron/muon neutrino [26], and tau neutrino [27]. The search for EDMs is an active and growing field.

Chapter 3

Motivation for a Radium EDM Experiment

3.1 Schiff Theorem and Schiff Moment

The dominant contribution to the EDM of a diamagnetic atom comes from CP violation in the hadronic sector. In 1963 Schiff realized that for a point-like nucleus and non-relativistic electrons the electron cloud of an atom will completely shield the EDM of the nucleus, resulting in no atomic EDM to measure [28]. Even if an external electric field is applied, the electron cloud will shield it from coupling to the nuclear EDM. If electrostatics are the only forces involved the shielding will be perfect. However, if one allows for other forces (say, magnetic fields from relativistic electrons) then the shielding will be incomplete. Schiff defined an operator, known as the Schiff moment $\vec{S}$, which is P-odd and T-odd and couples to an external electric field, that represents the quantity to which atomic EDM measurements are sensitive. The Schiff moment is given by [29]:

$$\vec{S} = \frac{1}{10}\int \rho(r)(r^2 - \frac{5}{3}\langle r^2\rangle_{ch})\vec{r}d^3(r) \tag{3.1}$$

where $\rho(x)$ is the nuclear charge distribution. We see that the Schiff Moment is a kind of radially-weighted dipole moment. However, it is perhaps more informative to write the Schiff moment so that we can clearly see the effect of a P-odd and T-odd operator. We begin by defining the ground state of the Hamiltonian without P-odd, T-odd effects

to be $|\Psi_0\rangle$, and the eigenstate of the Hamiltonian with a P-odd, T-odd perturbation V_{PT} to be $|\Psi'\rangle$. We first identify

$$\langle\Psi_0| S_z |\Psi_0\rangle = 0 \tag{3.2}$$

According to first order perturbation theory this gives us

$$\left|\Psi'\right\rangle = |\Psi_0\rangle + \sum_i \frac{|\Psi_i\rangle \langle\Psi_i| V_{PT} |\Psi_0\rangle}{E_0 - E_i} + c.c. \tag{3.3}$$

This gives us

$$S \equiv \langle S_z\rangle = \left\langle\Psi'\right| S_z |\Psi_0\rangle + \sum_i \frac{\langle\Psi'| S_z |\Psi_i\rangle \langle\Psi_i| V_{PT} |\Psi_0\rangle}{E_0 - E_i} + c.c. \tag{3.4}$$

This leaves us with

$$S = \sum_{i\neq 0} \frac{\langle\Psi_0| S_z |\Psi_i\rangle \langle\Psi_i| V_{PT} |\Psi_0\rangle}{E_0 - E_i} + c.c. \tag{3.5}$$

3.2 Static Deformations

We now consider the effect of nuclear deformations on the Schiff moment, and show that deformations can result in significant enhancement. Following the treatment in [30] we write the surface of a nucleus in terms of spherical harmonics

$$R(\theta) = R_N[1 + \sum_{l=1} \beta_l Y_{l0}(\theta)] \tag{3.6}$$

Each β is a deformation parameter in the multipole expansion; i.e. β_0 is the monopole deformation, β_1 is the dipole deformation, etc. Defining the center of mass to be at $r = 0$ requires

$$\beta_1 = -3\sqrt{\frac{3}{4\pi}} \sum_{l=2} \frac{(l+1)\beta_l \beta_{l+1}}{\sqrt{(2l+1)(2l+3)}} \tag{3.7}$$

It is then possible to rewrite the Schiff moment as

$$\vec{S}_z = \vec{S}_{intr} \frac{2KM}{I(I+1)} [\sum_{i \neq 0} \frac{\langle \Psi_i | V_{PT} | \Psi_0 \rangle}{E_0 - E_i} + c.c.] \tag{3.8}$$

Where $K = |\vec{I} \cdot \vec{n}|$ is the absolute value of the projection of the nuclear spin on the nuclear axis (with $M = I_z$), and with the intrinsic (geometric) Schiff moment given by

$$S_{intr} = eZR_N^3 \frac{3}{20\pi} \sum_{l=2} \frac{(l+1)\beta_l \beta_{l+1}}{\sqrt{(2l+1)(2l+3)}} \tag{3.9}$$

Now we see that the more deformed the nucleus, in general the larger the Schiff moment.

3.3 Advantages to Using ^{225}Ra

3.3.1 Octupole Deformation

In the previous section we discussed how deformations can enhance the Schiff moment, and therefore EDM sensitivity. ^{225}Ra has a particularly deformed nucleus, and this represents one of the primary reasons we have chosen to study it. One of the indicators of octupole deformation is the existence of a nearly degenerate parity doublet, as an octupole deformed nucleus is not reflection symmetric [31]. Figure 3.1 shows the nuclear levels of ^{225}Ra; note the ground state parity doublet at 55 keV. ^{225}Ra has both a larger quadrupole and a larger octupole deformation compared to ^{199}Hg, with $\beta_2 = 0.138$ and $\beta_3 = 0.104$, whereas ^{199}Hg has $\beta_2 = $ -0.122 and $\beta_3 = 0$ [32]. The shapes of the two nuclei are shown in Figure 3.2.

It should be noted that the deformations discussed here are in the intrinsic frame of the nucleus, not the lab frame. A spin $I = 0$ or $I = 1/2$ particle in the lab frame cannot have quadrupole, octupole, or higher moments, as there is no preferred direction. However, in the "body" frame these moments are allowed. As an example, below we give the relation between the intrinsic quadrupole moment in the body frame and lab frame [34]:

$$Q_{lab} = Q_{intrinsic} \frac{3K^2 - J(J+1)}{(J+1)(2J+3)} \tag{3.10}$$

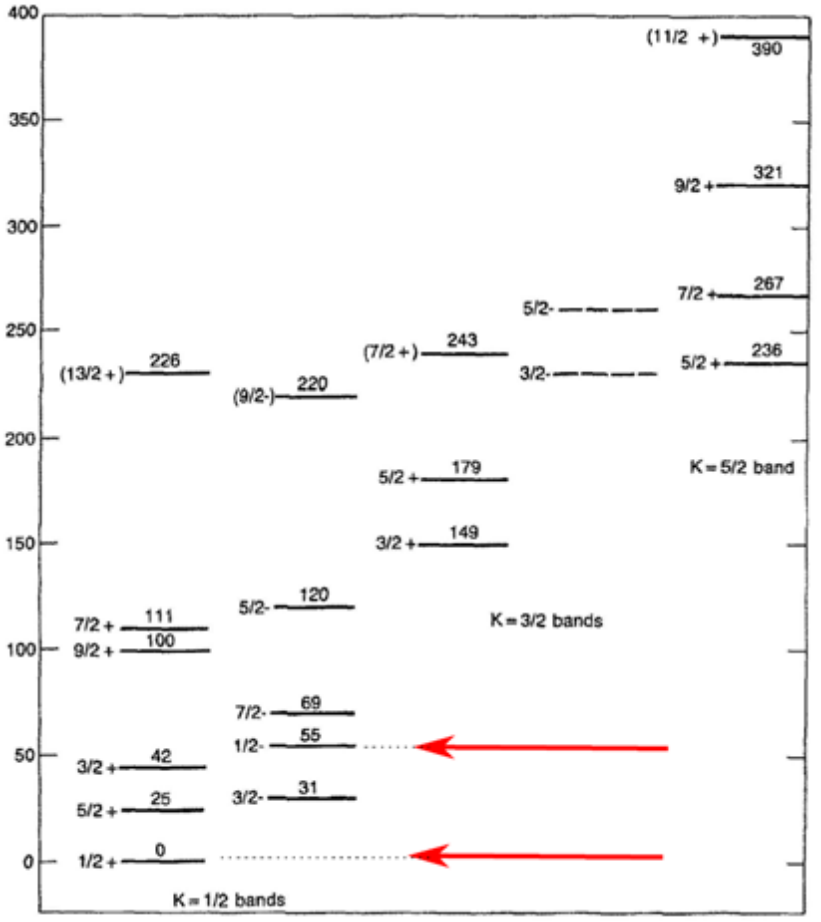

FIGURE 3.1: Nuclear levels of ^{225}Ra. Red arrows indicate the parity doublet states separated by 55 keV [33].

where the nucleus is viewed as a rotating ellipsoid with a fixed projection K of the total angular momentum J. Here the maximum value of K is J.

From this we see that the nuclear structure of ^{225}Ra, with its large octupole deformation, leads to a significant enhancement in the geometric part of the Schiff moment. The Schiff moment for ^{199}Hg, with negligible octupole deformation, comes from a term not included in this analysis, that of a valence neutron "attached" to the surface of the nearly-spherical nucleus. The nuclei near radium in the periodic table, such as radon and francium, are also expected to have octupole deformations, and EDM searches are underway in those species.

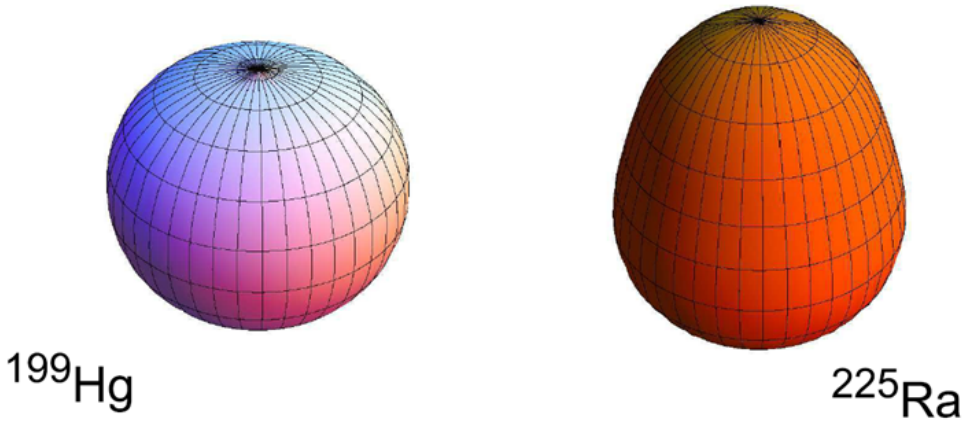

FIGURE 3.2: Comparison of Hg and Ra nuclei [35].

3.3.2 Parity Doublet

As we saw in the previous section, the existence of an octupole deformation is indicated by the presence of a parity doublet. This leads to a second, complementary enhancement in the first-order perturbation expansion given in equation 3.8. In fact, in the literature the expansion for ^{225}Ra is often not even written as a sum over terms, as only one term in the expansion is sufficient.

Further, it is noted that this parity doublet makes nuclear structure calculations more accurate in ^{225}Ra than in ^{199}Hg. There are a wide range of theoretical estimates of the pion-nucleon coupling terms for ^{199}Hg; there is not even agreement on the sign for the isovector term [36]. There is no analogous parity doublet transition in mercury, so the mercury nucleus is "soft" and may not be very well described by a single mean field. As noted in Ref. [36], it is not really the challenging nature of the calculations for ^{199}Hg that leads to uncertainty, but rather that only a few groups have attempted it.

3.3.3 Relativistic Enhancements

The discussion so far has focused on the large ^{225}Ra Schiff moment. However, in order to guarantee the atomic EDM will be large we need to consider not only the Schiff moment but also the electron cloud shielding. This involves advanced many-body perturbation theory atomic structure calculations beyond the scope of this thesis.

The EDM in Ra is calculated to be [37]

$$d(^{225}Ra) = -8.5 \times 10^{-17}(\frac{S}{e \cdot fm^3})e \cdot cm \tag{3.11}$$

which is about 3 times less suppressed than the EDM for Hg

$$d(^{199}Hg) = -2.8 \times 10^{-17}(\frac{S}{e \cdot fm^3})e \cdot cm \tag{3.12}$$

3.4 Disadvantages of Using 225Ra

The primary disadvantage of ^{225}Ra is that it is radioactive, and this significantly limits its availability. At the moment, the only known source of ^{225}Ra is Oakridge National Laboratory, capable of providing up to 30mCi (less than 1 μg) of ^{225}Ra once every 2 months. A variety of mitigating circumstances (most commonly scheduling conflicts) further limit this rate. For example, in 2014 four ^{225}Ra samples were ordered, three with 3 mCi and one with 6 mCi.

The other primary challenge with radium is its low vapor pressure; its boiling point is about 1700 ^{o}C, with a vapor pressure of 8 mTorr at 546 ^{o}C. By contrast, the vapor pressure of mercury is 2 mTorr at room temperature, resulting in a density of about 5×10^{13} atoms per cubic centimeter. Given the low vapor pressure, it was decided to attempt a radium EDM measurement using laser-cooled and trapped atoms, rather than a vapor cell. This has the additional effect of making the experiment sensitive to a different set of systematics than the ^{199}Hg experiment, and allows application of greater electric field (the Hg experiment was limited to 10 kV/cm due to the glass cell). The challenges associated with laser cooling and trapping radium will be discussed in the next chapter.

Chapter 4

Laser Cooling and Trapping of Radium

4.1 Radium Energy Levels

The experiment requires the cooling and trapping of two isotopes of radium – ^{226}Ra, which has a half-life of 1600 years and has no nuclear spin (and is thus not directly useful for an EDM measurement), and ^{225}Ra, which has a half-life of 15 days and a nuclear spin of 1/2. ^{225}Ra is thus used for the actual nuclear spin precession and EDM experiments, while ^{226}Ra is used for development and diagnostics (as it is less radioactive, it is possible to work with many more ^{226}Ra atoms safely).

Ideally, one would use a strong, closed transition for laser cooling and trapping – and a weaker (still closed) transition for achieving low temperatures. Unfortunately, while the $^1S_0$-$^1P_1$ (483 nm) transition is relatively strong (a linewidth of 30 MHz), it is "leaky", decaying not just to $^1S_0$ but also $^1D_2$, $^3D_1$, and $^3D_2$. Only about 1100 photon scatters are possible on the 483 nm transition before the population has been pumped into metastable states. Rather than attempt to "plug the leaks" with a large number of repump lasers, the $^1S_0$-$^3P_1$ transition was chosen for the loading, trapping, and cooling. The narrow linewidth of this transition (420 kHz) limits the capture velocity of the Transverse Cooling, Zeeman Slower, and 3D MOT, but with only a single repump (on the $^3D_1$-$^1P_1$ 1428 nm transition) it is possible to get over 10^7 photon scatters before the atoms go dark.

Even with the single repump for $^3D_1$-$^1P_1$, it would not be immediately obvious that radium can be loaded into a MOT. The $^3D_1$ state will decay to $^3P_0$ and might be lost to the cooling cycle. Fortunately, there is an additional repump from blackbody radiation that pumps atoms back from $^3P_0$ to $^3D_1$. As discussed in [38], this room-temperature blackbody radiation provides a sufficiently high pump rate out of the metastable states to allow for a many-second long trap lifetime.

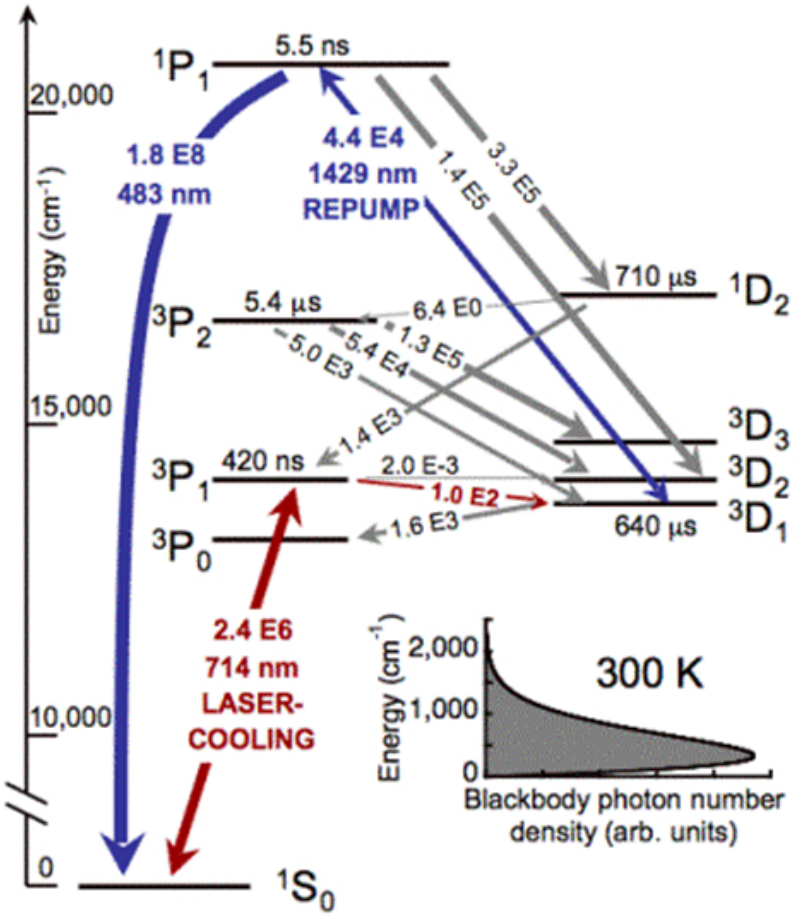

FIGURE 4.1: Energy Levels of ^{226}Ra. Transition rates are given by Bieron et al [39].

4.2 Lasers and Locking Systems

4.2.1 714 nm Laser

We will first discuss the lasers used in the experiment, and their associated locks. Detail about the application of these lasers to the laser cooling and trapping of radium can be found in the next sections of this chapter.

The 714 nm laser is intended to drive the $^1S_0$-$^3P_1$ intercombination transition in radium, and is considered the "main" laser of the experiment. The experiment requires (in its current configuration) about 1.2 W of 714 nm light, with a linewidth much less than the natural 400 kHz linewidth of the transition (100 kHz is typical; narrower is better). The 714 nm light is created by a Spectra-Physics Matisse ring-cavity TiSaph laser, which is pumped by a 532 nm Spectra-Physics Millennia Prime solid-state diode laser system. For a pump power of 15 W, which is routinely achieved, we observe about 2 W of 714 nm light when the ring-cavity alignment is optimized. This allows us a great deal of overhead in our power requirements.

The output of the TiSaph is split into many different paths − most of the power goes to the vacuum system, but some of the power is split off and sent to a Bristol wavemeter and a ULE cavity. The Matisse is internally locked to a thin etalon and a piezo etalon to keep it stable and single-mode, and locked by a cavity-mirror-mounted piezo to a reflection Pound-Drever-Hall lock to the ULE cavity (the theory behind the Pound-Drever-Hall lock will be covered later in this chapter). The ULE cavity is temperature-regulated and thermally isolated, drifting less than 10 mK per hour. The light that goes to the ULE cavity is sent first through a broadband AOM in double-pass, allowing us to easily lock to a cavity mode for both the 226 and 225 isotopes.

As the frequencies of the ULE cavity modes will drift in time, this AOM is occasionally adjusted to compensate. The drift is measured by recording the frequency drift in the MOT spectrum over time, and is shown in Figure 4.2. Both thermal drift and mechanical "settling" contribute to the frequency drift. The actual magnitude of the drift is not important, as it is relatively easy to compensate for the drift − the improvement of using a ULE cavity is that the drift-compensation only needs to be done every 1-2 weeks.

4.2.2 Two 1428 nm Lasers

Despite the blackbody repumping described earlier, one repump at 1428 nm is still needed for long MOT lifetimes (the MOT lifetime without this extra repump is about 30 ms). This repump laser pumps atoms from $^3D_1$ to $^1P_1$ (once in $^1P_1$, the atoms rapidly fall to $^1S_0$). With sufficient power in this repump, MOT lifetimes of up to 50 seconds have been observed. As the main limitation of this experiment will be the number of trapped atoms, the ability to accumulate large numbers of atoms over time is very important.

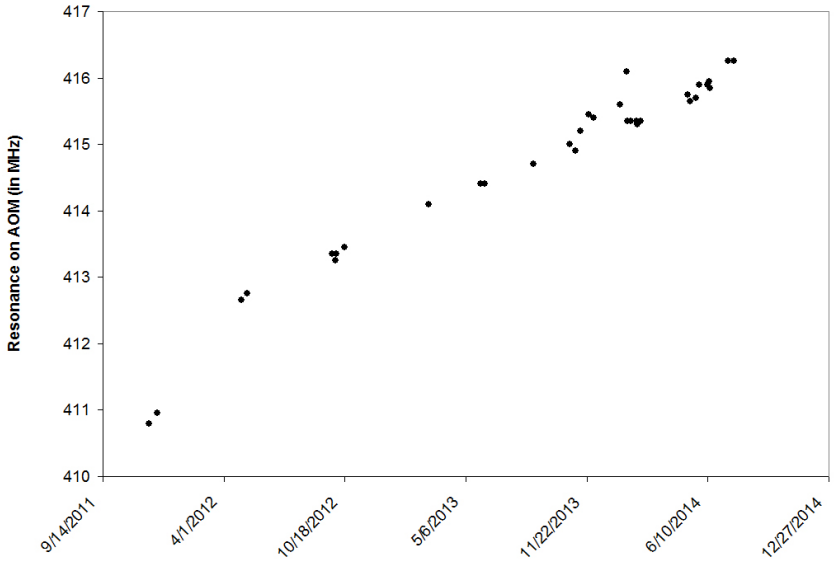

FIGURE 4.2: Drift in the ULE frequency over time, measured by adjusting the RF frequency and measuring the MOT spectrum.

The original repump system used by the radium experiment was a New Focus Vortex, capable of producing about 12 mW. After sending the light to a wavemeter, a cavity for locking, and through a fiber to reach the trap, the available power at the atoms was about 2 mW. For the beam size needed in the experiment, saturation occurs at approximately 30 mW, so using only 2 mW at the atoms significantly limited the trap lifetime.

The first step in improving this was to implement an injection-lock system, sending the Vortex into a higher-output fiber-coupled diode laser, from QC Photonics. Diode lasers ranging from 150 mW-300 mW were tried. This system increased the available power at the atoms to about 60 mW, but required constant adjustment. Over time, the fiber tip would get damaged or covered by a particle of dust, and the laser would become multimode; further, the alignment of the "master" laser proved to be quite sensitive and time-consuming. In each of these schemes, part of the output light is sent into a temperature-stabilized Fabry-Perot cavity, which is in turn locked to a frequency-stabilized HeNe laser, with a frequency stability of 2 MHz per hour. Reflections from the cavity and the fiber coupler compete with the injection lock to limit the maximum output power at which the injection lock will be dominant (typically no more than 200 mW).

The solution to this problem came from the realization that a fiber-coupled diode, with

an internal FBG (Fiber Bragg Grating) at the correct wavelength would provide sufficient power and be much less sensitive to the environment. Further, a company (Fara-Banafsh in Texas) was capable of producing such a laser, relatively cheaply. The FBG is housed in a temperature-controlled copper sleeve; varying this temperature provides coarse frequency tunability. Locking to a cavity is done by feeding back to the diode current. This laser is capable of producing about 300 mW; the output is sent through an optical isolator and split to a wavemeter, cavity, and to a fiber which sends the power to the atoms. Unfortunately a significant amount of power is lost through the isolator; nonetheless it is relatively easy to send 60 mW of repump light to the atoms. The repump light is sent vertically down into the chamber, and is made large enough to hit the MOT with the Slower beam (described in a later section) both on and off (which displaces the MOT by about a centimeter).

The Fara-Banafsh laser proved to be so effective and easy to use that a second laser was purchased, basically identical to the first. The only significant change is slightly higher power, 400 mW instead of 300 mW, and a more robust temperature control apparatus for the FBG. The fiber was significantly bent upon arrival, however that has not seemed to influence performance. Using lessons learned from the first repump setup, this "New Repump" laser arrangement is different than the "Old Repump" − no isolator is used, instead tiny fractions of light are split off from the main beam by pieces of glass and sent to the various fibers as needed. The main beam is sent directly into the MOT chamber, in free space. This allows over 300 mW of light to reach the atoms, while avoiding back-reflection issues simply by virtue of the small fractions of light used in the other paths. This laser is beat-locked to the Old Repump, with a tunable offset of 10-100 MHz between the two lasers.

Due to dissatisfaction with the long-term stability of the HeNe laser, the scanning Fabry-Perot cavity was replaced by a temperature-regulated Zerodur cavity, inside a vacuum chamber. The vacuum chamber is fitted with a small ion pump to maintain vacuum, to avoid variable-pressure-induced frequency drift. The old 1428 nm laser is locked to the Zerodur cavity with a reflection Pound-Drever-Hall scheme, very similar to the one used with the ULE cavity (the Pound-Drever-Hall lock is covered later in this chapter). As this transition is 30 MHz (governed by the $^1S_0$-$^1P_1$ transition) there is no need to compensate for frequency drift as with the ULE cavity.

When working with ^{225}Ra the situation is a bit more complicated, as there are now two ^{3}D$_1$ states into which the atoms can fall (F=3/2 and F=1/2), and similarly two ^{1}P$_1$ states (again, F=3/2 and F=1/2). When working with ^{225}Ra, at least one of the lasers is tuned to pump atoms out of the ^{3}D$_1$ F=3/2 state and into the ^{1}P$_1$ F=3/2 state. This proves sufficient to give the same MOT lifetime (within 10%) as the ^{226}Ra MOT. Experiments to pump atoms out of both ^{3}D$_1$ states simultaneously have been done, but did not result in a detectable gain in lifetime. The electronics for the beat lock between the "old" repump and "new" repump are slightly more complicated than a standard beat lock system, as we wish to use the "old" repump exclusively for ^{226}Ra and quickly switch the "new" repump between the two isotopes as needed; the relevant transitions are separated by 1.490 GHz. The electronic configuration is shown in Figure 4.3.

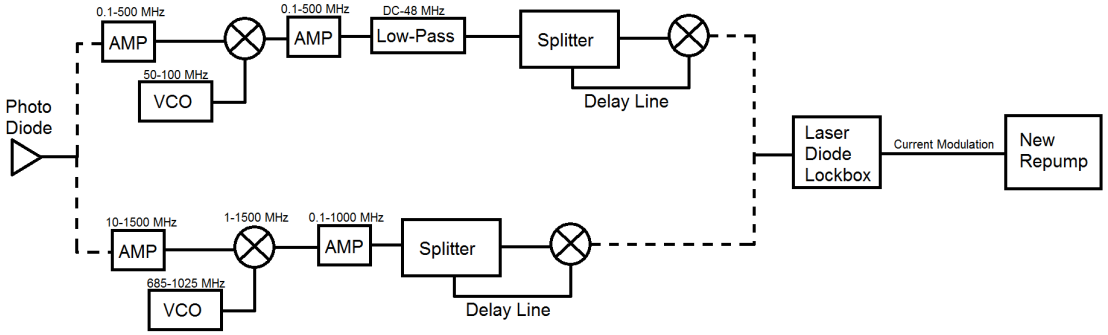

FIGURE 4.3: Block diagram for the beat lock between the two repump lasers. Two separate systems can lock at two very different beat frequencies; we transition between the two configurations by physically changing BNC cables (those cables are represented by dashed lines in the figure). The photodiode used is a ThorLabs DET08CL, for frequencies up to 5 GHz.

4.2.3 483 nm Laser

The 483 nm laser is intended to drive the ^{1}S$_0$-^{1}P$_1$ transition, which for now is only used for optical pumping and state readout in the science chamber. This transition was chosen over the intercombination transition for this purpose due to its short lifetime (5.5 ns), which results in higher signal-to-noise (see the discussion of spin precession in Chapter 6 for more detail). A home-built 966 nm ECDL is frequency-doubled to produce the 483 nm light. The ECDL is in Litrow configuration, and can produce about 150 mW of 966 nm light with a linewidth less than 1 MHz.

The 966 nm laser is locked to the same Zerodur cavity as the 1428 nm laser, in a different (perpendicular) channel. A reflection Pound-Drever-Hall lock scheme is used, similar to the ones used for the 714 nm and 1428 nm lasers (the Pound-Drever-Hall lock is covered later in this chapter).

About 70 mW of this 966 nm light is then sent into a PPLN waveguide from HC Photonics, in single-pass. There are 12 waveguides in the crystal, but only one works at the desired wavelength. Though output powers as high as 4.5 mW have been achieved, due to the difficulty in mode-matching the 966 nm light (which comes from a rectangular diode) to the waveguide the typical output power is 1-2 mW. The experiment in its current form requires only about 100 μW of 483 nm light, so even after being sent through a fiber and an AOM this power is more than sufficient.

4.2.4 Two 1550 nm Lasers

A 50 W IPG Photonics laser at 1550 nm is used as the so-called "bus" ODT, which transports the atoms 1 meter. The laser is neither single-mode, nor single-frequency, nor polarized. Due to the potentially time-dependent polarization it must be off during the actual nuclear spin precession to avoid vector-AC-Stark-shift-induced decoherence; however due to the high power this cannot be done simply by turning off the laser diodes (which can produce thermal lensing on the fiber output). Therefore a large pneumatic shutter was installed where the beam was expanded in a telescope to shutter the beam − the shutter is suspended from a separate shelf to avoid misalignment of optics caused by the rather violent motion of the shutter.

A second IPG Photonics laser is used as the "holding" ODT. As it will be used to form a standing wave trap, it must be polarized, single frequency, and single mode. This second laser is capable of producing 30 W, but as it is retroreflected to produce the standing wave, it is sent through two optical isolators. The use of only one 30 dB isolator for this purpose destroyed a 10 W IPG laser, so now two 30 dB isolators are used. Unfortunately, the damage threshold of the optical isolators is 10 W, which prevents us from using the laser at its maximum 30 W output power. While this power is sufficient for reasonable transfer between the two ODTs, we strongly suspect that our transfer efficiency would be higher if we could use more power.

4.2.5 Pound-Drever Hall Locking

The 714 nm laser, the "old" 1428 nm laser, and the 966 nm laser are all locked to cavities by Pound-Drever-Hall (PDH) locks. Because of the ubiquitous use of this technique, it deserves special attention. The PDH technique is very common in atomic physics experiments, as a technically simple way to generate a narrow linewidth error signal with a cavity. This error signal can then be used to apply feedback to an element that changes the laser's frequency, typically by adjusting the voltage on a piezo or the current in a diode (often both). The cavity is a pair of highly reflective mirrors mounted on a very stable spacer; in our experiment we use ULE and Zerodur (an etalon can also be used to generate the error signal). This treatment closely follows that of [40].

We first consider the regular operation of a cavity on resonance. If the spacing between the mirrors is an integer multiple of the wavelength, the light intensity inside the cavity will build up due to constructive interference. A small fraction of the light will exit through each mirror. Ignoring losses in the cavity, the light entering the cavity will be transmitted through when on resonance, due to destructive interference between the reflected incident beam and the leakage of the standing wave inside the cavity, which cancels the reflected beam. When the light is not on resonance, phase cancellation will not occur and light will be reflected off the cavity. A cavity will have multiple resonant frequencies, separated by the Free Spectral Range (FSR), given by $FSR = c/2L$, where L is the length of the cavity. The linewidth of the cavity is given by $\Delta\nu = FSR/\mathcal{F}$, where $\mathcal{F} = \frac{\pi\sqrt{R}}{1-R}$ is the finesse of the cavity and R is the reflectivity of the etalon mirrors. We can now define a reflection coefficient $F(\omega)$, of which the in-phase component gives the magnitude of the reflected electric field and the out-of-phase component gives the phase of the reflected field

$$F(\delta) = \frac{E_{ref}}{E_{inc}} = \frac{R[exp(i\frac{\delta}{FSR}) - 1]}{1 - R^2 exp(i\frac{\delta}{FSR})} \tag{4.1}$$

where $\delta = \omega - \omega_0$. We now consider what happens if we phase modulate the incoming light, for example with the use of an EOM.

$$E_{inc} = E_0 e^{i(\omega t + \beta \sin \Omega t)} \approx E_0[J_0(\beta)e^{i\omega t} + J_1(\beta)e^{i(\omega+\Omega)t} - J_1(\beta)e^{i(\omega+\Omega)t}] \tag{4.2}$$

where β is the modulation depth, chosen such that the majority of power is in the carrier and first order sidebands, Ω is the modulation frequency (typically in the RF), and the J's are Bessel functions. If the modulation is large enough, the sidebands will be pushed far enough away from the center frequency that they will be completely reflected by the cavity when the carrier is on resonance. With three beams incident on the cavity (the carrier and the two sidebands), we multiply each frequency by the reflection coefficient at the appropriate frequency:

$$E_{ref} = E_0[F(\omega)J_0(\beta)e^{i\omega t} + F(\omega+\Omega)J_1(\beta)e^{i(\omega+\Omega)t} + F(\omega-\Omega)J_1(\beta)e^{i(\omega+\Omega)t}] \quad (4.3)$$

We actually measure the reflected intensity on a photodiode, rather than the reflected electric field, given by $P_{ref} = |E_{ref}|^2$. We will get a variety of interference terms with different combinations of frequencies (ω, $\omega \pm \Omega$, and 2Ω); we keep the terms up to but not including 2Ω:

$$\begin{aligned} P_{ref} = {} & J_0^2(\beta)P_0|F(\omega)|^2 + J_1^2(\beta)P_0[|F(\omega+\Omega)|^2 + |F(\omega-\Omega)|^2] + \\ & 2\sqrt{J_0^2(\beta)P_0 \cdot J_1^2(\beta)P_0} \cdot [Re[F(\omega)F^\star(\omega+\Omega) - F^\star(\omega)F(\omega-\Omega)]\cos\Omega t + \\ & Im[F(\omega)F^\star(\omega+\Omega) - F^\star(\omega)F(\omega-\Omega)]\sin\Omega t] + (2\Omega \text{ terms}) \end{aligned} \quad (4.4)$$

where $P_0 = |E_0|^2$. In practice, we can use a mixer (and a phase delay line if needed) to isolate only the component of this signal that varies as either $\sin\Omega t$ or $\cos\Omega t$. Let us choose to operate where the carrier is on resonance but the sidebands are not, so that the sidebands are totally reflected; *i.e.* $F(\omega+\Omega) \approx -1$. In this case part of the expression above simplifies, as we have

$$F(\omega)F^\star(\omega+\Omega) - F^\star(\omega)F(\omega-\Omega) \approx -2iIm[F(\omega)] \quad (4.5)$$

so that the cosine term above becomes negligible. Our resulting Pound-Drever-Hall error signal is given as

$$\epsilon = -2\sqrt{J_0^2(\beta)P_0 \cdot J_1^2(\beta)P_0}\, Im[F(\omega)F^\star(\omega+\Omega) - F^\star(\omega)F(\omega-\Omega)] \tag{4.6}$$

A characteristic PDH lineshape is shown in Figure 4.4.

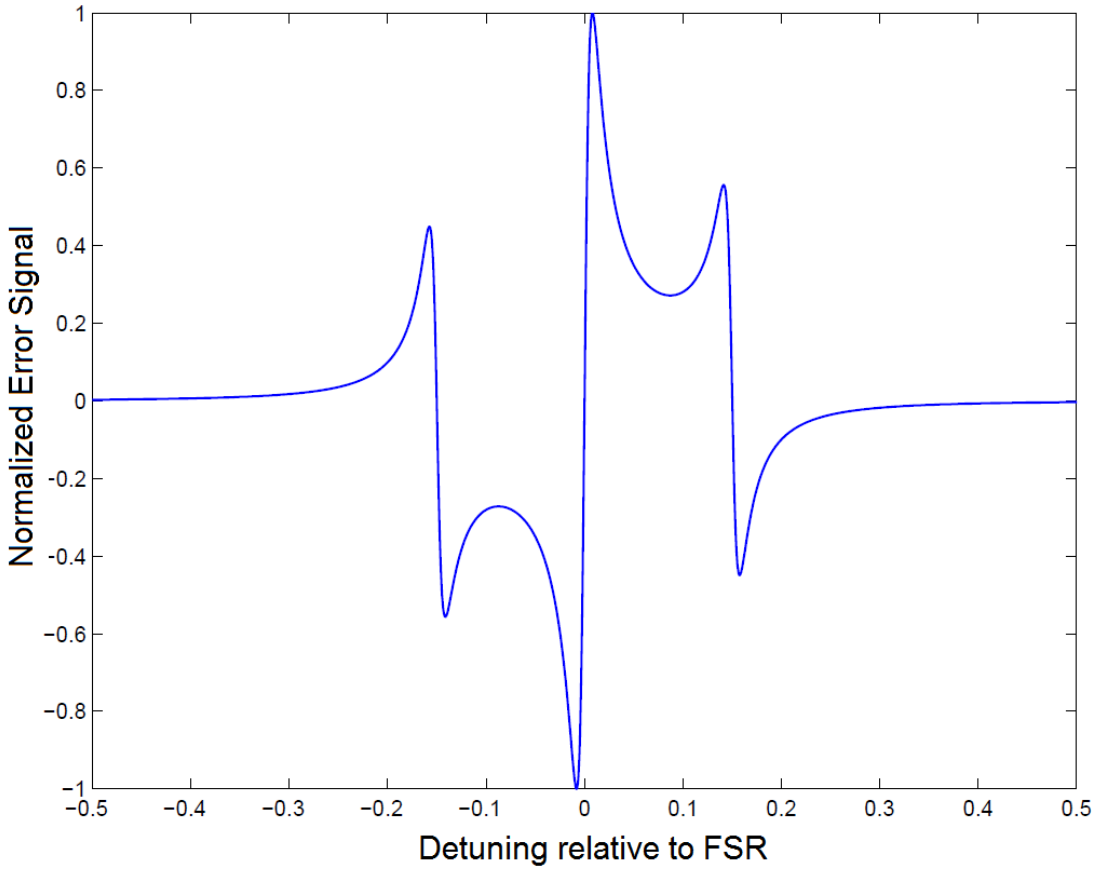

FIGURE 4.4: Shape of the Pound-Drever-Hall error signal. Adapted from [41].

4.3 Production of Atomic Beam

4.3.1 Radiochemistry

There are two general types of loads done for the Radium EDM experiment–loads of only ^{226}Ra, which have a relatively large number of atoms and are thus useful for apparatus contruction and diagnostics, and combined loads of ^{226}Ra and ^{225}Ra, which are actually used for the spin precession and EDM experiments. Thus far no loads have been attempted using only ^{225}Ra. For a ^{226}Ra-only load, a typical activity is about 3 μCi, while for a combined load we attempt to use 5 μCi of ^{226}Ra and 3-6 mCi ^{225}Ra.

The amount of ^{225}Ra limits the experiment, but due to safety concerns and lack of an additional source it is not planned to use significantly more in the foreseeable future. More ^{226}Ra is used during the combined runs simply to make the diagnostics easier (and thus faster), since the ^{225}Ra lifetime limits the duration of the combined run to about two weeks.

The procedure for a ^{226}Ra-only load is as follows: first, the nozzle, crucible, and perforated rod (all shown in 4.5) are "heat treated" (brought to 600 ^{o}C for about a day) to remove much of the hydrogen gas embedded in the material (the crucible is made of titanium, a getter material). This reduces the outgassing when the fully-loaded crucible is brought to high temperature inside the actual vacuum system. Similarly, the radium nitrate solution is dropped onto a piece of aluminum foil and left overnight to dry (to reduce contamination due to water in our vacuum system).

The barium arrives at Argonne in a glass ampule filled with argon gas. The pellet is approximately 0.1 g. On the day of the load, the neck of the ampule is sawed off (using a triangular file) inside a plastic bag to contain any shards of glass. The pellet of barium is rolled out of the opened ampule and cut into four pieces using a small wire cutter. The atomic barium will undergo a redox reaction with the radium nitrate in the vacuum system once the temperature is high enough for sufficient barium vapor pressure, yielding barium nitrate and atomic radium − this is the mechanism (we believe) by which we produce a beam of atomic radium. Two pieces of barium are put inside the aluminum foil; the foil is then wrapped up and put in the crucible. The other two pieces are added to the crucible outside the aluminum "wrapper". This procedure must be done quickly − even though the work area is backfilled with either nitrogen or argon, the barium will still oxidize quickly, which as described later will cause problems for the experimentation. Once the crucible is loaded, the nozzle (for beam collimation) and the perforated rod (to mount the crucible to a flange on the vacuum system) are attached.

The loading of the crucible is done in a separate lab from the atom trapping lab; once the crucible is loaded it is transported on a cart from one lab to another. The vacuum system is valved off and flushed with argon. The system is vented to atmosphere and the old crucible is replaced with the new one. The system is pumped down, and the old crucible is surveyed for radioactivity and put in a plastic bag for storage.

In the event that we wish to do a combined load of ^{226}Ra and ^{225}Ra, the two isotopes are mixed first before loading. At the moment, the only source of ^{225}Ra available seems to be Oak Ridge National Laboratory. For a combined ^{226}Ra and ^{225}Ra load, we typically order 3 mCi ^{225}Ra, which comes in the form of dried radium nitrate in a glass vial. Upon receipt of the sample, the radiochemist at Argonne adds the aqueous ^{226}Ra nitrate solution to the solid ^{225}Ra salt in the vial and mixes tham. As with a ^{226}Ra-only load, the radium nitrate solution is dropped on an aluminum foil and left to dry overnight – while it is unfortunate that the short-lived isotope will be left to decay for one night, it is worth it to reduce the pressure in the system.

4.3.2 Vacuum System

The complete vacuum system is several meters long and rather complex, so for intellectual simplicity it is divided into three parts–the Oven End, the MOT Chamber, and the Science Chamber. The Oven End is responsible for creating a beam of atomic radium, collimating that beam by a transverse cooling stage, and maintaining differential pumping through conductance limiting. During a "crack", the pressure in the Oven End may reach 10^{-5} Torr, but under normal operating conditions the pressure is typically kept at mid-10^{-9} Torr. A diagram of the Oven End is shown in Figure 4.5.

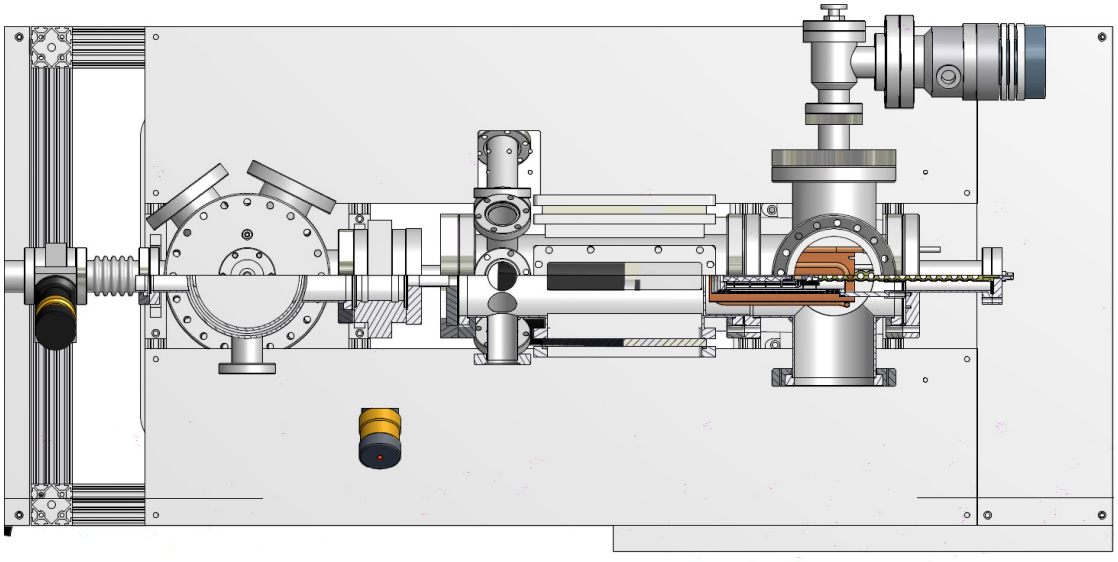

FIGURE 4.5: Diagram of the Oven End. On the right is the oven itself (the perforated rod, the crucible, and the nozzle) and the associated pumps and water-cooled stainless steel cooling shroud. In the middle is the transverse cooling chamber. On the left is the conductance-limiter and counting chamber, currently fitted with NEG pump.

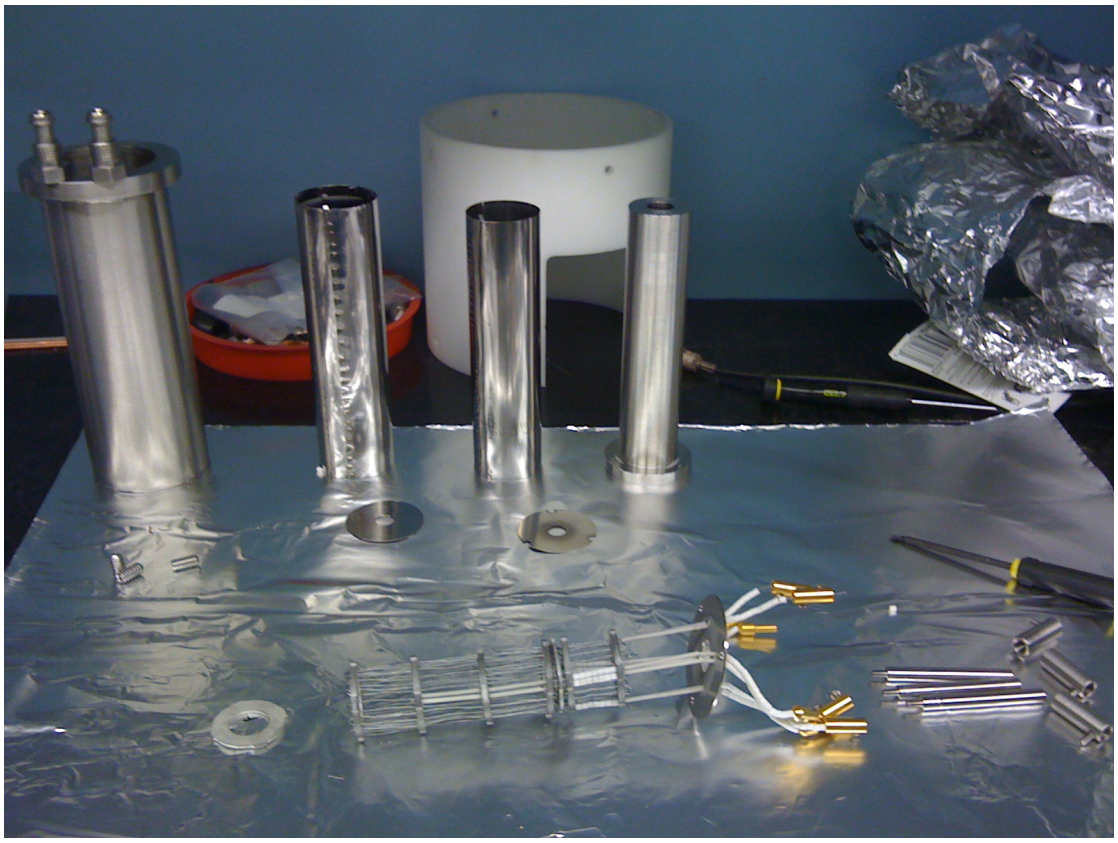

FIGURE 4.6: Disassembled oven, showing the component parts. The upper part of the image shows the stainless steel heat shields; the leftmost shield has feedthroughs for water cooling. The bottom shows the two oven filaments, a long one in front and a short one in the back, which (when assembled) surround the oven nozzle and heat it radiatively (the filaments are supported on ceramic spacers to avoid direct contact with the oven nozzle and crucible).

4.3.3 Atomic Beam Flux Measurements

The crucible is surrounded by two tungsten filament coils, one long and one short. Only the long one is used regularly.

The atomic beam flux can be measured by collecting the fluorescence of 714 nm photons from the atoms. A 1-inch-diameter lens placed inside the vacuum system collects the fluorescence and images it onto a PMT, with about 10% quantum efficiency and a 714 nm interference filter in front of it. To improve the signal-to-noise of the collection system, the 714 nm light is modulated at 1 MHz; this because the lifetime of the 714 nm transition is 420 ns, so half of the time the major source of 714 nm light comes from fluorescing atoms. The PMT data collection is collected and binned at 20 MHz, then gated in software so that we can observe only the signal when the 714 nm laser was off.

This data has much less background due to scatter from the vacuum system than the data with the laser on; this dramatically improves the theoretical SNR. In reality, there is background not just from scattered light but also from the blackbody radiation from the hot oven, but this modulated approach is still a dramatic improvement.

By varying the frequency of the 714 nm probe light one can map out a spectrum of the atomic beam, broadened by the transverse velocity of the atoms. To convert this spectrum into an actual flux, we first calculate how many counts we expect for a measurement:

$$N_{cnts} = N_{atoms} * \rho_{ee} * D * N_{cycles} * f \tag{4.7}$$

Here N_{atoms} is the number of atoms in the collection volume, ρ_{ee} is the excited state fraction, f is the fraction of photons collected. D is the decay probability, given by:

$$D = \frac{\int_0^{500} e^{-t/420} dt}{\int_0^{\infty} e^{-t/420} dt} = .7 \tag{4.8}$$

And

$$N_{atoms} = n_0 * L * \int \frac{f(v,T)}{v} dv = n_0 * L * \int_0^{\infty} \frac{v^3}{2\overline{v}^4} * e^{-\frac{v^2}{2\overline{v}^2}} * \frac{1}{v} dv \tag{4.9}$$

Here n_0 is the (unknown) flux in the collection region, $\overline{v} = \sqrt{k_B T/M}$, and L is the length of the collection region. An assumption here is that the collection region is a sphere, much smaller than the region of overlap between atoms and the probe beam. The result of this calculation is:

$$N_{atoms} = \frac{1}{2} * n_0 * L * \sqrt{\frac{\pi M}{2 k_B T}} \tag{4.10}$$

The next step is to calculate the excited state fraction, ρ_{ee}. The following treatment comes from Metcalf 2.25 [42]:

$$\rho_{ee} = \int_{-\infty}^{\infty} \frac{s_0/2}{1 + s_0 + 4\frac{\delta^2}{\gamma^2}} d\delta = \frac{\pi s_0 \gamma}{4\sqrt{1+s_0}} \tag{4.11}$$

We can now combine each of these equations to arrive at the relation between the measured spectrum and the atomic flux:

$$Integral\ of\ spectrum = \frac{1}{2} * n_0 * L * \sqrt{\frac{\pi M}{2k_B T}} \frac{\pi s_0 \gamma}{4\sqrt{1+s_0}} D * f * \eta * \tau \tag{4.12}$$

We usually integrate 500,000 cycles, with a collection efficiency of $\eta = .005$ (10% quantum efficiency, 1% lens collection efficiency, and an interference filter with 50% transparency), and τ is .5 seconds. The last piece of the puzzle is to convert n_0, the atom number through the viewing region, to the total atomic flux F. The viewing region is expected to be about 3mm (the size of the PMT viewing region, as it is imaged roughly one-to-one onto the atomic beam by the lens), which is much smaller than either the atomic beam diameter or the probe beam diameter. To better estimate the viewing region, we use the beam fluorescence spectra to determine the doppler width, allowing us to determine the velocity spread of atoms detected. This allows us to determine the opening angle of the viewing region. The doppler width is measured to be 5.8 MHz, which compared to the maximum doppler shift of 426 MHz for a 300 m/s atomic beam corresponds to an open angle of 13.6 mrad. The known 27 cm distance from the viewing region to the end of the oven nozzle allows us to estimate the actual size of the viewing region to be 3.6 mm.

To determine the relation between the number of atoms in the viewing region to the number of atoms in the beam, we need to know the angular distribution of the atomic beam. The Ra nozzle is 8.3 cm long and 0.15 cm in diameter; from this we expect an approximate half-angle of 18 mrad. To determine the distribution more accurately we use two models: a theoretical model given in Ref [43] and a monte carlo simulation written by David Potterveld. In the monte carlo, the output of the effusive oven is determined by considering a single atom placed on a wall in the source region, leaving the wall with a velocity given by the Boltzmann distribution. The atom will travel ballistically until it encounters another wall (at which point it will again leave with a velocity given by the Boltzmann distribution) or exits through the nozzle. Each time the atom hits a wall, the exit velocity is given by the temperature of that wall. Interactions between

atoms and roughness of the walls are neglected in this model. To see if this assumption is justified, we use the size of radium and barium atoms (both about 2 angstroms), and an estimated number density of barium atoms in the oven, to get the mean free path $l = \frac{1}{n\sigma}$ in the oven, shown in Figure 4.7. This calculation assumes hard core scattering.

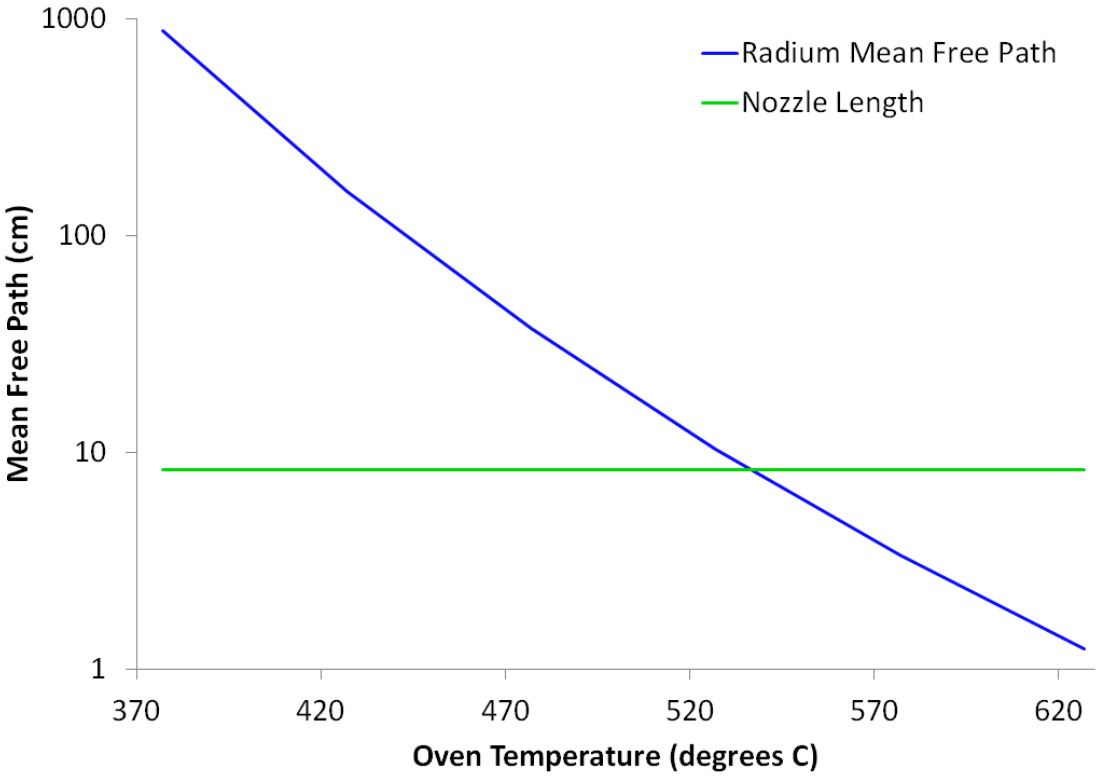

FIGURE 4.7: Mean free path of radium in the oven as a function of oven temperature, limited by collisions with barium. Once the mean free path becomes smaller than the nozzle length collisions become important to the angular distribution; we typically operate around 500^{o}C.

To determine the validity of the monte carlo, two atomic systems were simulated: the ^{88}Sr trap at JILA, which is well understood, and the Ra trap at Argonne. The Sr oven nozzle is 2 cm long and 2 mm in diameter. The angular distributions (measured from the tip of the nozzle) predicted by the monte carlo and the analytic function for both species are given in Figure 4.8. From the small-angle part of the figure the benefit to using a long, thin oven nozzle is clear.

The flux conversion can be found by integrating the atomic beam distribution at the viewing region. The measured atom beam flux is predicted to be 0.12% of the total atom flux, which varies between 2 x 10^9 and 2 x 10^{10} atoms per second for a typical ^{226}Ra load (dependent on operating temperature, age of the oven, and initial activity

loaded into the oven). The flux calculated this way agrees within a factor of 2 to the flux estimated by comparing the total number of atoms loaded into the oven to the actual "lifetime" of an oven (typically about 3 months, operating 8 hours a day, with effort made to keep the MOT size fairly constant). A simplified version of the code used to convert the beam fluorescence signal into a flux of atoms out of the oven is included in Appendix E.

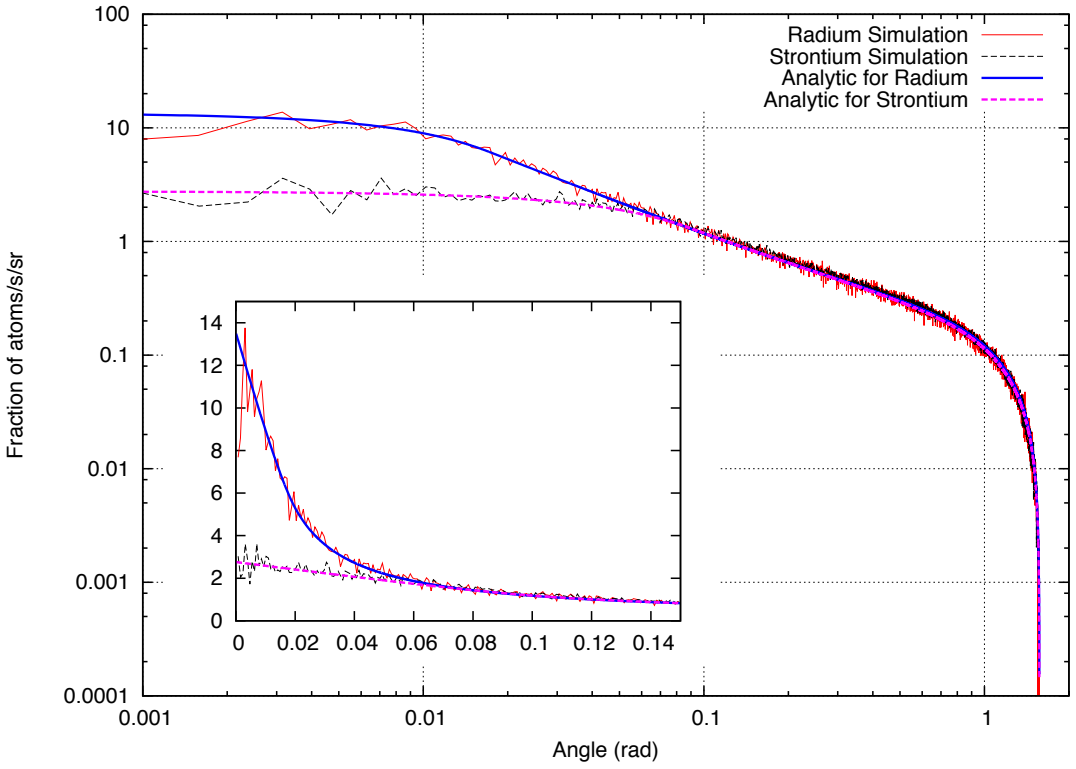

FIGURE 4.8: The predicted angular distribution of the atomic beam, for the oven geometry used in the radium experiment. A monte carlo simulation and analysis for a strontium experiment are included in the figure. The inset shows the angular distribution on a linear scale.

When a crucible is first loaded, generally the barium inside will have a small layer of barium oxide around it that will prevent atomic barium from being released at reasonable temperatures (400-500 ^{o}C). While we could operate at high oven temperatures exclusively, it is better for the pressure in the system (and thus the lifetimes of the traps) to use a low oven temperature. Therefore the barium oxide layer is "cracked" apart by running briefly at high temperature–this produces a sudden large flux of atomic radium which is easily detectable by the beam flux system. After this crack the oven can be operated at much lower temperatures with sufficient flux. The key to this procedure is to fully break apart the oxide layer without using up a large amount of the loaded radium

in the process, as these temperates can produce a radium flux hundreds of times larger than is used under regular "operating" conditions. The exact temperature at which the crack occurs varies (likely due to the varying thickness of the barium oxide layer), but is usually around 570C. A "textbook" crack is shown in Figure 4.9.

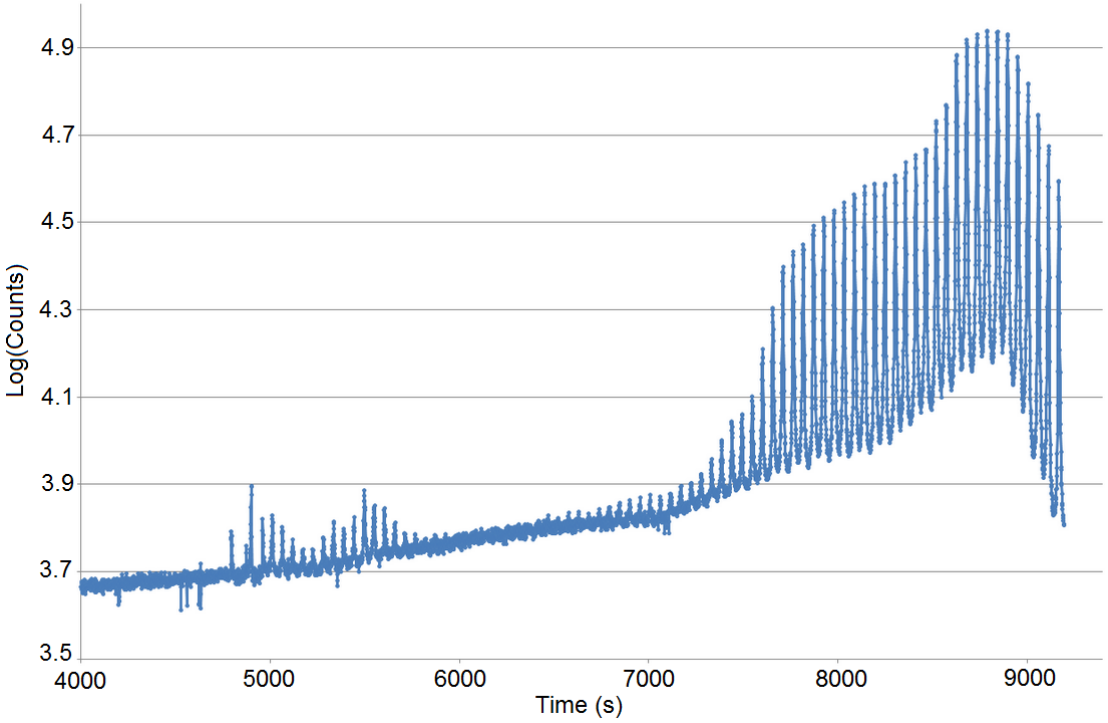

FIGURE 4.9: Beam fluorescence signal from a recently-loaded oven (4.6 μCi of ^{226}Ra). The temperature of the oven is ramped gradually over the course of about six hours from room temperature to 600 degrees C. Time t=0 s here refers only to when the fluorescence program was started. A few "burps" of signal can be seen at t=5000 s, corresponding to an oven temperature of about 430 degrees C. The crack itself occurs at t=8800 s, at an oven temperature of about 570 degrees C. At this point the temperature is rapidly decreased.

4.4 Loading into a 3D MOT

While it is possible to directly load the atomic beam into a 3D MOT, it would be very inefficient. This is due to the roughly 500^{o}C temperature of the beam and the approximately 2 meter distance between the oven and the MOT. To vastly improve the efficiency of the system, three stages are added between the oven and MOT to reduce the longitudinal and transverse velocities of the atoms. From oven to MOT, these are the Transverse Cooling, 2D Focusing, and Zeeman Slower. A diagram of the full apparatus can be found in Figure 4.10.

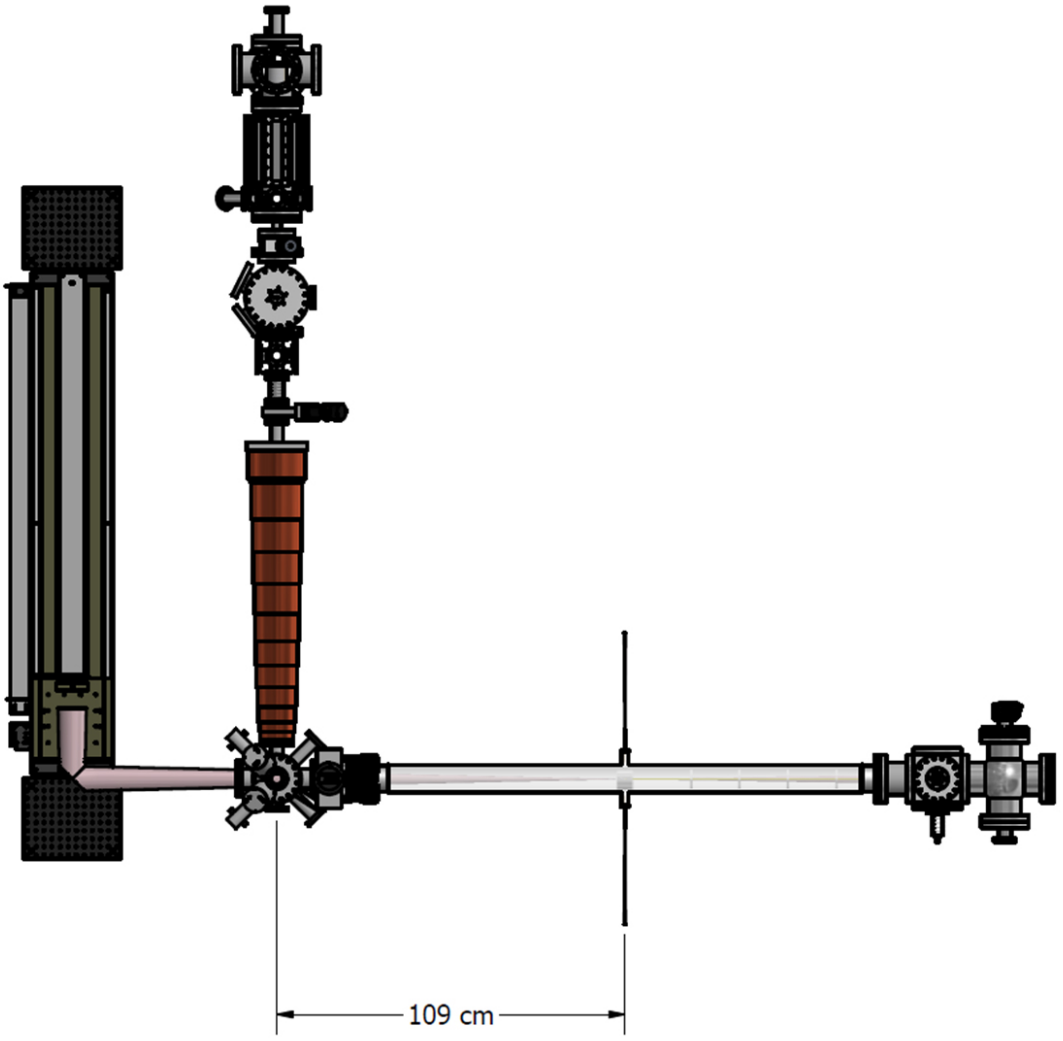

FIGURE 4.10: Diagram of the entire experimental vacuum system. On top is the "oven end", with the atomic beam traveling toward the bottom of the image into the MOT chamber. The vacuum system then takes a 90-degree turn into the Science Chamber (the magnetic shielding is not displayed here for clarity).

4.4.1 Transverse Cooling

The transverse cooling stage uses about 150 mW of 714 nm light, expanded to be about 2 cm in diameter. The beam is split in two, with one intended to cool the horizontal dimenion and the other to cool the vertical dimension. Each dimension has two long mirrors outside the vacuum system, allowing the beams to bounce through the chamber about 10 times with a variable shallow angle.

The gain in 3D MOT laoding rate due to each transverse cooling dimension is typically about 7; the total transverse gain is about 60. It is worth keeping in mind that the gain

from the transverse cooling is reduced in the presence of a large external magnetic field, as the laser will decouple from the atoms. Therefore there are two large bias coils on the two sides of the transverse cooling chamber to cancel out any external field. Fortunately the transverse cooling gain is identical (within uncertainty) between ^{226}Ra and ^{255}Ra.

4.4.2 2D Focusing

Between the transverse cooling stage and the Zeeman Slower, a 2D focusing stage was added. Simply a 2D MOT, the purpose of this stage is twofold: it negates the effect of transverse heating in the Zeeman Slower, and allows us a way to compensate for a misalignment in the transverse cooling and/or the oven nozzle.

To choose the correct magnetic field gradient and laser parameters, a simple 1D simulation was written to approximate the 2D focusing stage. The gradient it predicted was optimum, about 0.5 G/cm, was found experimentally to be correct. However, a large bias magnetic field was required as well, likely due to a combination of both an external magnetic field and poor alignment of the transverse cooling stage. The MATLAB code for the simulation can be found in Appendix A.

The gain of the 2D focusing stage varies wildly (as high as 4 and as low as .5), and is mostly determined by how well the transverse cooling is aligned and optimized. Therefore, the 2D focusing stage is often not used, and greater care is used on the transverse cooling optimization. This is done so that the power otherwise used for the 2D MOT can be used for something else. However, due to its utility (as providing extra degrees of freedom should they be needed) it is always kept available.

4.4.3 Zeeman Slower and Slower Repump

The Zeeman Slower uses a variable magnetic field (see Figure 4.12) to keep atoms on resonance as they are decelerated by the 714nm beam. The maximum acceleration for the 714 nm transition is about 3000 m/s^2, which means it can slow atoms up to about 60 m/s. As the practical efficiency of the slower improves with the uniformity of the laser beam and the overall intensity, the beam is expanded to be a few centimeters in radius, with a saturation number of about 30. As the most probable velocity of the thermal atomic beam is 250 m/s, a maximum of only about 3 x 10^{-3} of the atomic flux can

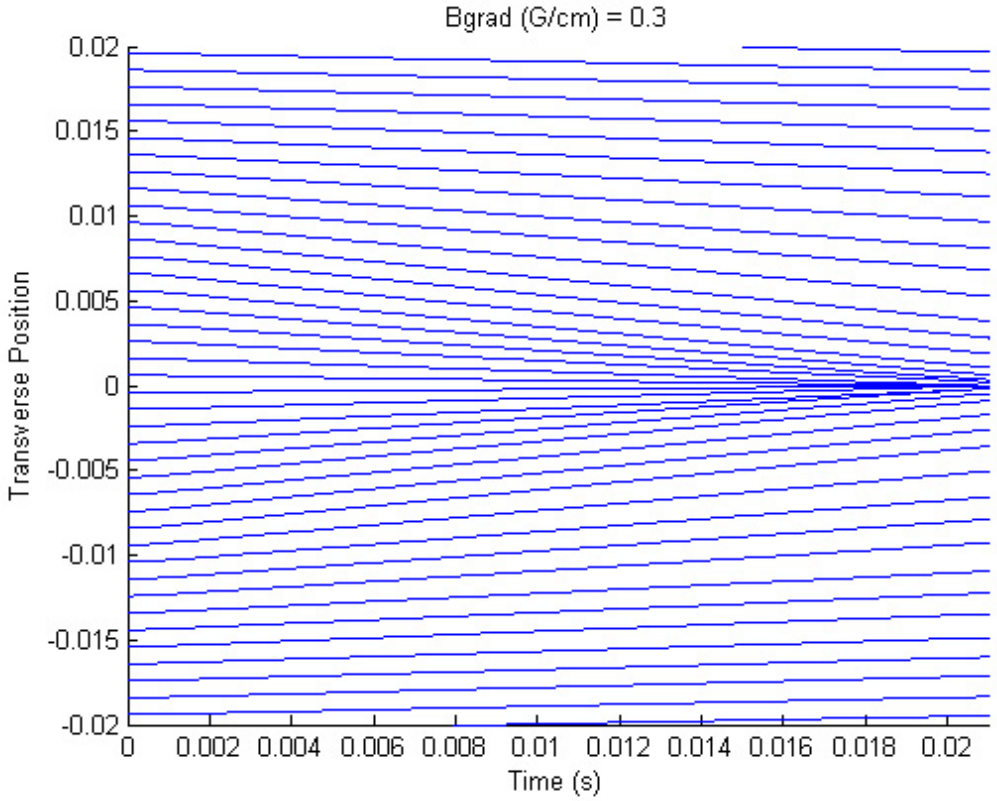

FIGURE 4.11: Simulation of the 2D Focusing stage. The simulation shows that the narrow linewidth of the intercombination transition limits the number of atoms that can be focused correctly–the use of a broader (but not leaky) transition would improve its effectiveness.

be slowed. The "gain" of the Zeeman Slower is so large that it has never been directly measured. It is worth noting that this efficiency could be improved dramatically if the maximum acceleration could be increased through the use of a stronger transition, and a significant amount of work has been done to develop a scheme for slowing using the stronger 483nm transition–which is made difficult due to the repumping needed.

As a general tool to understand the dynamics of the laser cooling and trapping system, a simple rate equation model was written in Mathematica (which can be found in Appendix C). A simple coupled ODE model, it makes the assumption that all states are trapped, and calculates the population transfer under various illumination conditions. This assumption is valid in the ODT (as the only untrapped state is $^1P_1$, which has a very short lifetime) and is also reasonable in the transverse cooling and zeeman slower (as there is no true "trap"). Transition rates are taken from Bieron et al [39]. Both spontaneous decay and stimulated emission are included. The model allows the user to

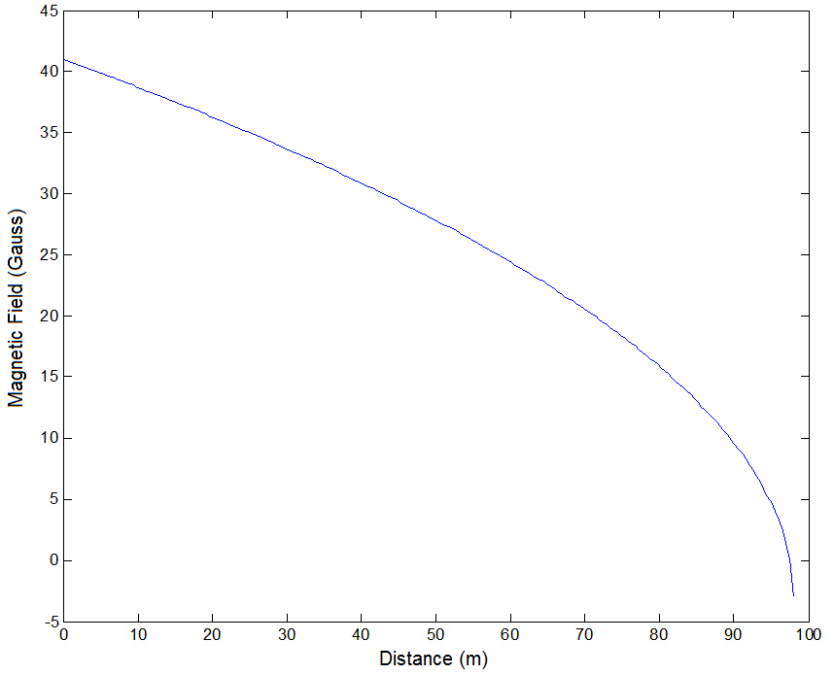

FIGURE 4.12: Analytic model of the longitudinal magnetic field, calculated from the coil geometry and currents used in the actual experiment. Note that the magnetic field of the 3D MOT coils must also be included.

include the effects of repumping due to blackbody radiation and the ODT. An easy way to demonstrate the utility of the model is to calculate the population dynamics if the atoms are illuminated by 714 nm light (S=20) with blackbody repumping on, which is the situation in the zeeman slower. As can be seen in Figure 4.13, the population in the metastable states ($^3D_1$ and $^3P_0$) builds up over time, becoming dominant after about 20 ms. As a trappable atom in the slower will travel no faster than 60 m/s, the time an atoms spends in the slower will be at least 17 ms; this means that a significant number of atoms will be lost to the metastable states by the time they reach the MOT Chamber (further, the more time an atom spends in a metastable state the more likely it is to decouple from the slower and thus be insufficiently slow by the time it reaches the MOT chamber). To address these issues, the more powerful of the two 1428 nm repump lasers (the New Repump as it is called) was made to be the same size as the 714 nm slower beam and sent down the slower pipe. This is expected to reduce the population lost to metastable states, demonstrated in Figure 4.14. The addition of this Slower Repump laser improved the loading rate of the MOT by a factor of about 3.

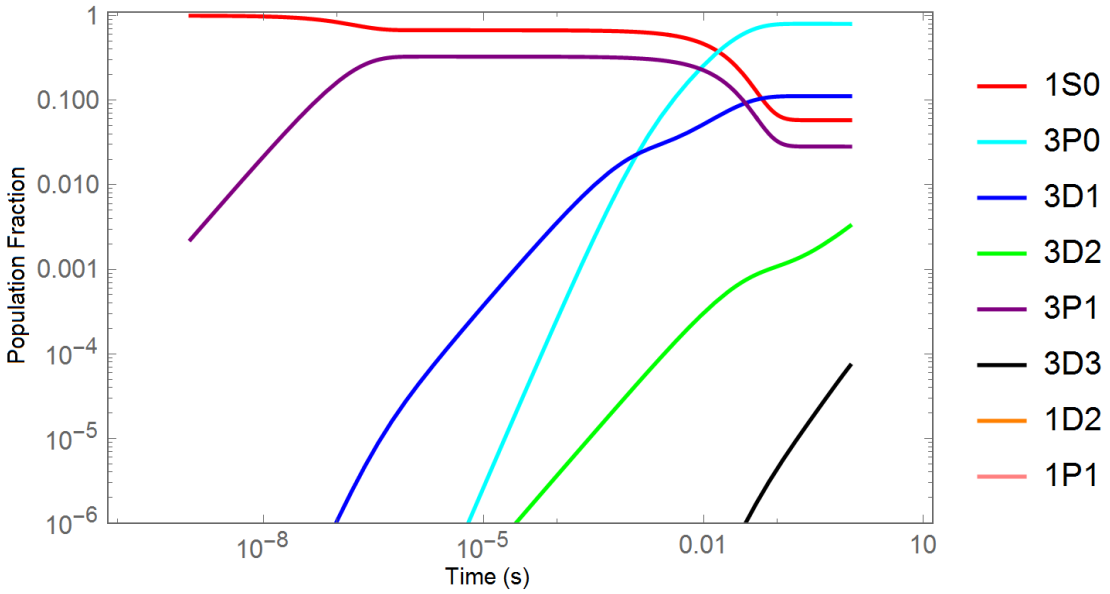

FIGURE 4.13: Population dynamics in the Zeeman Slower without the use of a repump laser. The red curve is the ground state population and the purple curve is population in $^3P_1$; over time the atoms are pumped to long-lived metastable states.

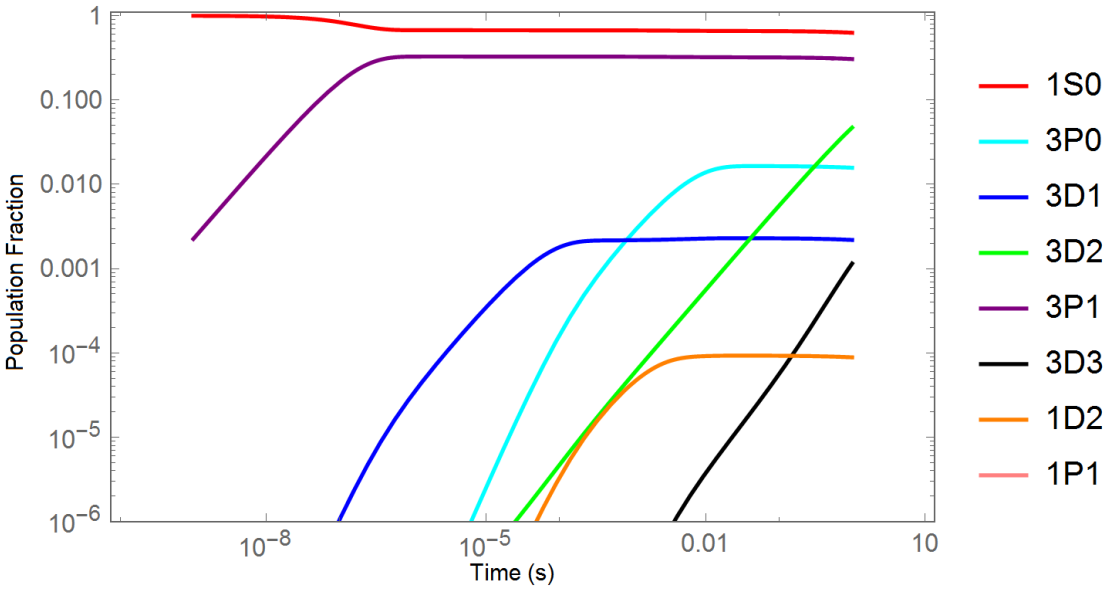

FIGURE 4.14: Population dynamics in the Zeeman Slower with the use of a repump laser. Note that, as expected, the fraction of atoms lost in $^3D_1$is heavily suppressed.

4.4.4 3D MOT

The radium MOT is formed by two coils in anti-helmhotlz configuration, with three trim coils to cancel out external magnetic fieds. Both 1428 nm lasers hit the MOT, usually with identical frequencies–the "old repump" is oriented vertically and the "new repump" interacts with the 3D MOT and then continues down the Zeeman Slower tube. The radium MOT is described in more detail in [38]. The stainless steel parts of the vacuum system in the MOT Chamber have been "heat treated" to reduce outgassing. Each part is put in an oven and heated to about 400 ^{o}C for 10 days; this results in a pressure in the MOT Chamber of mid-10^{-10} Torr. Trap lifetimes exceed 30 seconds, and at large detunings can be as large as 60 seconds.

We operate the MOT in two primary configurations. The first, named "Load", uses a weak (about 0.5 G/cm) magnetic field gradient and high intensity, large detuning laser beams so that the capture volume is large and the trap is deep. This configuration, however, is poor for detection because there is a great deal of background 714nm light and the atoms are loaded into a diffuse cloud several millimeters in diameter. The second configuration, named "Probe", uses a stronger magnetic field gradient (typically 2-6 G/cm) and lower intensity beams closer to resonance. This configuration squeezes the atoms into a diameter of about .6mm and decreases the amount of background laser light, providing much higher per-shot SNR. The 3D MOT is imaged by a lens inside the vacuum system onto an Andor Luca-R CCD camera (10% quantum efficiency).

4.5 MOT-to-ODT Transfer

The ODT is formed by the 50W (far-off-resonance) 1550 nm fiber laser, at the focus of a 4-inch-diameter lens, with a focal length of 2 meters. The beam is expanded by an initial telescope to fill nearly the entire lens. The diffraction limit for such a system is a waist of about 60 μm, but due to imperfections in the alignment, a waist of 100 μm diameter is typical. This will be discussed further in the section on Astigmatism below. As the beam is 50 W, dielectric mirrors are needed to avoid thermal lensing. To avoid clipping of the beam on its path, the dielectric mirrors are 6 inches in diameter.

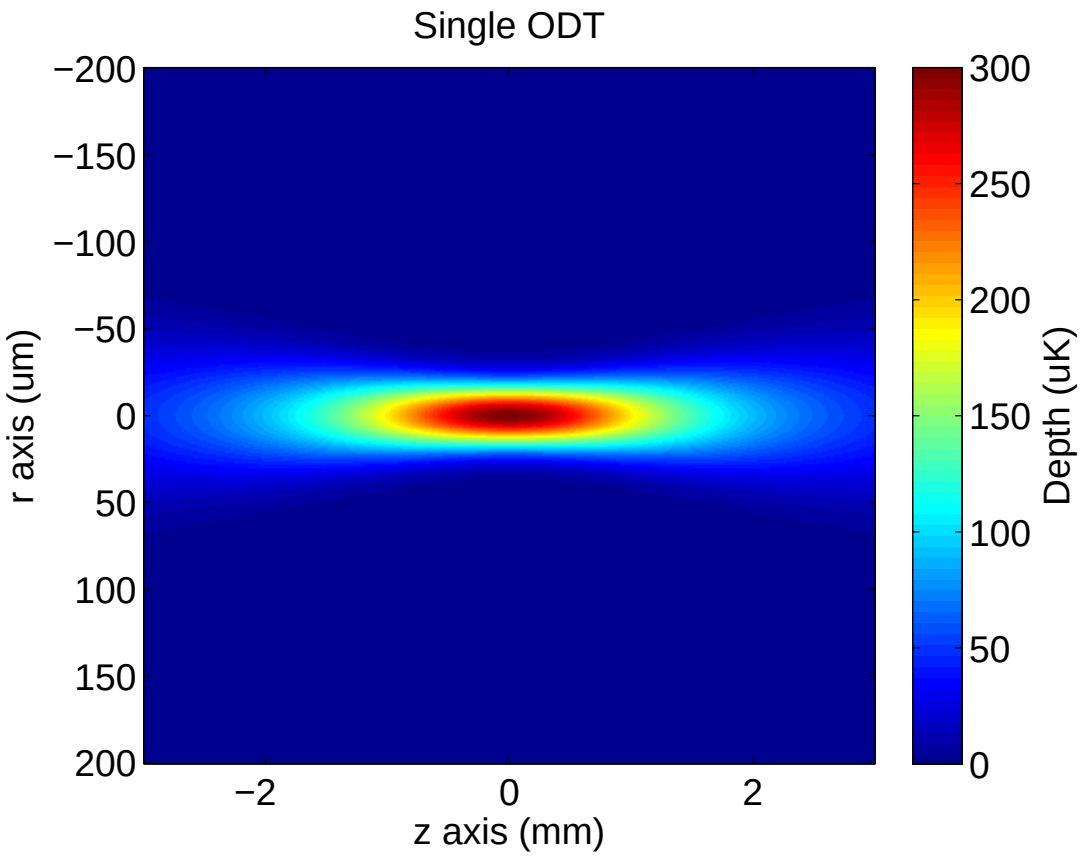

FIGURE 4.15: Analytic model of a diffraction-limited traveling-wave ODT.

4.5.1 Temperature Measurements

The expected depth of the ODT is approximately 500μK, as given by the following formula:

$$U_0 = -\frac{1}{4}\alpha E_0^2$$

Here U_0 is the trap depth, α is the AC polarizability of the ground state at 1550 nm, and E_0 is the electric field of the ODT laser. This is only approximate because it depends on a calculated value of α and knowledge of the electric field the atoms experience, which is sensitive to optical alignment. To determine the actual ODT depth, we perform an experiment in which we slowly reduce the power in the ODT, wait for some time, then turn it back to full power. The idea here is that the hottest atoms will be lost from the trap, so the fraction of atoms in the trap surviving after this will provide information about the energy distribution. Effectively this maps out the Boltzmann distribution.

Following the treatment in [44], we write the normalized energy distribution of the atoms as

$$f(E) = \frac{1}{2(k_B T)^3} E^2 e^{-E/k_B T} \tag{4.13}$$

Here T refers to the atom temperature. The probability that an atom will have an energy less than E is given by

$$P(E) = \int_0^E f(E')dE' = 1 - (1 + \frac{E}{k_B T} + \frac{1}{2}(\frac{E}{k_B T})^2)e^{-E/k_B T} \tag{4.14}$$

This equation is the probability that an atom will remain in the ODT after the depth is decreased. Note that as this formula is a function of the ratio $\frac{E}{k_B T}$, this sort of measurement cannot directly give the ODT depth. However, using this technique to determine the ratio of ODT depth to atom temperature, and using time-of-flight thermometry with the MOT to get the atom temperature directly, we can extrapolate the ODT depth. These measurements typically give an ODT depth of 300-400 μK.

4.5.2 Timing Sequence

The temperature of the 3D MOT in the Probe configuration is about 1 mK, determined by time-of-flight measurements. So it is immediately apparent that the efficiency of transferring atoms from the Probe MOT to the ODT will be very poor, simply due to energy conservation. Therefore we introduce a third configuration of the MOT, named the "Cool" MOT, which is optimized not for imaging SNR but for temperature (as determined by time-of-flight measurements and MOT-to-ODT transfer). The Cool MOT uses very low intensity 714 nm light, with similar detuning and magnetic field gradient to the Probe MOT. The Cool MOT is overlapped with the bus ODT with the 3 trim coils, for about 200 ms. We typically cool the atoms to about 40 μK, which is sufficient for at least 80% transfer efficiency into the ODT. An image of the ODT properly aligned to the 3D MOT is shown in Figure 4.16.

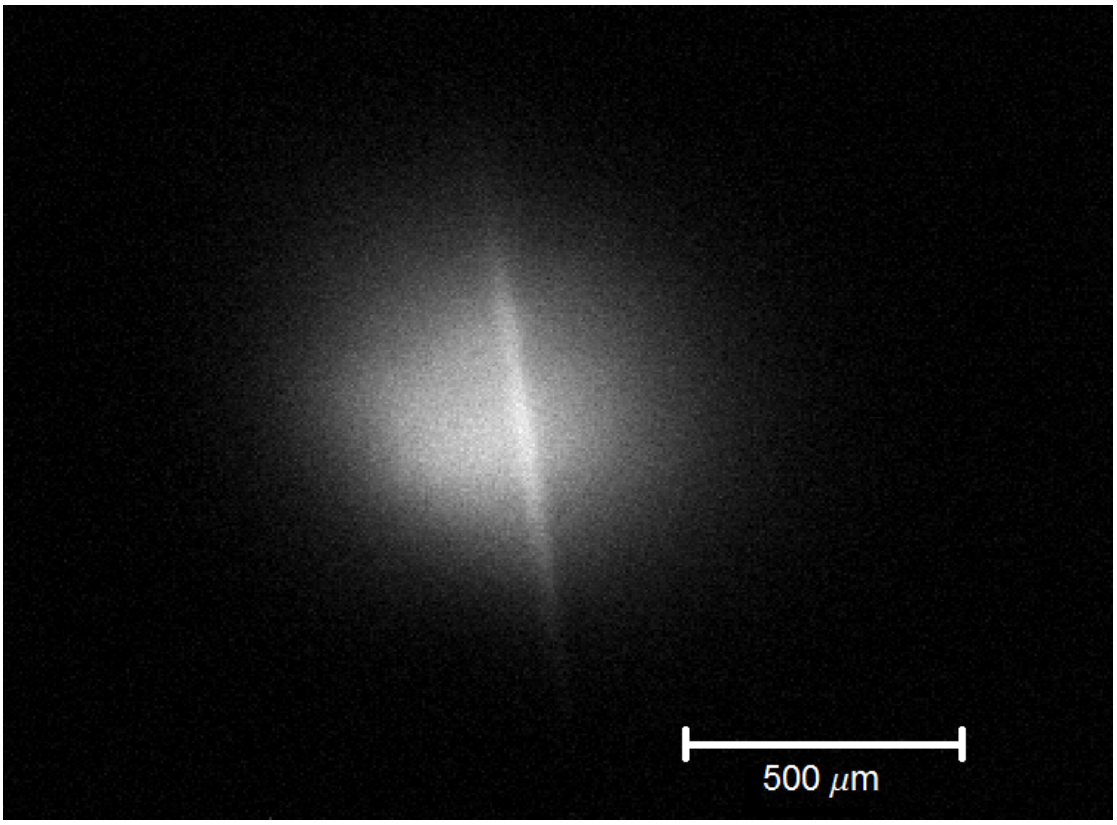

FIGURE 4.16: The ODT overlapped with the 3D MOT. The relative brightness of ODT compared to the MOT is a crude measure of the fraction of atoms loaded into the ODT, and therefore the atom temperature.

4.6 ODT Transport

After atoms are loaded into the bus ODT, they need to be moved 1 meter away to the center of the science chamber, between the high voltage electrodes. Of course, this must be done as efficiently as possible. The sinusoidal motion profile shown in Figure 4.17 was chosen experimentally, as it gave the highest transport efficiency. Other motion profiles were tested–triangle-wave, parabolic, minimal-jerk, etc.—but all were worse than or equivalent to a simple sinusoidal motion profile, shown in Figure 4.17. Note that the acceleration profile is discontinuous; this results in atom loss due to the motion itself but is faster than "smoother" profiles with the same maximum acceleration, thus resulting in less atom loss due to background gas collisions.

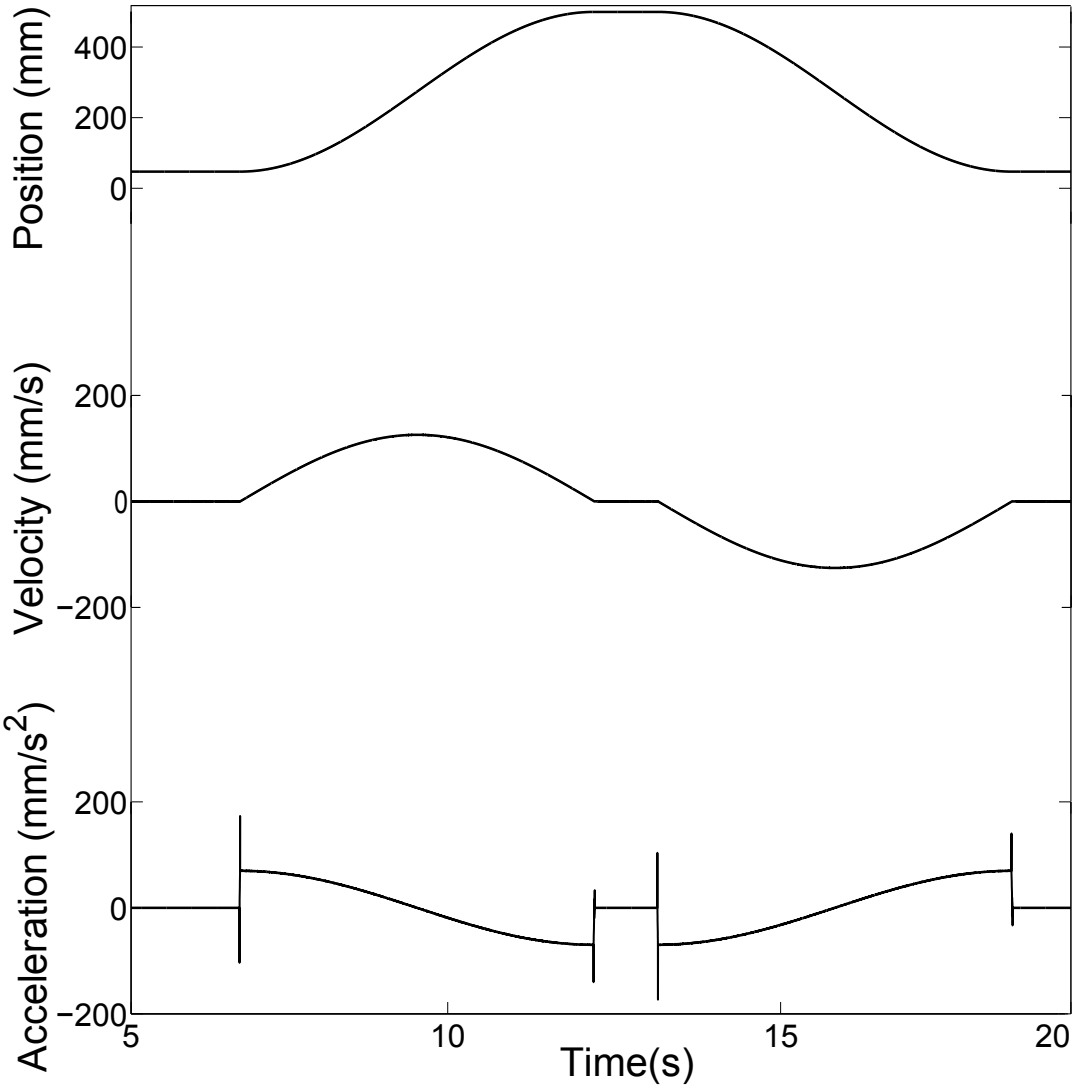

FIGURE 4.17: The motion profile used in the EDM experiment.

4.6.1 Simulations

As no atomic physics experiment before has tried to transport atoms 1 meter in an ODT, and particularly as efficiency is critical to the radium experiment, it is important to understand the dynamics of transport. In particular it is valuable to understand the sensitivity of the transport efficiency to the motion profile, trap frequency, trap depth, initial atom temperature, and noise in the motion. A monte carlo simulation was written so that the motion profile and beam characteristics could be optimized. The simulation chooses atoms from a thermal distribution and tracks them as the potential moves, evaluated with a Runge-Kutta algorithm. The simulation includes only the longitudinal

dimension for computational simplicity; one of the first questions to answer is whether all of the important dynamics can be encapsulated in only the longitudinal dimension. This is not immediately obvious, as one might expect that tranverse vibrations might dominate atom loss. The code for the simulation is given in Appendix B. Figures 4.18 and 4.19 demonstrate characteristic atom trajectories for successful and unsuccessful transport respectively.

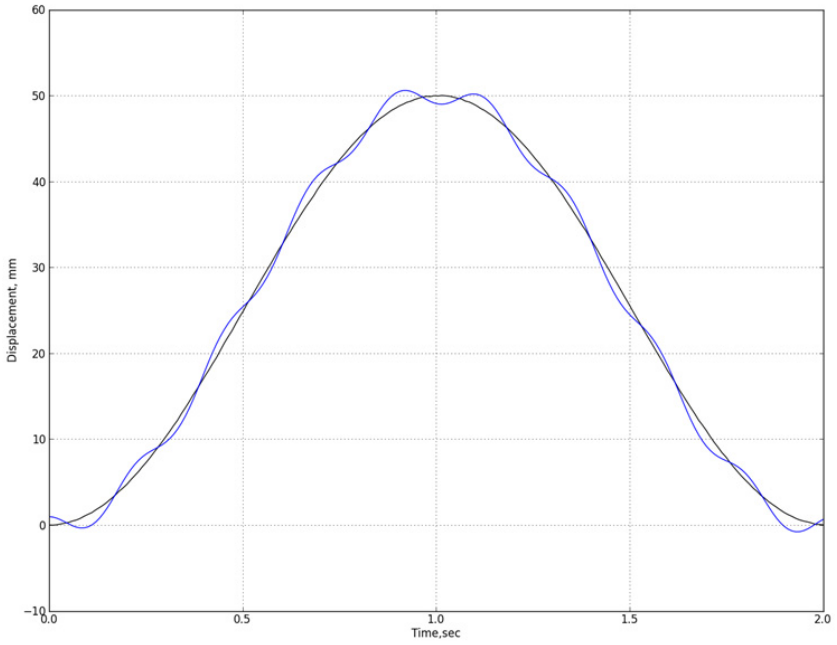

FIGURE 4.18: Trajectory of a single atom as the stage moves. The black curve is the trajectory of the potential minimum; the blue curve is the atom as it follows. Note that the deviation of the atom from the potential minimum increase as the stage accelerates and decelerates.

4.6.2 Experiment

Before drawing conclusions from the simulation, we perform a series of experiments to compare with the simulation, using shorter transport distances to improve the signal-to-noise. As the trap depth is not well known, it is left as a fit parameter. A comparison of simulation and experiment is shown in Figure 4.20. Although it is straightforward to include a constant (time-independent) loss rate into the simulation to mimic the effect of background gas collisions, for understanding the transport dynamics it is best to normalize out the vacuum effects in the data for comparison. To avoid the problem of sampling large pressure gradients (resulting in non-uniform vacuum loss rate), we take data only up to 300 mm (this also helps with the statistics of the measurement.

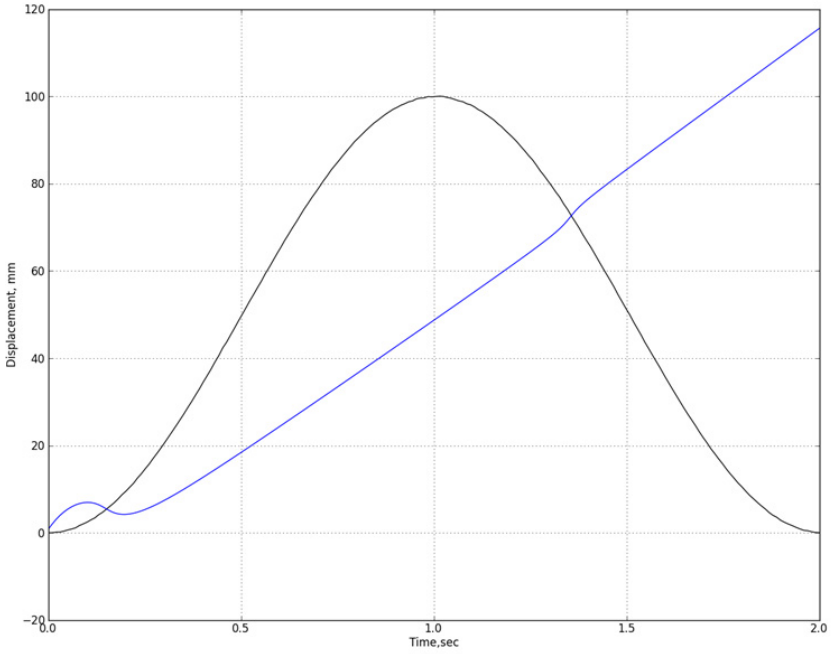

FIGURE 4.19: Trajectory of a single atom that becomes unbound during the motion. Atom loss is most likely to occur at the turning points of the motion.

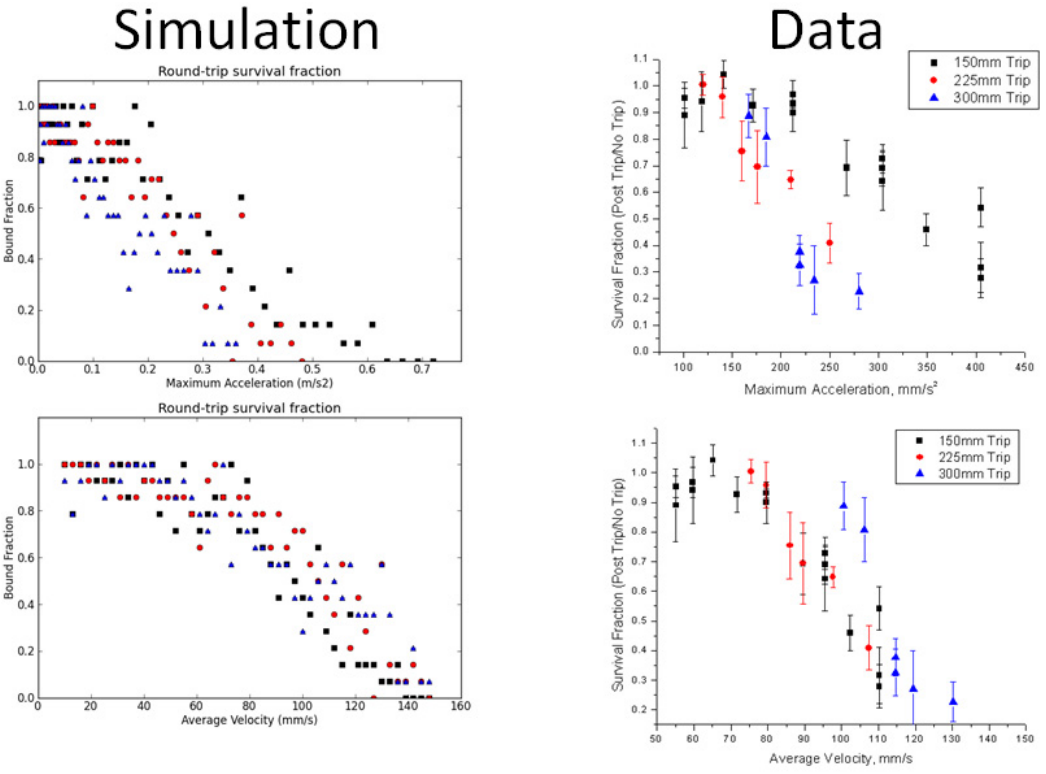

FIGURE 4.20: Comparison of experiment and simulation. The agreement is reasonable, indicating that the most important dynamics are likely constrained to the longitudinal dimension.

From the simulation we learn that the transport efficiency is not very sensititve to the intial atom temperature, or noise-like vibration in the longitudinal axis. To develop a simple guide to determine the parameters most important to transport efficiency, we compare a characteristic parameter of the trap itself with a characteristic parameter of the motion profile. We begin by introducing the trap frequencies, which in a harmonic approximation of the trap potential are given by:

$$\omega_z = \sqrt{\frac{2U_0}{mz_R^2}} = \sqrt{\frac{2U_0\lambda^2}{m\pi^2\omega_0^4}}$$

and

$$\omega_r = \sqrt{\frac{4U_0}{mw_0^2}}$$

Here ω_z and ω_r are the longitudinal and radial trap frequencies, m is the atom mass, and z_R and w_0 are the longitudinal and radial waists respectively, with

$$U_0 = \alpha I = \frac{2\alpha P}{\pi\omega_0^2} \tag{4.15}$$

where α is the polarizability and I is the intensity of the light.

We define a "cutoff" time to be the transport time that results in the loss of 90% of the original atom number. For a given longitudinal trap frequency, we can run the simulation to determine the corresponding cutoff time for a variety of transport distances. Each motion profile has a characteristic acceleration given by the distance and transport time. By running the simulation over a variety of experimental parameters (the Rayleigh Length zR, the trap potential depth U_0, the ODT power, and the transport distance), we find a general linear dependence which relates the characteristic acceleration the atoms experience in the trap when there is no motion to the acceleration of the trap center when there is motion. As one would expect, as the trap frequency is increased the atoms can survive larger transport accelerations. Figure 4.21 shows that when only the two characteristic acceleration parameters are considered, the dynamics are highly insensitive to the specific experimental parameters used. This allows us to write a general rule of thumb for the minimum amount of time T_{min} one can perform the transport with significant (*i.e.* $> 10\%$) efficiency:

$$T_{min} \approx \sqrt{\frac{D}{z_R \omega_z^2}} = \frac{\pi \omega_0^2}{2} \sqrt{\frac{Dm}{\lambda \alpha P}} \tag{4.16}$$

where D is the transport distance, ω_z is the longitudinal trap frequency, and z_R is the Rayleigh Length. Note that on the right hand side the only parameter the experimenters can easily control is ω_0, the transverse waist. Therefore reducing the transverse waist is crucial to efficient transport, and our campaign to reduce astigmatism in the beam is discussed below.

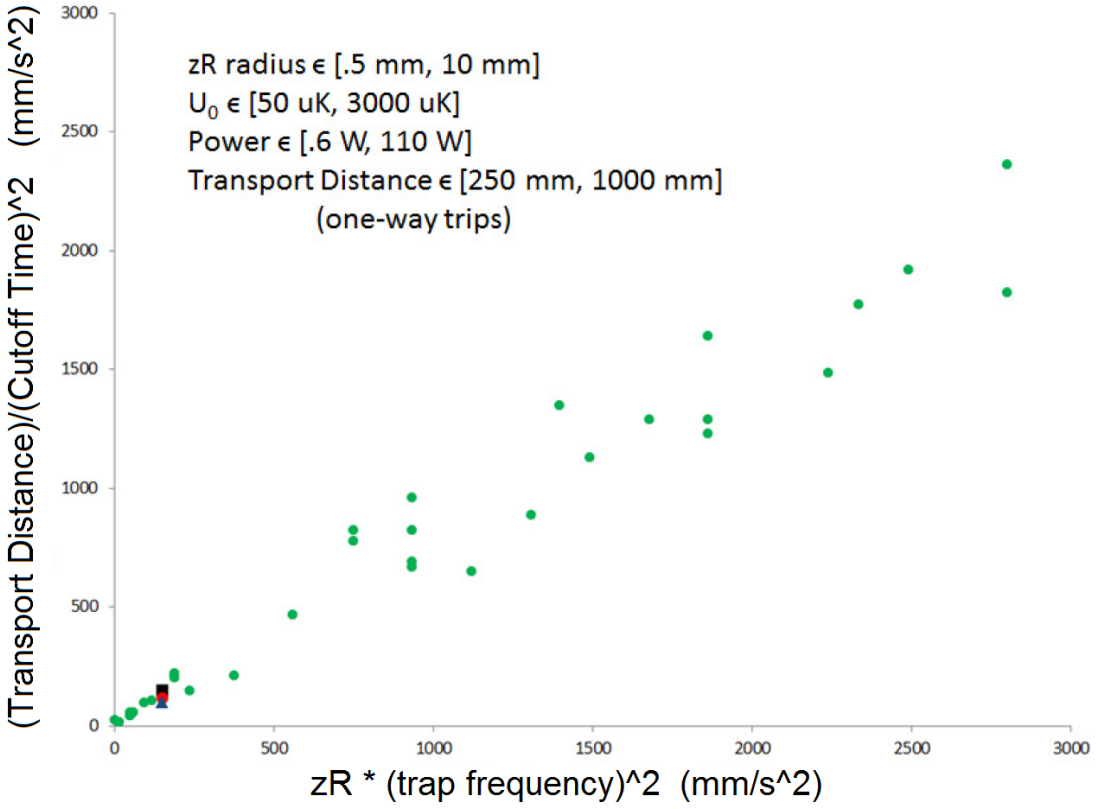

FIGURE 4.21: This plot shows the "phase transition" above which transport-induced losses exceed 90%. As one might expect, longitudinal trap frequency plays a large role in determining how quickly the transport can be done. The green points are from the simulation, the other 3 are experimental data.

Due to the difficultly in improving the trap frequency a rigorous comparison of the dynamics in the actual apparatus with the simulated results in Figure 4.21 has not been performed; therefore the results remain primarily an intellectual guide. We find in practice that the optimum transport time is 5.764 s, where the losses due to the lifetime in the ODT (discussed in the next chapter) and the losses due to the motion are balanced. Nonetheless, it has consistently been observed that poor transport efficiency

is often explained by an ODT waist size much larger than the diffraction limit, which can then be improved with alignment.

4.6.3 Discussion of Loss Mechanisms

For intellectual simplicity, it is convenient to separate the loss mechanisms into those that occur whenever atoms are loaded into the ODT, and will therefore occur regardless of the motion, and those due specifically to the motion. The simulation discussed in the previous section describes the losses due to the motion, but neglects the other loss mechanisms in the ODT. The primary loss mechanisms we face are losses due to background collisions, losses due to pointing noise, and losses due to intensity noise. In the presence of these mechanisms, the energy distribution of atoms over time is given by the Fokker-Planck equation [45]:

$$\frac{\partial n(E,t)}{\partial t} = (\frac{\Gamma}{4}E^2 + \dot{Q}E)\frac{\partial^2 n(E,t)}{\partial E^2} - \dot{Q}\frac{\partial n(E,t)}{\partial E} - \frac{\Gamma}{2}n(E,t) - \Gamma_{Vac}n(E,t)$$

We see that the atoms will both increase in energy over time and that their energy distribution will become broader over time. As the ODT is a shallow conservative potential, this broadening of the enegy distribution will lead to trap losses. In this analysis, it is assumed that background gas collisions are not a source of heating, only a loss mechanism, similarly justified by the shallow trap depth. While it is possible to measure pointing noise and intensity noise directly, it is also possible to determine which effect dominates by measuring the time dependence of the atom loss from the ODT directly, and extract the relevant parameters from the fit. Figure 4.22 shows an example data set and the resulting fit if one assumes that all the losses are given by background gas collisions. Clearly this assumption misses important dynamics. Figure 4.23 shows the same data, now including both vacuum losses and heating due to pointing noise. The agreement is much better; while this does not conclusively demonstrate pointing noise is a loss mechanism in our experiment, it would explain the behavior we observe. The fit predicts a vacuum-limited lifetime of 80 seconds. Adding intensity noise to the fit does not improve the chi-square significantly; the intensity-noise-limited lifetime determined from the fitting was found to be at least 200 seconds. Therefore it was possible to explain the dynamics completely with only pointing noise and vaccum losses.

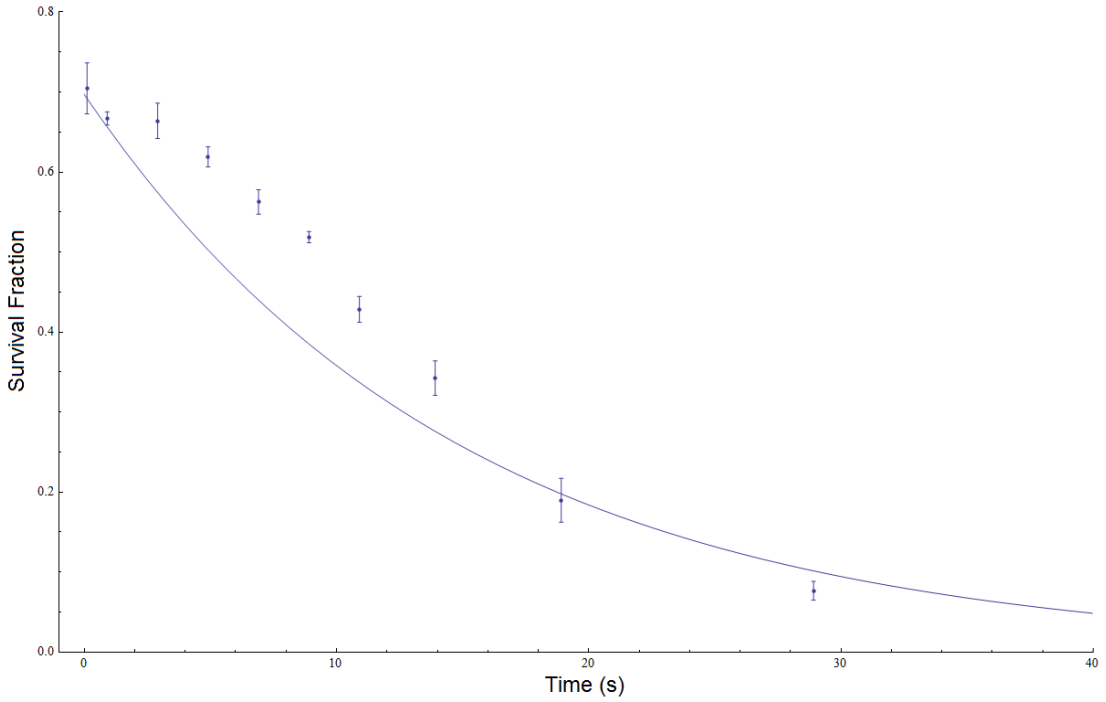

FIGURE 4.22: Atom loss in a stationary ODT. The fit includes only vacuum losses, and is clearly missing some important dynamics.

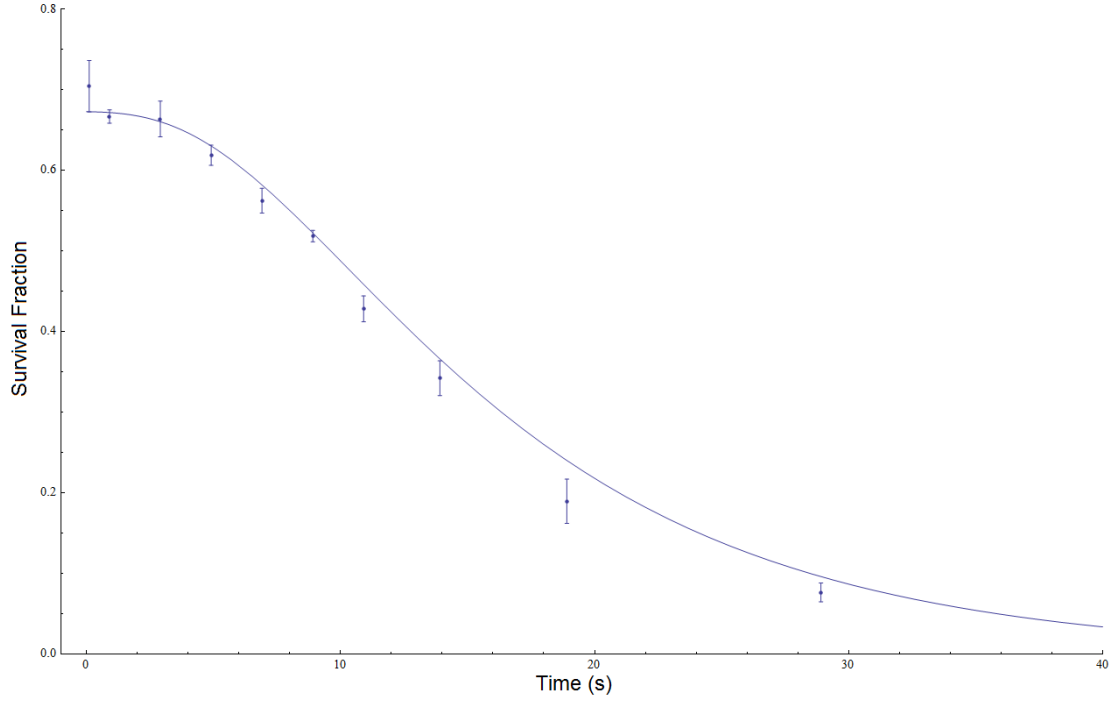

FIGURE 4.23: Atom loss in a stationary ODT. The fit now includes both vacuum losses and pointing noise, and agrees well with the data.

Once it was realized that pointing noise may be a serious problem, many of the optics were replaced with larger 6" optics (to reduce clipping, thereby increasing the trap depth) and vibtration-damped mounts (to reduce pointing noise). Currently, the lifetime in the "bus" ODT is typically about 12 seconds. Transport efficiency is optimized when the losses due to the motion are balanced by the losses intrisic to the ODT; in our current regime this occurs for a transport time of about 6 seconds. In general it is better to reduce the motion-induced losses than increase the lifetime, because operating the apparatus with a long transport time will also increase the time required per EDM mesurement. Therefore, once the lifetime of the "bus" ODT was improved to be above about 10 seconds no further upgrades to the lifetime were implemented. It should be noted, however, that the lifetime of the bus ODT can temporarily be significantly worse if the vacuum pressure increases (this can happen, for example, when a brand-new oven is loaded into the system).

4.6.4 Astigmatism

The transport simulation described above demonstrated the dependence of the transport efficiency on the longitudinal trap frequency. It is possible to increase the longitudinal trap frequency by increasing the transverse trap frequency, namely by reducing the transverse beam waist. In the case of a Gaussian beam this is straightforward. However, with an astigmatic and aberrated beam this approach is limited for 2 primary reasons; first, because the positions of the x and y foci will change as the alignment progresses, and also because, unless the aberrations are well-known, the relation between the transverse and longitudinal waists is unclear. Therefore, to optimize the alignment and reduce the longitudinal waist we purchased a ThorLabs M^2 Measurement System. This device allows the user to measure 2 orthogonal slices of the ODT beam over 20 cm, providing almost a full 3D intensity profile. As shown in Figure 4.24, with this device, it is straightforward to measure the astigmatism of the beam, and adjust lenses to correct for it.

After improvements to the traveling-wave ODT optics and the pressure in our vacuum chambers, we were able to reach a single-trip, 1 meter transport efficiency of about 10%. By reducing the astigmatism in our ODT beam by a factor of 5 using this more

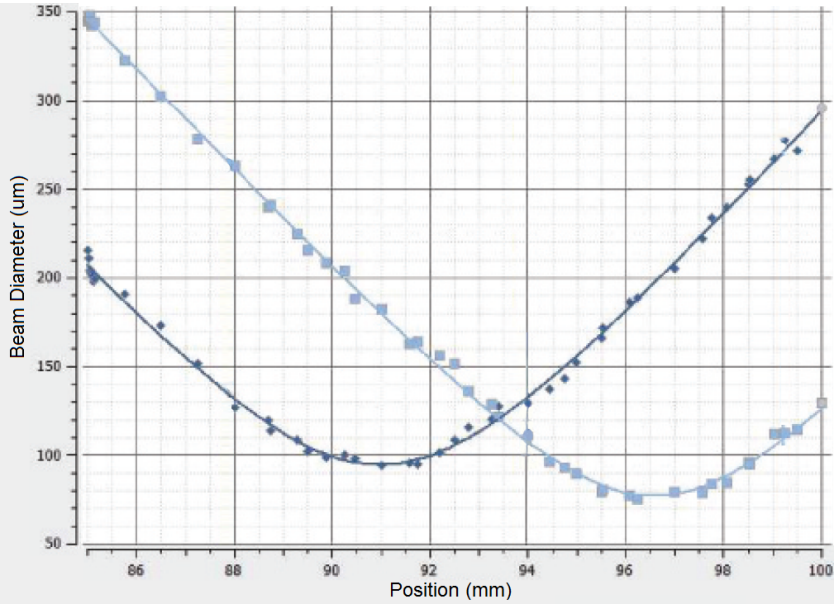

FIGURE 4.24: Measurement of the astigmatism of the bus ODT before final tuning. The two curves are orthogonal scans of the beam, each as a function of axial position. The displacement of the two foci is measured to be 5.6mm. Careful alignment of the lenses in the system reduced the astigmatism to 0.9mm.

rigorous alignment, the typical 1-meter transport efficiency achieved with the apparatus was about 30%.

4.7 ODT-to-ODT Transfer

The final step of the laser cooling and trapping is to load the atoms into a standing-wave ODT, formed by a 1550 nm, 10W, single-mode, single-frequency, retroreflected laser. The beam is focused to a $1/e$ waist diameter of 120 μm, comparable to the traveling-wave ODT. It is in this ODT that the actual EDM measurement is done. As this ODT does not move (intentionally), it is referred to as the holding ODT. The low atom density in this experiment presents an unsual problem that makes this challenging, in that the atoms will not interact with each other and therefore will not rethermalize as the potential is changed. To illustrate the challenge, this section will first include a discussion of some of the ideas proposed to accomplish ODT-to-ODT transfer, then the discussion to move to the successful implementation currently in use.

4.7.1 Rate Equation Model

As ODTs are conservative potentials, once the traveling-wave and standing-wave ODTs are overlapped we must apply some dissipative, velocity-dependent force to transfer the atoms between the two traps. Every approach described below (both successful and not) involves the application of 714 nm light. Successfully loading atoms from one ODT to another requires loading the atoms in faster than they are lost. There are many potential loss mechanisms, including heating and radiation pressure force, but one loss mechanism that does not depend on geometry is the optical pumping of atoms into long-lived metastable states. Every relevant electronic state in radium is expected to be trapped in the ODT except $^1P_1$, so the atoms will not truly be "lost"; however, they will be removed from the cooling cycle, and therefore effectively unavailable for loading into the holding ODT. A rate equation model was written using theoretical branching ratios and decay rates from Ref. [46]; the code is given in Appendix C. Results for a characteristic 714 nm intensity (the intensity used in the 3D MOT during the cooling phase) are shown in Figure 4.25; the population in the ground state is significantly depleted after about 100 ms. The depletion rate will depend on the experimental details, and particularly the intensity needed; however, this provides a characteristic timescale. This means that the time required to load atoms between the two traps should not be much longer than 100 ms.

4.7.2 Failed Ideas

Optical Molasses: The simplest idea is an optical molasses, formed by 2 counter-propagating red-detuned 714 nm beams. This will result in cooling the atoms, however it will also result in transverse heating and losses by pumping the atoms to metastable states. With a dissipative force only in the longitudinal axis, this approach will be successful if the rate at which atoms are loaded into the trap is fast compared to the loss rate. Further, as the longitudinal trapping force of the bus ODT is low (the trap frequency is only 3-5 Hz) any imbalance in power between the two retroreflected 714 nm beams will result in a radiation pressure force; the atoms will be pushed out of the trap if the imbalance is greater than 1%, which is very challenging to achieve in practice. Monte Carlo simulation predicts the time required to load atoms into the holding ODT

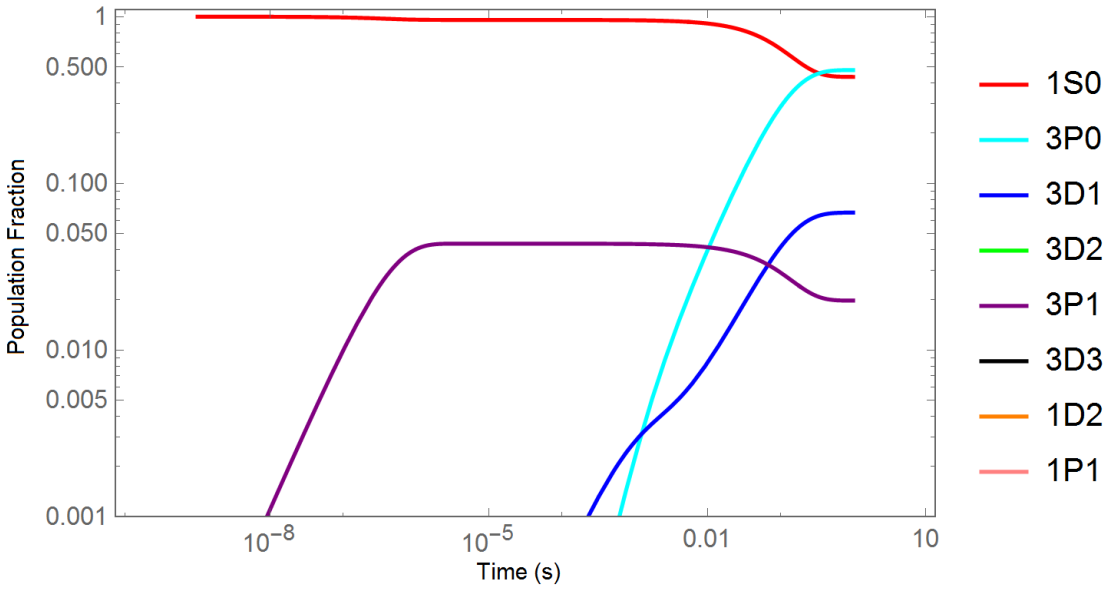

FIGURE 4.25: Rate equation model of radium atoms, under illumination with 714nm light with S=.05. Blackbody repumping and ODT repumping are turned on for this calculation.

to be about 1 second, whereas the rate equation model above predicts a significant fraction of atoms are pumped to metastable after about 100 ms. Empirically, it is possible to load atoms from the bus ODT to the holding ODT using this method; however, the maximum achieved efficiency was only about 5%.

Pulse Trick: One of the main limitations of the above approach is that the optical molasses cools the atoms down but doesn't "push" them to the center; in fact, it suppresses motion. One way to solve this problem is to pulse the 714 nm light instead of keeping it on constantly. The trap frequency described above is the characteristic oscillation frequency of the atoms in the trap (in the limit where the trap is harmonic). A pulse of light will form the optical molasses and cool the atoms, but leave their position in the trap unchanged; once the pulse is turned off, the atoms will fall to the center, all at this same frequency. A second pulse of light, if applied sooner than one full period, will again "freeze" the atoms in place, but the position distribution will be smaller. Therefore, by applying pulses of light at one quarter of a full oscillation period it is theoretically possible to quickly condense the atoms into the center of the trap, avoiding one of the main limitations of a simple optical molasses. Unfortunately, this requires the ODT to be well-described by a harmonic potential, which is not true in general for a beam affected by astigmatism and spherical abberation. No compression of the atom

cloud was observed using this approach.

Focus Trick: As briefly mentioned above, an intensity imbalance in the retroreflected 714 nm beams will produce a radiation pressure force. This force is position-independent for collimated beams, but can be position-dependent for focused beams. By placing the focus of the 1st pass 714 nm beam on one side of the bus ODT, and the focus of the 2nd pass 714 nm beam on the other side of the bus ODT, we create a position-dependent force that pushes the atoms to the center of the bus ODT. In this configuration the intensity imbalance in most positions will be large, so the atoms can be accelerated much faster than in an optical molasses. However, the success of this technique relies on being able to put the position of intensity balance at the center of the ODT, which requires very precise alignment (with 6 degrees of freedom, 3 for each beam). No compression of the atom cloud was observed using this approach.

1064 nm ODT: One of the problems that limits the ideas described above is that even after an atom is successfully loaded into the standing-wave ODT, it will continue to scatter 714 nm light, and can therefore be heated out of the trap. One approach to avoid this problem is to use a non-magic wavelength for the standing-wave ODT. In this case, the ground-state and excited-state polarizabilities are different. Therefore, if the 714nm laser is tuned to excite atoms only in the 1550nm ODT, the trapped atoms will not experience significant scattering from the 714 nm light. 1064 nm was chosen because of the availability of high-power lasers at that wavelength, and because it is expected that differential polarizability will cause the resonance to shift by more than the linewidth of the 714 nm transition for reasonable 1064 nm intensities [47]. We were able to employ a 20 W 1064 nm beam, with a 100 μm diameter waist, in both single-pass and in a crossed geometry shown in Figure 4.26. Using this trap wavelength in single-pass and forming an optical molasses as described above, we were unable to observe any transfer of atoms between the two ODTs. Using the crossed geometry we were able to achieve a transfer efficiency of about 5%; i.e. no better than using a 1550 nm standing-wave.

4.7.3 1D MOT

From the previous section it is clear that it is not trivial to transfer atoms between the ODTs efficiently. The fundamental problem is that the rate at which atoms must be loaded into the holding ODT must be no slower than about a few hundred ms, while

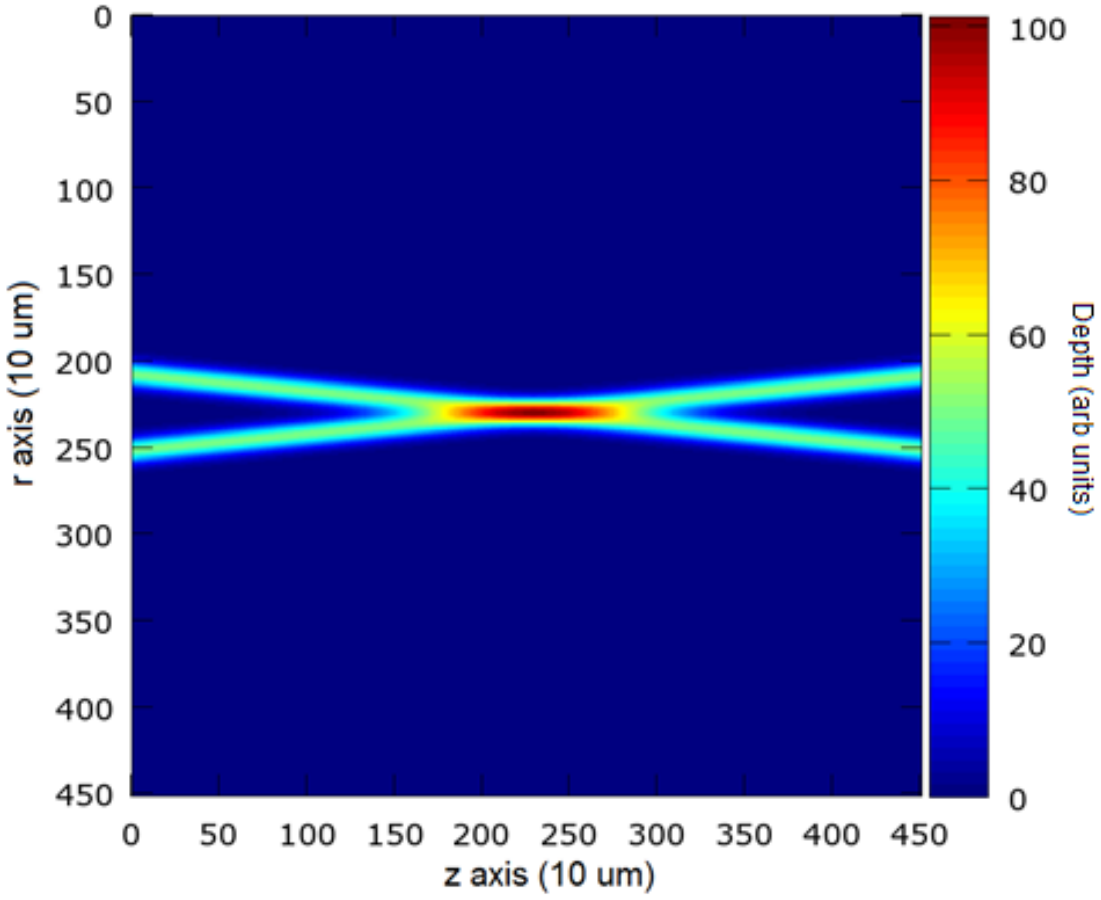

FIGURE 4.26: The geometry used to successfully demonstrate ODT-to-ODT transfer with 1064 nm ODTs. Only the 1064 nm beams are shown; when aligned, the bus ODT would be vertical in this image.

simultaneously being experimentally robust enough to not require unfeasibly precise alignment. Creating an optical molasses and then overlapping a quadrupole magnetic field solves these problems, by creating a 1D MOT. The position and compression of the 1D MOT can be easily tuned by adjusting the laser power balance and frequency 4.27. The dynamics of the 1D MOT are described in more detail in Ref. [48], but in general the parameters are similar to those used in the cool MOT.

There are concerns that the use of a quadrupole magnetic field inside the mu-metal shields would lead to magnetization–and in that case, could potentially result in an EDM systematic (or at the very least, could vary the magnetic field environment enough the limit statistics). The 1D MOT is briefly pulsed on when it is time to transfer atoms between the two ODTs, but is turned off with a mechanical relay to prevent current flow at all other times. The magnetization due to the 1D MOT has been measured to

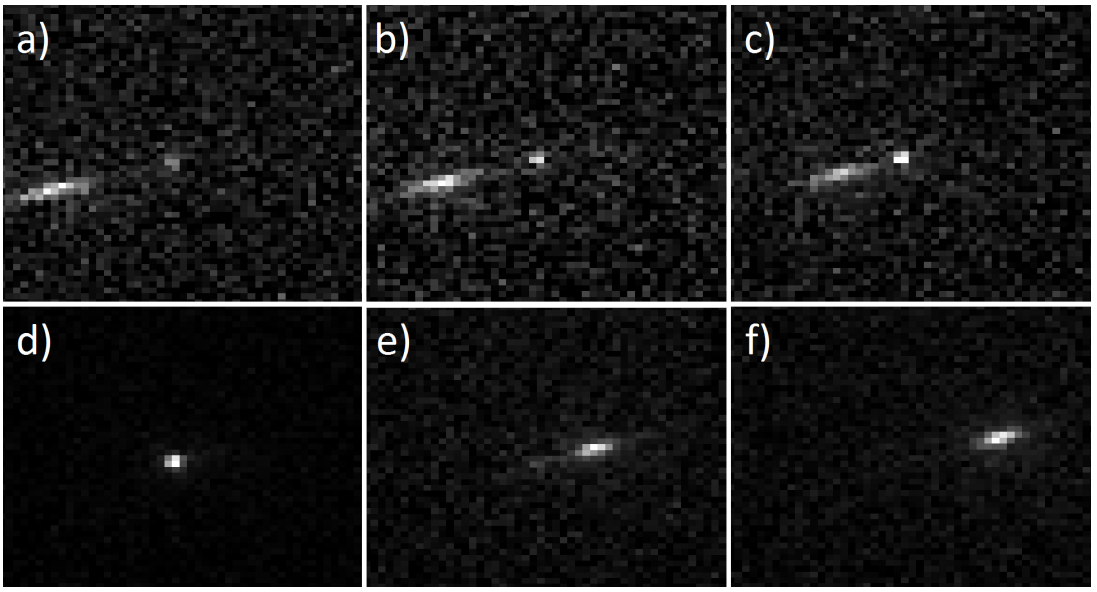

FIGURE 4.27: Adjusting the position of the 1D MOT relative to the overlap of the two ODT's by changing the balance of the 1D MOT beams. From a) to f) the 1D MOT is swept through the overlap of the two ODT's. Each image is a single shot of atoms. Fluorescence generally occurs most strongly in the center of the 1D MOT (the ellipse) and the deep potential well (the dot) created by the two ODTs. All three are aligned in d); this is the position for optimum transfer efficiency. Each image is 2 mm wide.

be less than 300 nG (i.e. below the measurement sensitivity), and thus does not present a problem at the current level of sensitivity); the ramp shape and time constant have been chosen to minimize the magnetization. If in the future the magnetization becomes a serious problem, an AC 1D MOT can be used instead, in which the magnetic field and polarization of the laser beams are synchronously alternated to maintain a constant trapping force.

Using this 1D MOT technique it is possible to transfer as much as 70% of the atoms to the standing-wave ODT [48], and this is the technique used for the EDM measurements described below. Transfer typically requires application of 714 nm light for 200 ms, comparable to the time required during the Cool phase of the 3D MOT. Due to the narrow 714 nm transition, frequency stability is crucial for robust transfer; the sensitivity to 1D MOT frequency is shown in Figure 4.28.

4.7.4 Beam Position Monitor and Feedback

An important realization while attempting ODT-to-ODT transfer was that mechanic instability can dominate, preventing successful alignment and minimizing average transfer

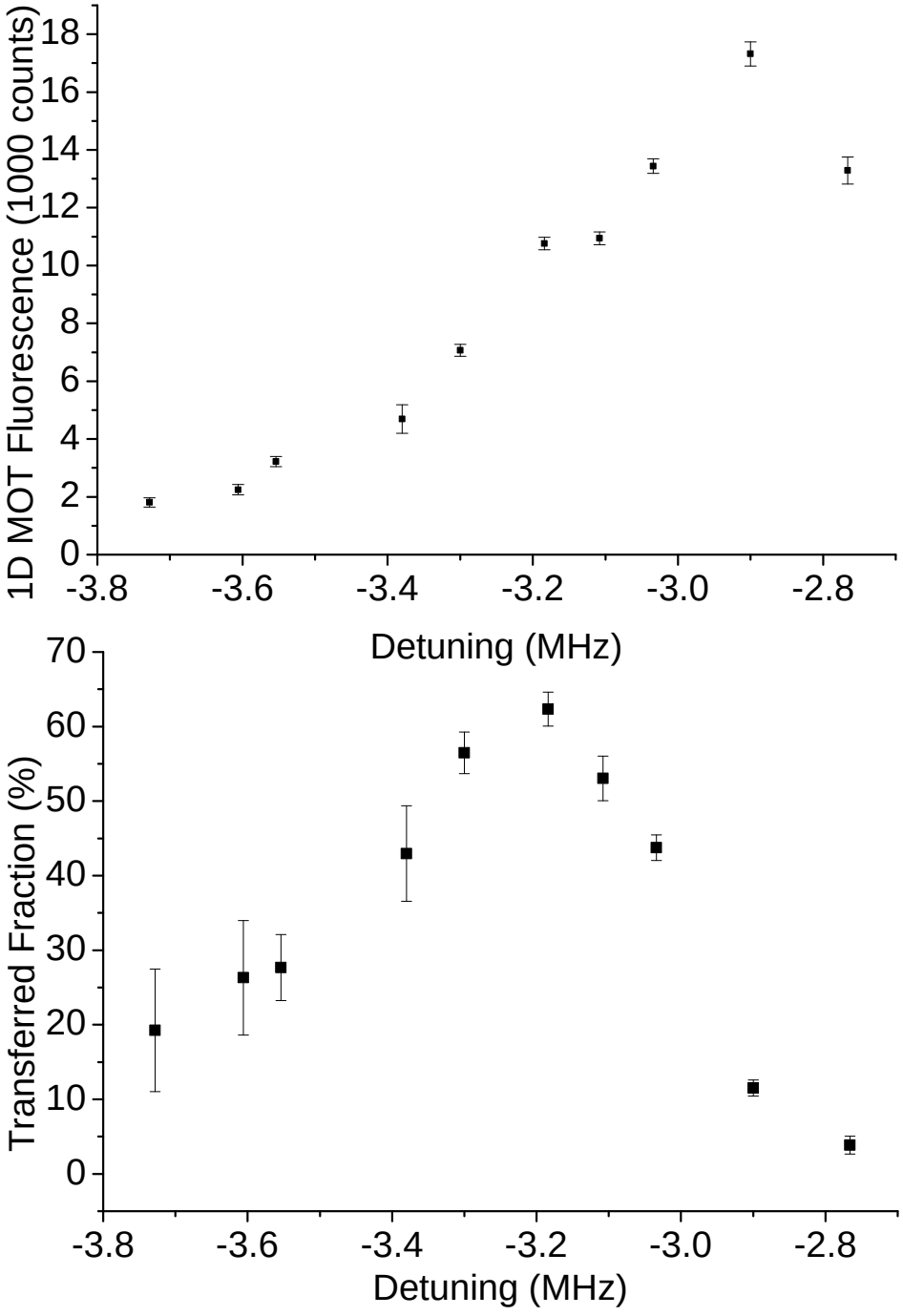

FIGURE 4.28: ODT-to-ODT transfer efficiency as a function of frequency. The top plot shows the brightness of the atom cloud (without actually turning off the traveling-wave ODT); the lower plot shows the fraction of atoms that remain after the traveling-wave ODT is turned off. Note that, just as with a 3D MOT, there is a tradeoff between brightness and ensemble temperature. This data was taken in a test chamber in which a large bias field was applied transverse to the longitudinal axis of the traveling-wave ODT; this bias field produced a large offset in the resonant frequency. Remaining in the regime of optimum transfer requires frequency stability on the level of 100 kHz.

efficiency. This is relatively straightforward to understand; the bus ODT is formed by a 2 m focal length lens, and the overlap between the two ODTs has to be better than 100 μm in the vertical dimension. The holding ODT is formed on two separate tables, one for the 1st pass and one for the retroreflection; therefore there are three separate tables (two of which are not stabilized with sand, and none of which are stabilized with air) which must remain stable relative to each other within 100 μm. For optimum transfer efficiency, the overlap should really be stable to 10 μm.

To monitor the vertical position of the bus ODT an image of the bus ODT was formed by a lens outside the vacuum system; the object plane of this lens was set to be the location of the electrodes, and the image plane was set to be a ThorLabs beam profiler. This allowed one-to-one analysis of the vertical (and horizontal) position of the bus ODT. The data recording is complicated by the fact that the bus ODT, in real operation, is only both on and between the electrodes for a few seconds, so a Labview program was written to gate the data as needed to allow real-time analysis.

Ideally, the room could be made sufficiently stable that no feedback servo would be needed. A correlation between the room temperature and the vertical ODT position was found, and the room temperature was further stabilized with the addition of another AC unit. The air flow is adjusted to minimize the fluctuations of the room temperature (or equivalently, the bus ODT position). However, as the room temperature is partially dependent on the outside room temperature this system is not perfect; therefore, a piezo was mounted onto the vertical knob of one of the bus ODT mirrors before the beam enters the vacuum system. The Labview program can adjust this piezo to keep the bus ODT centered, to compensate for thermal drift. However, as the servo is only allowed to operate for a few seconds every 50 second measurement cycle, the servo is only able to compensate for long-term drifts, not drifts that occur faster than a measurement cycle. The layout of the beam position servo system is shown in Figure 4.29.

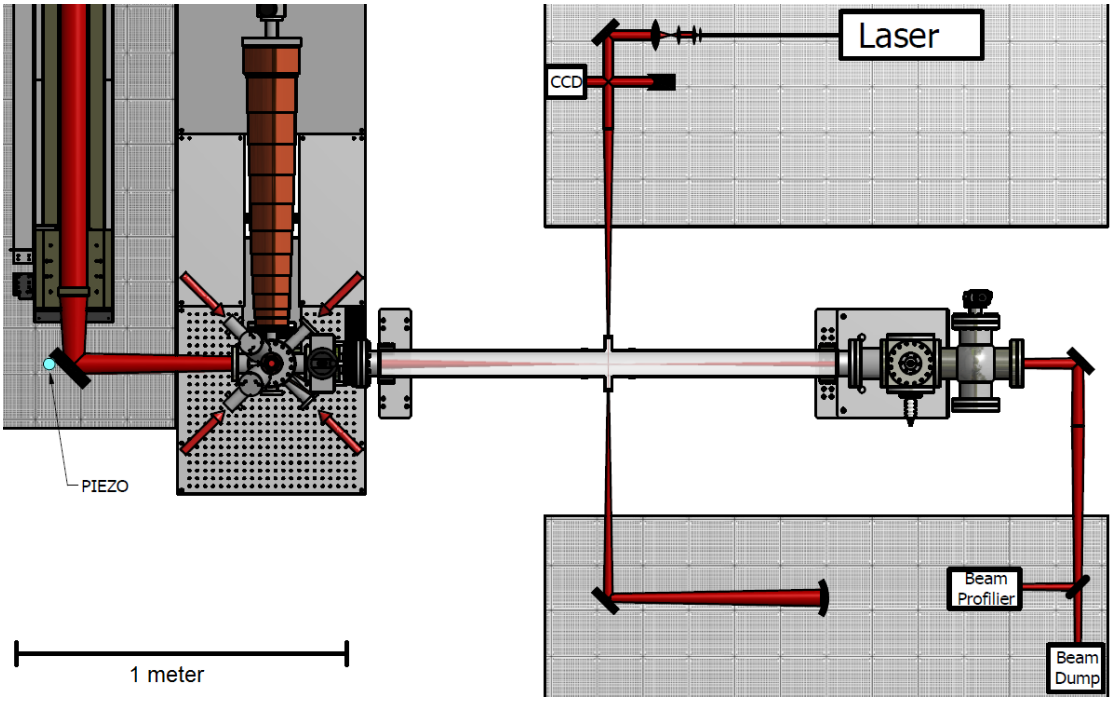

FIGURE 4.29: Set-up of the two ODT lasers, with the beam position servo.

Chapter 5

Discussion of Science Chamber

5.1 Vacuum System

The science chamber is a glass (pyrex) tube about 1 meter long. Glass was chosen to minimize ferromagnetism. The science chamber has three pumps: an ion pump, a titanium sublimation pump (part of the ion pump assembly), and a NEG pump. For the EDM data shown in this thesis the pressure in the glass tube was about 3×10^{-10} Torr; this was, however, due primarily to a leak in the vacuum system, and was an order of magnitude worse than the best achieved previously. At time of writing, the leak has been fixed and the pressure in the glass tube is below 3×10^{-11} Torr.

Performing a water bake of the glass tube after it has been exposed to atmosphere deserves special comment, as it is much more fragile than a typical stainless steel vacuum system. The glass-to-metal seal is likely the most fragile part; effort is made to guarantee that a temperature difference of no more than 20 ^{o}C exists over the entire length of the tube. To perform a water bake, a jig is installed that allows the entire tube to be wrapped in plastic (to maintain high air temperature) without any part resting directly on the glass tube). Typically the water bake is performed for 1-2 weeks with an average temperature of 130 ^{o}C.

5.2 HV Electrodes

For the EDM experiment we apply an electric field of approximately 67 kV/cm across a pair of copper electrodes, resulting minimal (<100 pA) leakage current and no HV discharges. We chose copper due to its low ferromagnetism, low outgassing, and the relative simplicity of manufacture. Schematics of the electrodes used can be found in Figure 5.1. A static discharge is particularly troubling, as material may be ablated from the high-field surface and impact the low-field surface, potentially causing permanent damage and necessitate opening the (very low pressure and slightly radioactive) vacuum system to fix. To achieve these requirements, the electrodes must first be machine-polished with a flatness tolerance of 5 millionths of an inch, then hand-polished with a Simichrome metal polish paste, then commercially electropolished. The final step was to condition the electrodes by gradually ramping up the potential in steps of 1000V (in vacuum) and waiting for the leakage current to fall to the acceptable level. Microdischarges occur at around 80 kV/cm, which is why 67 kV/cm was chosen. It should be noted that the actual voltage differences used, measured by a high voltage divider, were 15488 ± 9V in the "up" (parallel to the B-field) configuration and 15598 ± 1V in the "down" (anti-parallel to the B-field).

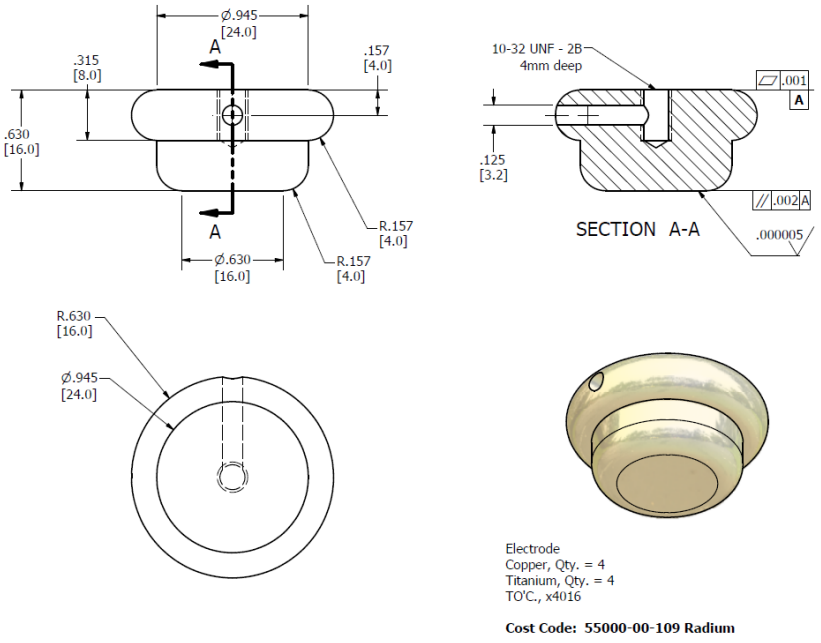

FIGURE 5.1: Diagram of the electrode geometry.

The ground state of radium will shift in the presence of an electric field due to the DC polarizability (predicted to be 3.21 $\times$ 10^{-23} cm^3 [35]; it has not yet been measured); the shift is calculated to be -150 MHz for 67 kV/cm. Therefore small gradients in the electric field can apply a force on the atoms, competing with the force from the ODT to displace the atoms. First, this force must be small enough that the atoms will remain trapped in the ODT; second, this force must be small enough that after displacement the atoms will not experience a significantly different magnetic field (determined by the B-field gradient). The electric field has an expected spatial variation below 1%/mm in the vertical axis, which produces a displacement of approximately 2 nm in the standing-wave ODT. The variation in magnetic field the atoms experience due to this displacement is negligible; see the systematics section for more details.

The voltage across the electrodes can be monitored two different ways. The voltage can be measured directly from the HV power supply, with an internal monitor, and can also be monitored at the output of an SF_6-insulated HV divider. In addition to these, the current out of the HV power supply and the leakage current between the electrodes is also monitored.

As a test to make sure the electric field is actually turned on, and at the right time, the effect of the electric field on the atoms can be easily observed. For ^{226}Ra at 67 kV/cm, the shift of the 483 nm transition is expected to be about 125 MHz for $m_J = 0$ and 60 MHz for $m_J = \pm 1$, i.e. several linewidths, but still reachable by adjusting an AOM. By contrast, the shift of the 714 nm transition is expected to be about 300 GHz for $m_J = 0$ and 275 GHz for $m_J = \pm 1$, i.e. far beyond the reach of a single AOM. This means that applying the electric field after the atoms have been transferred to the standing-wave ODT will cause the signal to decrease dramatically, but not completely; and the signal can be recovered by adjusting an AOM. If the electric field is applied during the 1D MOT, however, the transfer efficiency will be 0%. Further, if the electric field is applied before the atoms are transported between the electrodes the transport efficiency will be 0%, as the potential due to the electric field dwarfs that of the ODT (although the electric field potential is conservative, small gradients will quickly pull the atoms out of the ODT). Thus there are three signals we use to determine the timing and approximate strength of the electric field.

Another issue with the timing of the HV system concerns the timing required to ramp

up and down the electric field (measured to be the same). At the moment, there is no relay in place to quickly stop the flow of current, so the timescale is given by the capacitance of the cables that connect the HV control box to the electrode feedthroughs attached to the vacuum system. Previously, the HV power supply had been measured to ramp down with a 1/e time constant of 90 ms. However, in the two EDM runs the HV divider measured the 1/e ramp down time to be 160 ms. A possible reason for the slight discrepancy is the removal of current limiting resistors between the two measurements.

The gap between electrodes was measured using a camera mounted to a micrometer translation stage. By monitoring the location of a reference marker on the camera relative to the electrodes, the gap can be measured using the scale on the stage. The translation stage calibration was tested using a second high-resolution micrometer. The electrode gap was measured to be 2.276(22) mm; to be conservative it was reported as 2.3(1) mm.

5.3 Magnetic Fields

5.3.1 Magnetic Field Requirements

As the experiment is basically a sensitive measure of spin precession, any small fluctuations in magnetic field strength will limit its sensitivity. There are two related mechanisms that can cause problems. The first is a gradual drift in magnetic field (i.e. current) during the course of the run, generally no longer than a week. Whatever the resulting phase sensitivity of the experiment from a statistical point of view, the phase change over the week due to a drifting magnetic field should be much smaller. The second effect is shot-to-shot fluctuations within each measurement cycle, on the minute timescale. Even if the magnetic field has no overall drift, if the average magnetic field the atoms experience during precession varies greatly, it limits the statistical sensitivity of the experiment.

It should be noted that in the current phase of the experiment there is no direct measure of the magnetic field in the science chamber–the assumption is that the measurement of current in the bias field coil is sufficient. In the two runs presented in this thesis, two different current supplies were used. In the October 2014 run, a battery-operated current

supply was used, which was measured to have a deviation of 0.1 parts per thousand after 2000 seconds (see Figure 5.2). We believe this poor stability to be due to a depleted internal battery; the current supply was replaced with an ILX Lightwave Diode Laser current supply for the December 2014 run. This current supply was measured to have a deviation of 0.6 ppm after 2000 seconds (see Figure 5.3). To directly measure magnetic fields, the plan is to use Rb vapor cells operating as optical magnetometers. A pair of Rb vapor cells were built and successfully demonstrated sensitivity better than ppm, but were not employed in this version of the experiment. It is expected that in a later phase of the EDM project, they will be installed above and below the science chamber to monitor magnetic field fluctuations (with a bandwidth of 1 Hz). In a (much) later version of the experiment, Yb atoms can be co-trapped in the optical lattice and used as co-magnetometers, with high spatial resolution.

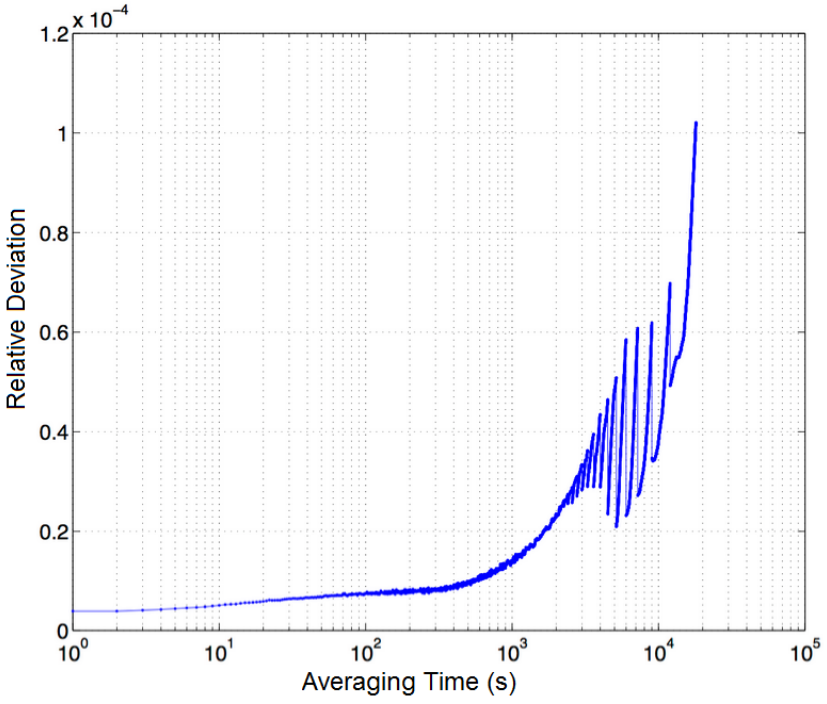

FIGURE 5.2: Allan deviation of the current of the Italian supply, used in the October EDM measurement.

Another issue is magnetic field gradients. The atoms must precess at approximately the same rate if we are to measure optimum contrast. This results in two separate requirements: first, the gradient should be small enouh to produce no significant decoherence in a single shot, and second, the gradient should be small enough to produce no significant systematic effect if the atoms move upon E-field reversal (see chapter on systematics for

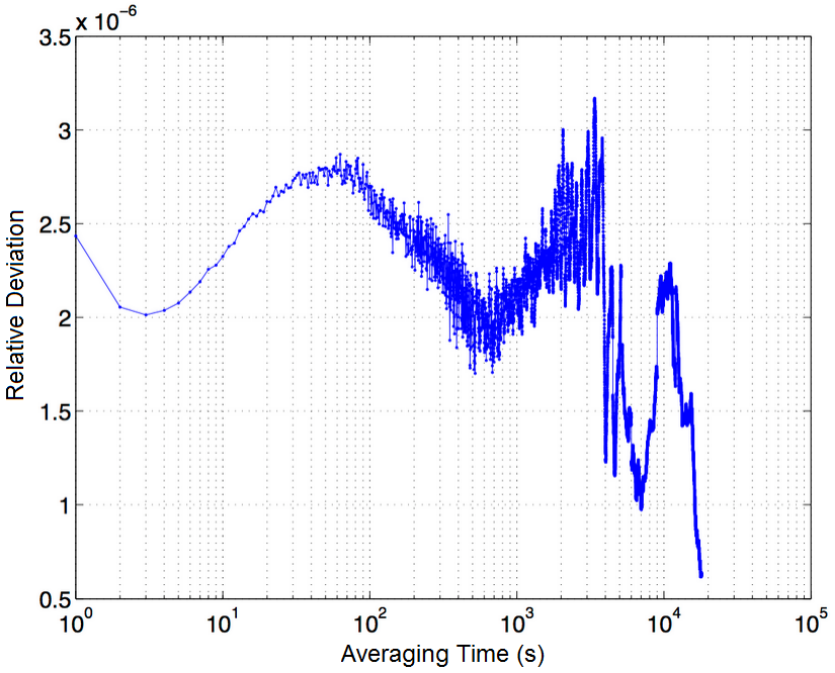

FIGURE 5.3: Allan deviation of the current of the Italian supply, used in the December EDM measurement.

more discussion on this issue). We are helped greatly by the small volume of the atom cloud, only about 50 μm in diameter. Requiring that we have no more than a 0.5 rad phase spread over a 10 second frequency measurement means we can have a magnetic field variation of no more than 7 μG over the atom cloud. The magnetic field gradients have been measured to be less than 0.1%/cm using Rb magnetometers at three positions within the cos(θ) coil (see next section). As the atom cloud is no bigger than 50 μm in diameter, this gradient results in a B-field difference at the top and bottom of the atom cloud of 0.2 μG, which is well within this tolerance. The systematic effect due to this has also been calculated to be negligible at the current statistical sensitivity (see systematics section).

5.3.2 Cosine Theta Coil

The bias magnetic field is created by a cos(θ) coil wound on an aluminum frame. The coil contains 60 loops of 28-gauge copper wire. The frame actually includes six coils (cos(θ), sin(θ), axial solenoid, and three sets of gradient coils), but only the cos(θ) coil was used in this experiment.

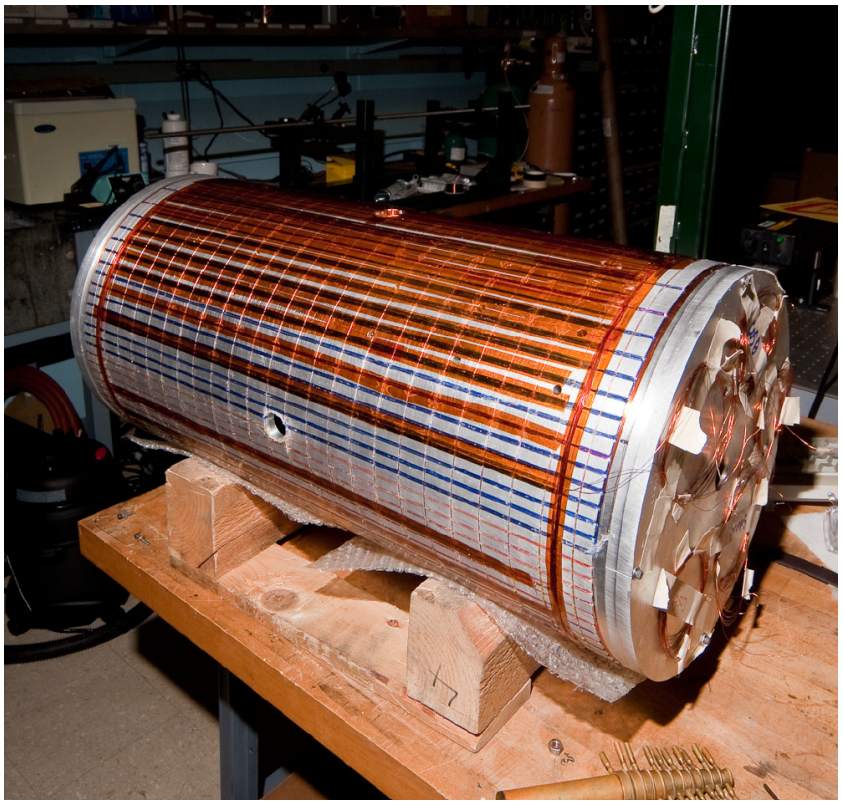

FIGURE 5.4: The $\cos(\theta)$ coil before being attached to the science chamber apparatus. The coil is wound on an aluminum cylinder 0.32 m in diameter and 0.65 m in length.

5.3.3 Magnetic Shielding

Magnetic shielding is needed for two primary reasons: the magnetic field must be stable so that contrast is not lost as we average over multiple runs, and any magnetic field due to the applied electric field must be negligible compared to the statistical sensitivity of the experiment. As the only real systematics that will affect this experiment are those which affect the spin precession linear in the applied electric field, the requirements for the mu-metal shielding are not very strict. Three layers of mu-metal shields surround the $\cos(\theta)$ coil frame. The shielding factor of the mu-metal was measured using a combination of fluxgate outside the shields and Rb magnetometers inside. Without degaussing, the shielding factor is characteristically about 8,000. Degaussing can improve the shielding factor by "resetting" the shields (the shields saturate above 1G, not dramatically bigger than Earth's field). To degauss, typically about 1 amp is sent through a set of coils wrapped around the mu-metal; a 50 Hz sinusoidal signal is used, with a exponential decay of 300 s. The most important thing here is that there be no residual offset current when the degaussing signal is finished; therefore an isolation transformer is put between

the current supply and the coil. After degaussing the shielding factor was measured to be about 20,000, more than sufficient for this phase of the experiment.

Chapter 6

Nuclear Spin Precession of ^{225}Ra

6.1 Larmor Precession

We begin with a brief review of Larmor precession, which is a concept fundamental to this experiment. It can be treated classically; consider a magnetic moment $\vec{\mu}$ in a magnetic field $\vec{B}$, along the z axis. The torque on the moment is

$$\vec{\tau} = \frac{\partial \vec{J}}{\partial t} = \vec{\mu} \times \vec{B} = B\gamma(\vec{J} \times \hat{z})$$

Where J is the angular momentum and $\mu = \gamma J$. With $J_x(t = 0) = x_0$ and $J_y(t = 0) = 0$ we get

$$J_x = x_0 \cos \omega t$$

$$J_y = -x_0 \sin \omega t$$

Therefore atoms initially polarized in the plane perpenicular to z will precess at a frequency $\omega = \gamma B$.

6.2 Optical Pumping and Imaging

We begin by considering two separate kinds of detection pulses; pulses sensitive only to atom number and pulses sensitive specifically to the population of atoms in one (and only one) of the two magnetic sublevels in the ground state. The number of atoms in the standing-wave ODT is probed by a blue laser beam tuned to the resonance of $7s^2\ {}^1S_0$ $F = 1/2 \rightarrow 7s7p\ {}^1P_1$ $F = 3/2$ at 483 nm, co-propagating along the standing-wave ODT laser beams. This transition can cycle for an average of about 1000 times before leaking to lower D states. The shadow image produced by resonant absorption is cast onto a CCD camera (Fig. 6.2). To produce an absorption image (given about 200 ^{225}Ra atoms in the trap), the blue beam is pulsed for 1.45 ms, during which each atom absorbs on average 100 photons. This detection method is destructive in that it heats the atoms out of the trap and pumps them to metastable levels. By measuring the number of atoms at various delay times, the lifetime of the atoms in the trap is determined to be 3-5 s, about 10 times shorter than that in the 3D MOT. This is consistent with the higher vacuum pressure observed in the glass chamber.

The atom spin polarization is both produced and detected via optical pumping by a circularly polarized blue beam tuned to the resonance of the non-cycling transition $7s^2\ {}^1S_0$ $F = 1/2 \rightarrow 7s7p\ {}^1P_1$ $F = 1/2$. An atom with a spin in the fully polarized state does not absorb photons, while one in the opposite-spin state absorbs on average three photons before becoming fully polarized. To see this, we begin by considering the quantum mechanical formulation of Larmor precession. First we introduce the three spin operators for a spin 1/2 system:

$$S_x = \begin{pmatrix} 0 & \hbar/2 \\ \hbar/2 & 0 \end{pmatrix} \quad S_y = \begin{pmatrix} 0 & -i\hbar/2 \\ i\hbar/2 & 0 \end{pmatrix} \quad S_z = \begin{pmatrix} \hbar/2 & 0 \\ 0 & -\hbar/2 \end{pmatrix} \tag{6.1}$$

The Hamiltonian for the magnetic moment described above, in a magnetic field along the z axis (which we take to be our quantization axis, is

$$H = \frac{\hbar\omega}{2} \begin{pmatrix} 1 & 0 \\ 0 & -1 \end{pmatrix} \tag{6.2}$$

We write $|+\rangle$ and $|-\rangle$ as the eigenstates of the Hamiltonian:

$$H|+\rangle = \omega S_z|+\rangle = \frac{\hbar\omega}{2}|+\rangle = E_+|+\rangle, \quad H|-\rangle = \omega S_z|-\rangle = -\frac{\hbar\omega}{2}|-\rangle = E_-|-\rangle \quad (6.3)$$

We now consider a general initial state, with spin up in an arbitrary direction given by a polar angle θ and azimuthal angle ϕ:

$$|\Psi(t=0)\rangle = \cos(\theta/2)|+\rangle + e^{i\phi}\sin(\theta/2)|-\rangle = \begin{pmatrix} \cos(\theta/2) \\ e^{i\phi}\sin(\theta/2) \end{pmatrix} \quad (6.4)$$

The time evolution of this state is given by

$$|\Psi(t)\rangle = \begin{pmatrix} e^{-i\omega t/2}\cos(\theta/2) \\ e^{i\omega t/2}e^{i\phi}\sin(\theta/2) \end{pmatrix} \quad (6.5)$$

We now consider the probability of measuring spin up along the x-axis, with $|\pm\rangle_x = \frac{1}{\sqrt{2}}[|+\rangle \pm |-\rangle]$ and $|\pm\rangle_y = \frac{1}{\sqrt{2}}[|+\rangle \pm i|-\rangle]$

$$P_x = |_x\langle +|\Psi(t)\rangle|^2 = |\frac{1}{\sqrt{(2)}}\begin{pmatrix} 1 & 1 \end{pmatrix}\begin{pmatrix} e^{-i\omega t/2}\cos(\theta/2) \\ e^{i\omega t/2}e^{i\phi}\sin(\theta/2) \end{pmatrix}|^2 = \frac{1}{2}[1+\sin(\theta)\cos(\phi+\omega t)] \quad (6.6)$$

For atoms initially perpendicular to the magnetic field, setting the azimuthal angle to zero by symmetry, this simplifies to

$$P_x = \frac{1}{2}[1+\cos(\omega t)] \quad (6.7)$$

We see from this that the number of scattered photons can directly give us the precession angle. The probability of scattering photons is unfortunately not independent of time, due to the probability of pumping atoms to dark states. This is particularly problematic for the spin-sensitive detection on the F = 1/2 → F = 1/2 transition, because for every photon scatter there is a 1/3 chance of being pumped to the dark magnetic sublevel. For simplicity, we divide the process into equal "timesteps", during which an atom can scatter either 1 or 0 photons (1 photon if it's in the bright sublevel, 0 if it's in the dark

sublevel). The number of atoms available to scatter in a given timestep will be 2/3 of the number that were available in the previous timestep. As a function of "timesteps" N, the number of photons scattered per atom n is given by:

$$n = \sum_{m=0}^{N} (2/3)^m \tag{6.8}$$

This sum converges to 3 if we take N to infinity, meaning that if we allow an infinite number of scattering timesteps (*i.e.* send in an infinite number of photons), the maximum number of photon scatters we can get from an atom is on average 3. Rewriting this sum as an integral and normalizing so that the integral is 3 gives

$$n = \int_{m=0}^{N} 3 \cdot \log(3/2) \cdot (2/3)^m dm \tag{6.9}$$

However, to maximize our SNR we wish to expose for a time less than infinity. To determine the optimum number of scattering timesteps (which will tell us the optimum duration of our blue light), we include a term that includes the noise due to the BG photon shot noise.

$$SNR \propto \frac{1}{\sqrt{N}} \int_{m=0}^{N} 3 \cdot \log(3/2) \cdot (2/3)^m dm$$

This SNR is plotted in Figure 6.1. Not surprisingly, the optimum number of scattering timesteps is 3, which results in an estimated 2.1 scattered photons per atom on average. Note that the same treatment holds for both polarization and detection. In practice, we prefer to set the duration of the probe pulse slightly longer than the theory suggests, as the sensitivity to duration is much weaker for longer durations than shorter durations.

Compared to the atom-number measurement on a cycling transition, the spin-sensitive detection scatters 30 times fewer photons, resulting in a reduction of image contrast. This is because, in addition to the above effects, we cannot expose the number-detection imaging pulse for the full duration to pump all atoms to dark states–the camera will saturate first.

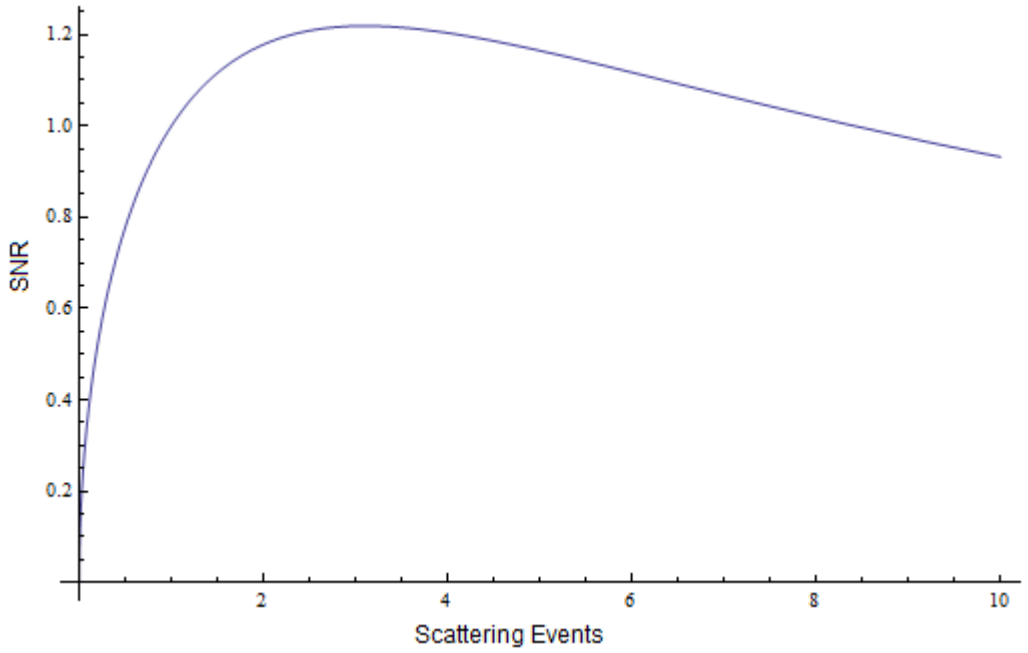

FIGURE 6.1: Sensitivity of SNR to number of scattering events (equivalently, the duration or intensity of the probe beam).

The key to efficient optical pumping for this system is a high degree of circular polarization with the (blue) pump beam. Following the treatment given in [49], we consider the electric field for arbitrarily polarized light, written in the $|R\rangle$ and $|L\rangle$ basis repesenting two orthogonal circular polarization axes

$$|E\rangle = E_0 e^{i\phi}[\sqrt{1+P}\frac{e^{-i\theta}}{\sqrt{2}}|R\rangle + \sqrt{1-P}\frac{e^{i\theta}}{\sqrt{2}}|L\rangle] \tag{6.10}$$

Equivalently it can be written in the $|S\rangle$ and $|P\rangle$ basis repesenting two orthogonal linear polarization axes

$$|E\rangle = E_0 e^{i\phi}[(\sqrt{1-P}\frac{e^{i\theta}}{2} + \sqrt{1+P}\frac{e^{-i\theta}}{2})|P\rangle + (\sqrt{1-P}\frac{e^{i\theta}}{2i} - \sqrt{1+P}\frac{e^{-i\theta}}{2i})|S\rangle] \tag{6.11}$$

The magnitude of the electric field is given by

$$\sqrt{\langle E|E\rangle} = \sqrt{(\frac{1+P}{2})E_0^2 + (\frac{1-P}{2})E_0^2} = E_0 \tag{6.12}$$

The degree of circular polarization is given by

$$\frac{\langle E_R|E_R\rangle - \langle E_L|E_L\rangle}{\langle E|E\rangle} = \frac{(\frac{1+P}{2})E_0^2 - (\frac{1-P}{2})E_0^2}{E_0^2} = P \tag{6.13}$$

We now consider the intensity of s-polarized light transmitted through a polarizing beam splitter at an angle θ with respect to the beam splitter axis, assuming perfect transmission and an extinction ratio of 0:

$$I = \langle E_S|E_S\rangle = E_0^2(\frac{1-P+1+P-2\sqrt{1-P^2}\cos 2\theta}{4}) = \frac{E_0^2}{2}[1-\sqrt{1-P^2}\cos 2\theta] \tag{6.14}$$

The maximum and minimum intensities are:

$$I_{max} = \frac{E_0^2}{2}(1-\sqrt{1-P^2}) \quad , \quad I_{min} = \frac{E_0^2}{2}(1+\sqrt{1-P^2}) \tag{6.15}$$

Therefore we can write the polarization P as:

$$P = \sqrt{1-A^2}$$

where $A = (I_{max} - I_{min})/(I_{max} + I_{min})$.

Here I_{max} and I_{min} refer to the maximum and minimum intensity of the pump beam after it has been sent through a polarizing beam splitter. A half-wave plate is put into the pump beam before the splitter and is rotated a full 360 degrees, and the beam after the splitter is sent onto a photodetector–Imax and Imin are given by the maximum and minimum signal on the photodetector. For perfectly circularly polarized pump light, the rotation of the half-wave plate will have no effect, so Imax and Imin will be the same, so A=0 and P=1. For perfectly linearly polarized light, the contrast of the signal will be perfect, so A=1 and P=0. In reality the pump beam will always be elliptical; it can be made more circular by adjusting a pair of waveplates (one half-wave and one quarter-wave) before the beam enters the Science Chamber. It is worth noting that in practice the polarizing beam splitter is placed outside the Science Chamber, after the beam has travelled through the Science Chamber, which means that this method can't

isolate any ellipticity induced by the birefringence of the glass viewports. In the end, the contrast of the precession signal is the best metric.

6.3 Background Subtraction Algorithm

A linear combination of images without atoms is used for background subtraction; *i.e.*, to suppress distortions arising from interference effects, following the technique used in Ref. [50]. The algorithm attempts to find the best background Q for an image with atoms A, using reference images R. We write Q as a linear combination of the reference images, $Q = \sum_k c_k R_k$, where k refers to different images. We miminize the least-squares difference $\delta = \sum_x m_x (A_x - Q_x)^2$ (where x refers to each pixel), where m is a mask placed over the atoms (determined by ^{226}Ra mesurements) to prevent the algorithm from suppressing the atom signal. Setting the derivatives with respect to each c_k equal to zero gives:

$$\frac{\partial \delta}{\partial c_j} = 2 \sum_x m_x R_{x,j} (A_x - \sum_k c_k R_{x,k}) = 0 \tag{6.16}$$

The right hand side results in a system of linear equations which can be solved by Matlab using LU decomposition. The noise of this detection scheme is approximately 1.2 times the photon number shot noise. This is implemented twice in our experiment; once in Labview to allow for real-time background subtraction, and once in Matlab to allow for post-processing of the images. Examples of the post-processing algorithm at work are given in Figure 6.2, panel b), and Figure 6.3, panels a) and b).

6.4 General Timing Sequence and Software

This section will discuss the general timing sequence used in the measurement of spin precession. The specific timing sequence used in the EDM measurement, as well as the actual spin precession data using absorption imaging, will be covered in the next chapter.

The timing sequence used to load atoms into the bus ODT and transport them to the science chamber is described in Chapter 4 (Sections 4.5.2 and 4.6.2). Transfer between

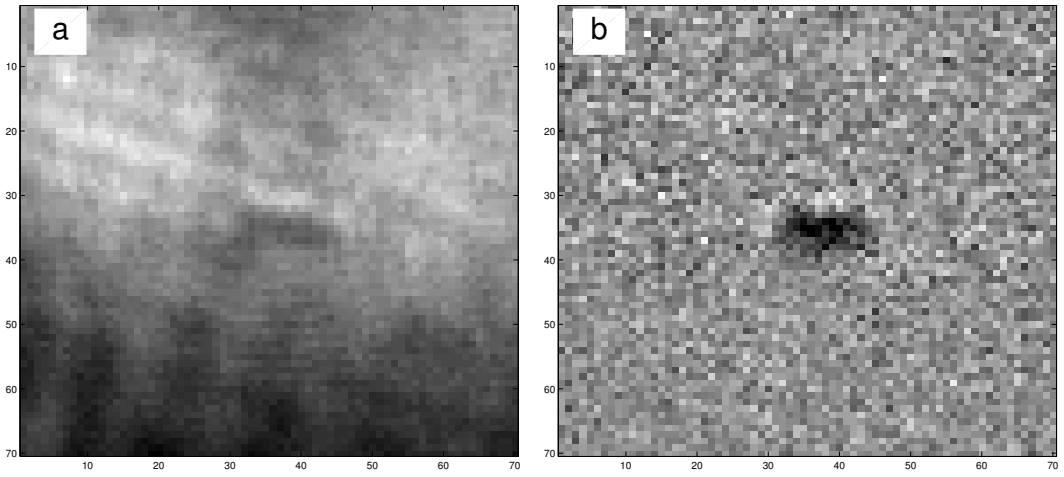

FIGURE 6.2: Examples of the background subtraction algorithm. Panel a) is an image of 5000 ^{226}Ra atoms without background subtraction; panel b) is the same image after backgroun subtraction. Note the presence of fringes in panel a).

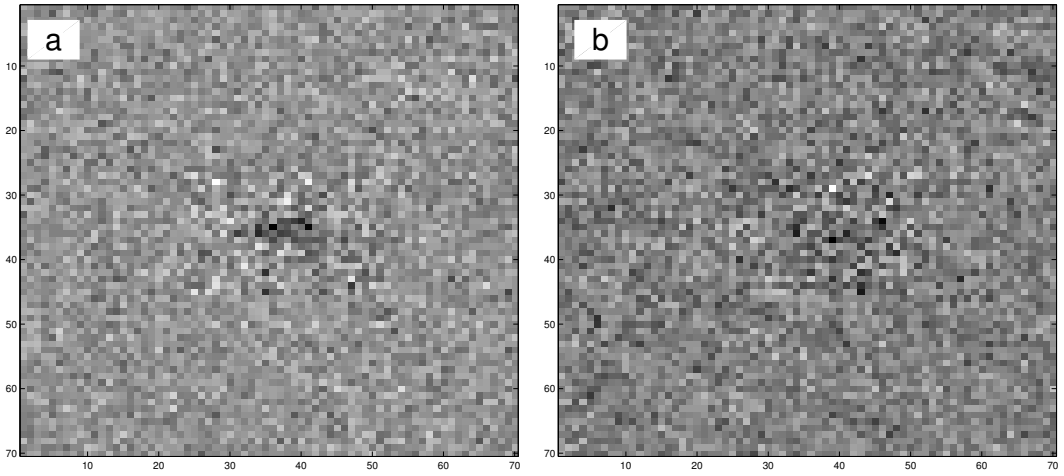

FIGURE 6.3: Panel a) is an absorption image of ^{225}Ra on the cycling transition, applying pulses almost at the saturation of the camera. Panel b) is an image of a similar number of ^{225}Ra atoms, using the spin-sensitive transition.

the two ODTs typically requires 200 ms of 714 nm light; the transfer is complete and the bus ODT is mechanically shuttered at 7.014 s into the measurement cycle. Five background blue images are taken before the atoms arrive between the electrodes, then one image is taken with the atoms unpolarized–this should give a signal at half contrast. Then the atoms are polarized and allowed to precess; this process is repeated until the experimenters expect there will be no atoms remaining. The polarization pulses are not recorded by the camera, as the SNR is expected to be too poor due to the long pulse duration. The process of polarizing and detecting is limited currently to a minimum of 400 ms, due to the retrigger rate of the camera (an Andor Clara). At this point, the holding ODT is shuttered for 1 second, long enough for all the trapped atoms to fall

away, and another 20 background images are taken. One final image is taken using the polarization pulse duration–this will be the only image near the camera saturation, and therefore is used as a "tag" to mark the end of each measurement cycle (the tag is used in post processing to determine if any camera triggers were skipped, or if the camera triggered at a wrong time).

A set of four VIs control the pulses. Three are VIs that program National Instruments multi-shot counters; one VI is used to control the Clara camera, one for the blue AOM, and one for the mechanical shutter on the blue imaging beam. A fourth VI converts the pulse sequence the user wants into a set of arrays giving the pulse times and durations. These arrays are then read by the VIs controlling the counters.

Decoherence during the spin precession is a serious potential problem; therefore the blue beam is mechanically shuttered nearly all the time. The shutter is briefly opened to allow a polarization pulse, then is closed until the imaging pulse is needed. The delay between the trigger on the shutter counter and the time when the relay actually receives the trigger, as well as the time required for the shutter to transition from fully open to fully closed, was measured and programed into the Labview VI. In addition, an extra user-controllable "buffer" was added to make sure the shutter could not accidentally block the blue beam at the wrong time. To further suppress any unwanted scattering of blue light, a pinhole was added after the blue AOM to block zeroth-order light. The extinction ratio of this system exceeds 50,000.

6.5 First Observation of Nuclear Spin Precession of ^{225}Ra

From the previous sections it is clear that, with only about 100 atoms in the standing-wave trap, the expected signal size is quite low. To see the first evidence of spin precession, we chose to use fluorescence imaging with a high solid angle imaging lens and a PMT, rather than absorption and a camera, as this was expected to have significantly higher signal-to-noise. This experiment was performed in a test chamber without electrodes, allowing a large lens to be placed inside the vacuum system, directly above the atom cloud. The use of a PMT allows us to crop out background counts occuring at the wrong times, and the PMT has a much faster "retrigger" rate tham the camera, allowing us to take more data points each experimental cycle. As this is not an EDM

experiment, there is no benefit to letting the atoms precess for a long time in the dark, so we measure the first several oscillations. As the test chamber was not shielded from magnetic fields, we apply a 7 G field to suppress the effect of Earth's field and provide a well-defined quantization axis; this also increases our precession frequency, effectively allowing us to take data more rapidly. The first demonstration of nuclear spin precession of ^{225}Ra is shown in Figure 6.4. The fit (similar to the one described in detail in Chapter 7) has a reduced chi square of 19.0/15, and gives an atom polarization of 96(10)%. Unfortunately our knowledge of the magnetic field the atoms experience is too poor to provide a useful measurement on the ^{225}Ra magnetic moment with this data; nonetheless, it demonstrated that we can polarize the atoms and observe their precession, an important first step.

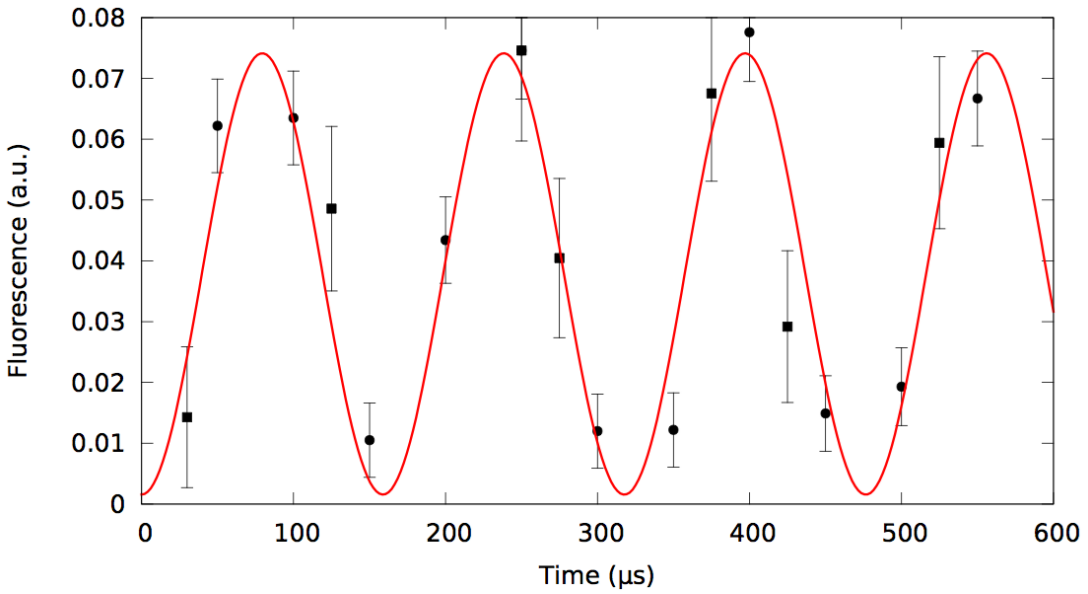

FIGURE 6.4: Spin precession of ^{225}Ra using fluorescence imaging.

Chapter 7

EDM Measurement of ^{225}Ra

7.1 Timing Sequence

The pulse sequence for the 483 nm light used for the EDM measurement is shown in Fig. 7.1. Two kinds of pulses, generated by acousto-optical modulator (AOM) switches, are used: 1.5 ms pulses to polarize the atom cloud, and 60 μs pulses to measure the number of atoms in the opposite-spin state (short pulses optimize the image signal-to-noise ratio, whereas longer ones for optical pumping maximize atom polarization). After each pulse, the 483 nm laser is blocked within 1 ms by an additional mechanical shutter to prevent decoherence induced by light leaking through the AOM while the atoms precess. Four images of atoms are recorded in each measurement cycle. The first occurs prior to any polarization pulse and, thus, produces a signal at half of the maximum contrast. The second occurs one half-period after a polarization pulse, and has a signal at the maximum contrast. The third is taken about 2 s after polarization; it is during this time that the E-field is applied. Then, the atoms are repolarized, followed by the fourth image also occuring about 2 s after polarization, but this time with no applied E-field. The third and fourth images are normalized to the second one in order to reduce sensitivity to atom number fluctuations. The third image is used to build the "E-field on" spin precession curve, and the fourth builds the "E-field off" spin precession curve. The data indicate that the decreasing contrast is consistent with the lifetime of the atoms in the ODT. An example of such a data set is shown in Figure 7.2.

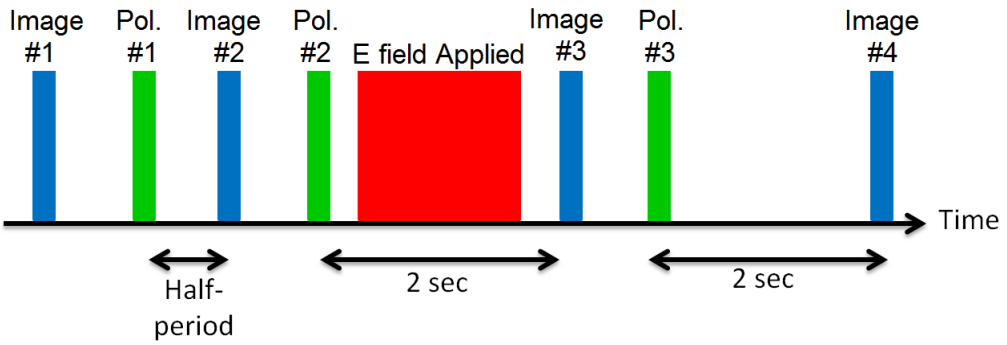

FIGURE 7.1: Pulse sequence used in the EDM measurement.

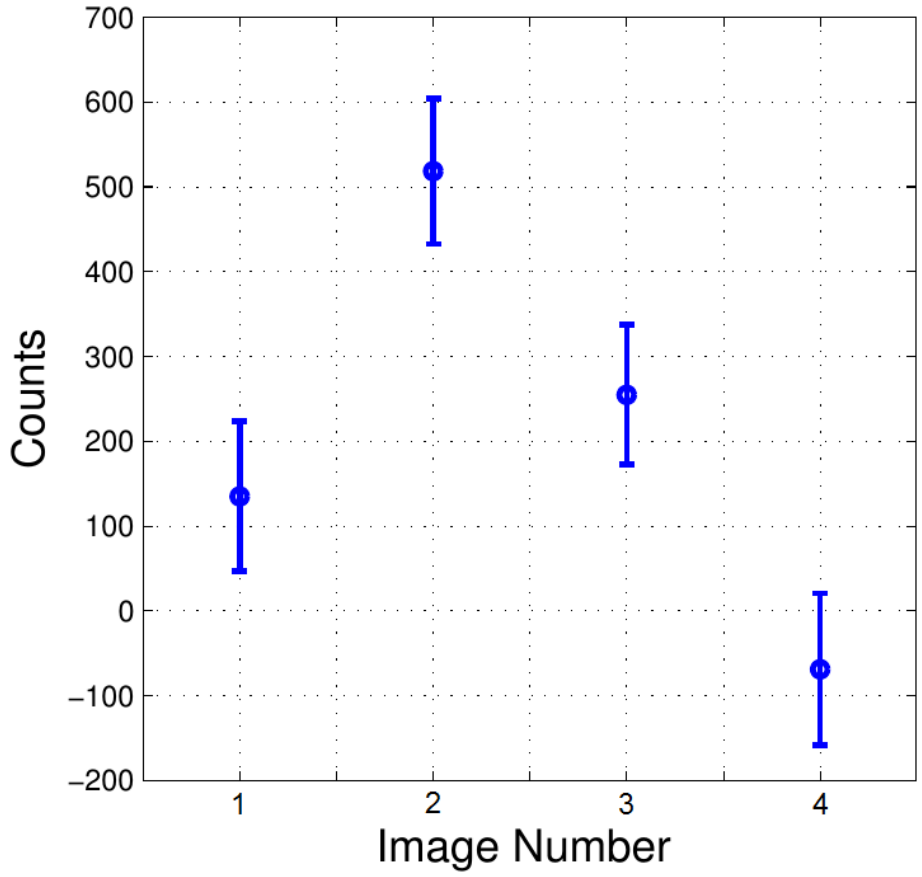

FIGURE 7.2: Example of EDM data in a 1-hour measurement sequence. These are the four points in the sequence that have atoms; the data in the figure is after background subtraction. Image 2, the largest one, is used for normalization.

The timing sequence for the high voltage is also important; we design it so that there is a large buffer between the E-field and any optical pulse. It is complicated, however, by the charging up and down time of the high voltage due to capacitance in the HV cables and delays in the BNC cables. The timing sequence used is given below; the measurements of the HV are done with an oscilloscope (monitoring the output of the

HV divider described in Section 5.2), and are accurate to about 10 ms in time and 1% in voltage.

TABLE 7.1: HV Timing

Event	Time since beginning of Measurement Cycle (s)
Polarizing Pulse Trigger	7.69862
HV Actually Starts Ramping Up	7.80
HV within 1% of Maximum	8.00
HV Starts to Ramp Down	9.30
HV within 1% of Fully Off	9.60
Spin Readout Pulse Trigger	9.69112

7.2 Expected Statistical Sensitivity

It is useful to estimate the sensitivity of the experiment, given current parameters. This not only allows us to make sure we understand the EDM results, but also provides insight for future upgrades. The following treatment was originally worked out by Michael Bishof. For a pair of measurements, one with the E-field parallel and one with the E-field anti-parallel, the EDM sensitivity scales as

$$\Delta d = \frac{h}{4E}\sqrt{2}\Delta\nu$$

where $\Delta\nu = \Delta\omega/2\pi$ is the difference in precession frequencies for the two electric field conditions. The population fraction of the bright magnetic sublevel oscillates due to Larmor precession:

$$p(t) = \frac{A}{2}[1 - P\cos(2\pi\nu t)]$$

Letting A=P=1, and limiting ourselves to the points on the sine wave of maximum EDM sensitivity, we have

$$\frac{\Delta p}{\Delta\nu} = \frac{2\pi t}{2}$$

$$\Delta d = \frac{\hbar \Delta p \sqrt{2}}{4E\tau}$$

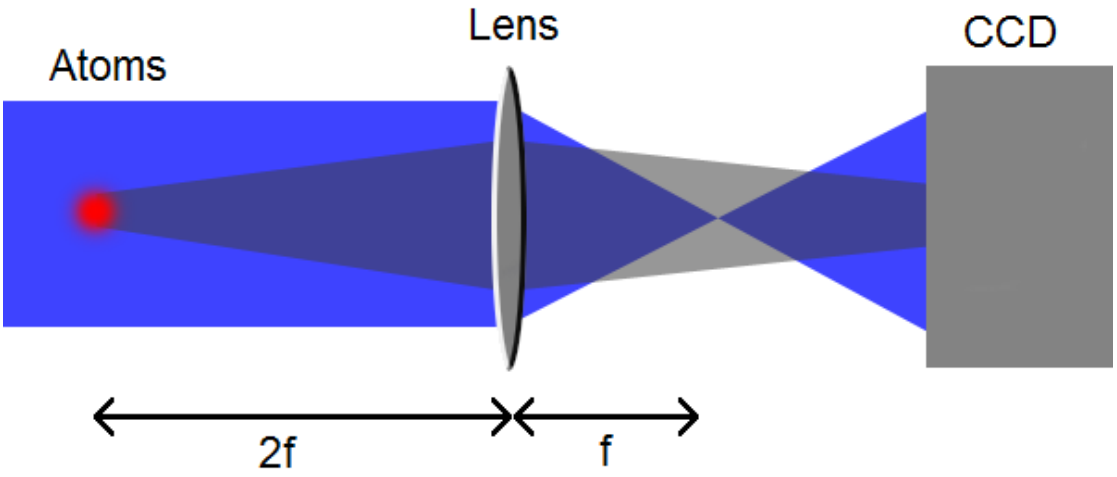

FIGURE 7.3: Diagram of the optics used in absorption imaging (not to scale).

We now consider the population fractions used to construct the precession curve. We use absorption imaging to construct the curve; a diagram of the optical setup is given in Figure 7.3. A collimated blue beam intersects the atom cloud and creates a shadow; the shadow is then imaged onto a CCD by a 2f-to-2f lens. The remaining blue beam will be a souce of background, and produce photon shot noise. Let N be the number of atoms in the absorption image, $\tilde{N}$ be the number of atoms in the normalization image, and N_+ be the number of atoms in the bright magnetic sublevel. Then we have

$$p_{meas} = \frac{N_+}{N}$$

$$\Delta p_{meas} = \sqrt{\frac{\Delta N_+^2}{N^2} + \frac{\Delta N^2 \cdot N_+^2}{N^4}}$$

In the following treatment, we use tildes above variables to indicate parameters in the normalization image, and a lack of a tilde to indicate the variable occurs in the "signal" image. There is a correction factor C between N and $\tilde{N}$, given by $N = \tilde{N} \cdot C$, due to the exponential decay of atoms in the trap. In this treatment we will ignore the uncertainty in that factor, as in practice that error is negligible compared to the other sources of error. Defining M to be the average number of scattered photons per atom, $\bar{P_L}$ to be the average number of photons in the detection pulse, $\tilde{P_L}$ to be the number of photons in the detection pulse, and $\tilde{P_a}$ to be the number of photons scattered by atoms, we have

$$N = \frac{1}{M}[\bar{P_L} - (\tilde{P_L} - C \cdot \tilde{P_a})]$$

$$N_+ = \frac{1}{M}[\bar{P_L} - (P_L - P_a)]$$

$$\Delta N = \frac{1}{M}\sqrt{\Delta\tilde{P_L}^2 + C^2 \cdot \Delta\tilde{P_a}^2}$$

$$\Delta N_+ = \frac{1}{M}\sqrt{\Delta P_L^2 + \Delta P_a^2}$$

Now we look at each noise term. The noise in the background is given by photon shot noise:

$$\Delta P_L = \sqrt{\bar{P_L}}$$

The uncertainty in the scatter photons is given by quantum projection noise

$$\Delta\tilde{P_a} = \tilde{N}M\Delta\tilde{p}_{QPN} = \tilde{N}M\sqrt{\frac{\tilde{p}(1-\tilde{p})}{\tilde{N}}} = 0$$

$$\Delta P_a = \tilde{N}M\Delta p_{QPN} = NM\sqrt{\frac{p(1-p)}{N}} = M\sqrt{\frac{N}{4}}$$

After some algebra we get

$$\Delta p_{meas} = \sqrt{\frac{5\bar{P}_L}{4M^2N^2} + \frac{1}{4N}}$$

This is the population uncertainty per shot; of course, we can improve the sensitivity by doing multiple measurements. The total number of measurements is given by the ratio of the total experimental time T to the time per measurement $\tau + T_d$, where T_d is the "dead time" per measurement. Therefore the EDM sensitivity is given by

$$\Delta d = \frac{\hbar\sqrt{2}}{4E\tau}\sqrt{\frac{5\bar{P}_L}{4M^2N^2} + \frac{1}{4N}}\sqrt{\frac{\tau + T_d}{T}} \tag{7.1}$$

For the characteristic parameters of our experiment, assuming 2 days of actual data collection, this formula predicts an EDM sensitivity of 3×10^{-22} $e\cdot$ cm.

7.3 Experimental Results

Two runs with ^{225}Ra were performed; one in October 2014 with 3 mCi loaded into the oven and one in December 2014 with 6 mCi. In both cases the actual amount of activity that was devoted to the EDM run was significantly less; in the October run the first week was spent demonstrating detection of 1st fringe of spin precession and demonstrating spin precession at 2 seconds without application of an electric field. In the December run problems with the 1D MOT current supply and coil prevented data collection for the first week. Therefore each run represents only 40-50 hours of data collection, using a partly-depleted oven. The data for both runs is shown in Figure 7.4, including the spin detection data with the E-field on, pointing parallel to the B-field, anti-parallel, or with the E-field off as functions of the free precession time. The E-field is at its maximum value of 67 kV/cm for 1.2 s during the 2 s of precession. Each data point was corrected for trap losses using the measured trap lifetime. Data taken under the three E-field configurations were simultaneously fit to a combined set of equations:

$$y_{\text{E}-\text{field Off}} = \frac{A}{1+P}\left[1 - P\cos(\omega t)\right]$$
$$y_{\text{Parallel, Anti}-\text{Parallel}} = \frac{A}{1+P}\left[1 - P\cos(\omega t + \theta \pm \Delta\phi/2)\right]$$

Five parameters A (normalization), P (atom polarization), ω (precession frequency with E-field off), θ and $\Delta\phi$ (defined below) were fit without constraints. $y_{\mathrm{E-field\,Off}}$ is the integrated signal in Image #4 (see Figure 7.1) after normalization to Image #2 and background subtraction. Similarly, $y_{\mathrm{Parallel,\,Anti-Parallel}}$ is derived from Image #3. An EDM would cause a polarity-dependent phase shift, $\Delta\phi$, with the EDM given by $d = \hbar\Delta\phi/(4E\tau)$ (here τ is the spin precession time with the E-field applied). An effect common to both E-field polarities would produce an overall phase offset θ. $\Delta\phi$ was found to be uncorrelated with the other fit parameters. In both of the experimental runs, the measured EDM was found to be consistent with zero: $-(4.0 \pm 5.2) \times 10^{-22}$ e·cm in the first measurement done with 3 mCi of ^{225}Ra, and $(0.6 \pm 2.9) \times 10^{-22}$ e·cm in the second one, done with 6 mCi of ^{225}Ra. The uncertainties listed above are statistical only. The systematic effects will be discussed in more detail in the following chapter.

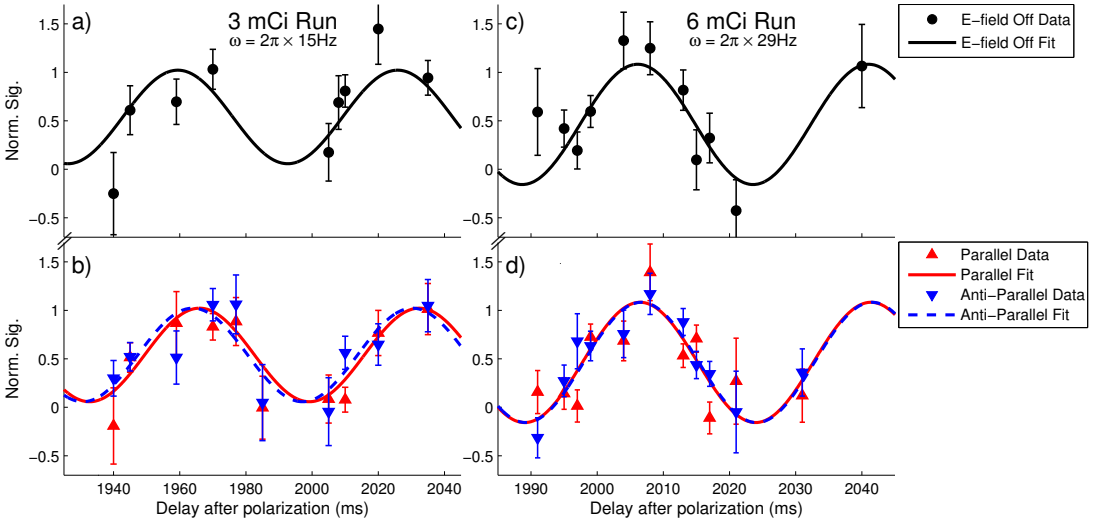

FIGURE 7.4: Precession curves from the two experimental runs. Panels (a) and (b) are based on the first run, which used a 3 mCi ^{225}Ra source, and panels (c) and (d) are based on the second run with 6 mCi. The panels show data with the E-field parallel to the B-field (red), E-field anti-parallel to the B-field (blue), and E-field off (black). Between the two runs the bias B-field was deliberately altered, resulting in the two different precession frequencies. An EDM would cause a phase difference between the E-field parallel and E-field anti-parallel fit curves. The global fits for the 3 mCi and 6 mCi runs yield $\chi^2/24 = 1.11$ and $\chi^2/28 = 1.35$, respectively.

7.4 Correlations Studies

To be confident that the errors listed above are accurate, we perform a detailed study of correlations between the various fit parameters. Below are the corelations matrices

for the two runs; for clarity, the variables are listed in the following order: A, P, ω, θ, $\Delta\phi$. For example, the square root of the first element is the 1-sigma uncertainty in A. Of particular importance is the last row/column–the correlations between $\Delta\phi$ and the other fit parameters.

$$\text{CorrelationsMatrixForOctober} = \begin{vmatrix} A & P & \omega & \theta & \Delta\phi \\ 0.0056 & 0.0069 & 0.0000 & -0.0003 & 0.0013 \\ 0.0069 & 0.0329 & -0.0002 & 0.0010 & -0.0006 \\ 0.0000 & -0.0002 & 0.0002 & -0.0000 & 0.0018 \\ -0.0003 & 0.0010 & -0.0000 & 0.0198 & -0.0005 \\ 0.0013 & -0.0006 & 0.0018 & -0.0005 & 0.0240 \end{vmatrix} \tag{7.2}$$

$$\text{CorrelationsMatrixForDecember} = \begin{vmatrix} A & P & \omega & \theta & \Delta\phi \\ 0.0055 & 0.0096 & -0.0007 & 0.0016 & 0.0021 \\ 0.0096 & 0.0528 & -0.0053 & 0.0034 & 0.0138 \\ -0.0007 & -0.0053 & 0.0056 & -0.0002 & 0.0119 \\ 0.0016 & 0.0034 & -0.0002 & 0.0604 & 0.0004 \\ 0.0021 & 0.0138 & 0.0119 & 0.0004 & 0.0537 \end{vmatrix} \tag{7.3}$$

Another source of concern comes from our algorithm for background subtraction and normalization. We apply an offset to the integrated images based on data taken without atoms, and normalize the data with respect to the measured lifetime with ^{226}Ra. As a check, we vary both of those two parameters and see how the fit parameters are affected. Figures 7.5 and 7.6 show the effect of varying the applied offset, and Figures 7.7 and 7.8 show the effect of varying the lifetime used for normalization. In all cases the parameter relevant to the EDM, $\Delta\phi$, is insensitive.

We can now combine the October and December runs together and calculate an EDM $d(^{225}\text{Ra}) = -(0.5 \pm 2.5_{\text{stat}}) \times 10^{-22}$ e·cm, where the error given is statistical only. The systematics will be discussed in the next section.

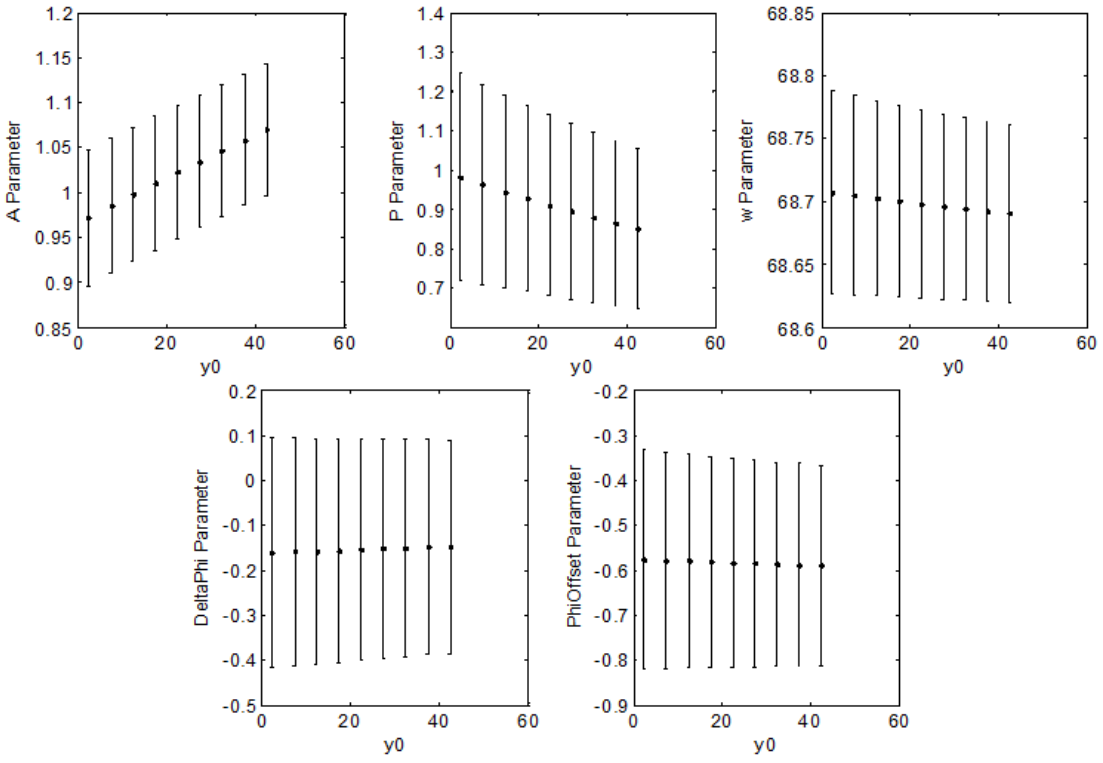

FIGURE 7.5: Varying the y-offset and determining the dependence of the five fit parameters for the October data.

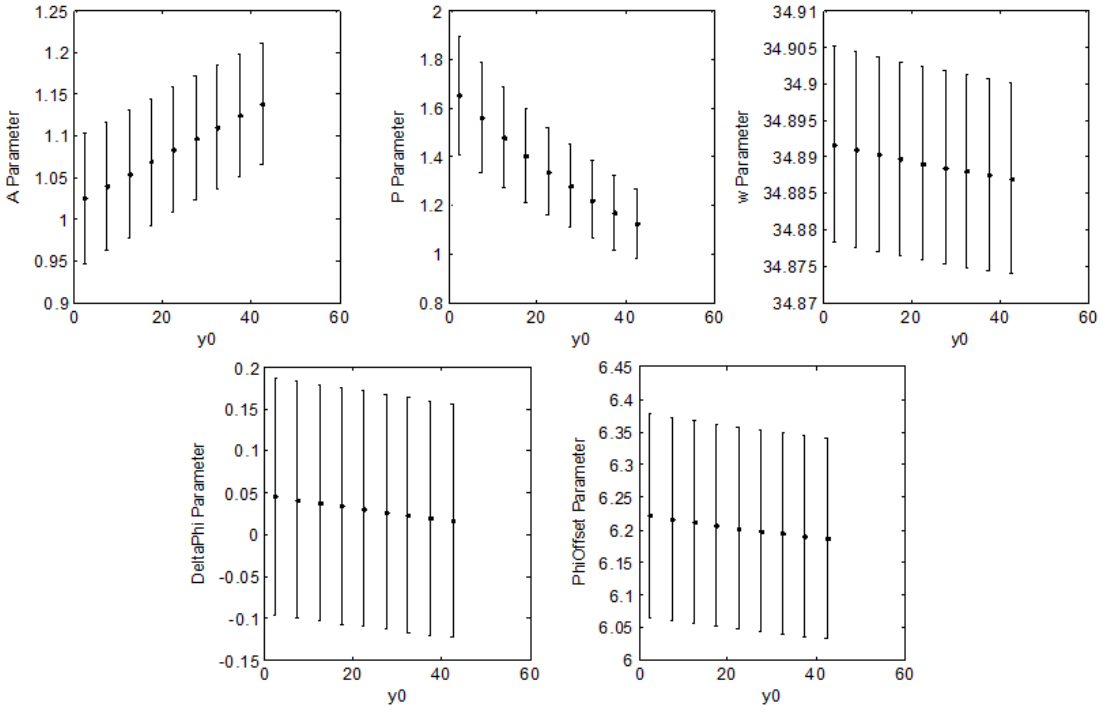

FIGURE 7.6: Varying the y-offset and determining the dependence of the five fit parameters for the December data.

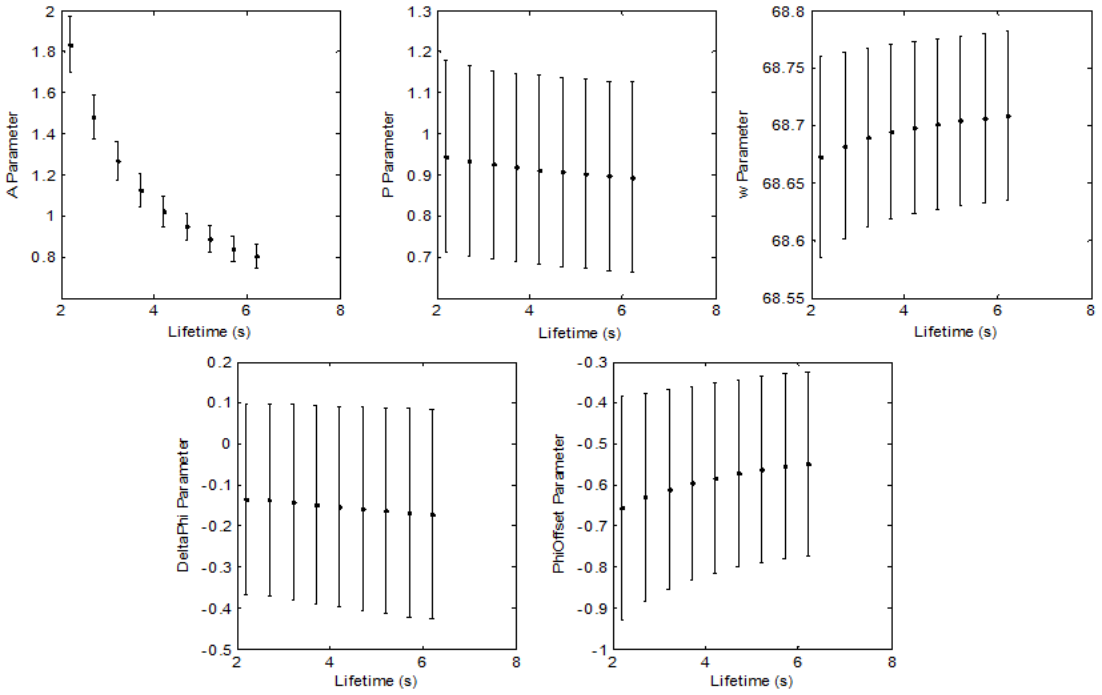

FIGURE 7.7: Varying the lifetime used for normalization and determining the dependence of the five fit parameters for the October data.

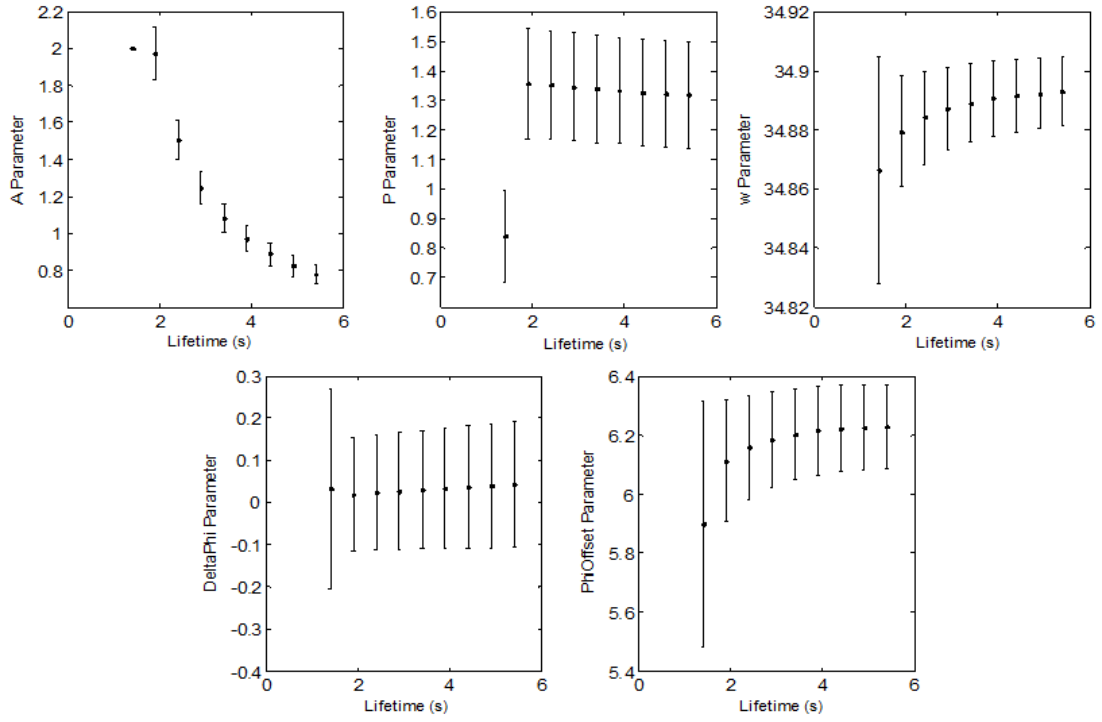

FIGURE 7.8: Varying the lifetime used for normalization and determining the dependence of the five fit parameters for the December data.

Chapter 8

Discussion of EDM Sytematics

An advantage that EDM experiments have is that "true" systematics must appear linear in electric field; effects that are independent of electric field or scale as E^2 might potentially reduce statistical sensitivity, but would not produce a "fake" EDM. Table 8.1 shows the (very conservative) 2-sigma limits on the systematic effects to which this experiment is sensitive. Note that because all the systematic effects are negligible compared to the statistical sensitivity, there is no need to apply any correction to compensate for a particular effect.

TABLE 8.1: List of systematic effects. Limits given are 2-sigma.

Systematic Effect	d_F (x $10^{-26} e\cdot$ cm)
Imperfect E-field Reversal	2000
Blue Probe Frequency Correlations	9
Current Supply Correlations	4
Standing-wave ODT Power Corr.	4
External B-field Correlations	4
E × v effects	0.5
E-field Pulsing	0.3
Leakage Current	0.2
Stark Interference	0.1
Geometric Phase	10^{-9}

8.1 Imperfect E-field Reversal

There are many effects that are quadratic in the electric field. Effects quadratic in E-field do not produce an EDM-like signal, unless the E-field reversal is imperfect. The voltage

difference between the electrodes is recorded for each polarity; the E-field imbalance is found to be less than 0.7%. There are two basic approaches that can be used to determine the magnitude of this systematic: modelling, and direct measurement with atoms. First I will give an example of one such effect, then explain how the effect can be constrained with atoms. To be conservative, we follow the lead of the mercury EDM experiment and ultimately choose to constrain the effect with atoms.

One potential systematic effect comes from the presence of both an electric field gradient and a magnetic field gradient. The atoms can experience a force due to the electric field gradient given by $\vec{F} = \vec{p} \cdot \boldsymbol{\nabla}\vec{E} = \alpha\vec{E}\boldsymbol{\nabla}\vec{E}$. This force will cause the atoms to displace, until the force due to the electric field gradient is balanced by the restoring force of the ODT. We can then calculate the displacement at which this balance occurs, assuming typical trap parameters and conservative values for the electric field gradient. Because the E-field is not quite the same between the two polarities, the displacement will be slightly different for the two polarities. The differential displacement between the two configurations is expected to be less than 20 nm. We can then calculate the maximum expected B-field difference the atoms would experience, based on the constraint on the linear gradient placed by magnetometry measurements. The difference in precession frequencies is below 300 nHz, resulting in an EDM systematic below 2×10^{-26} $e \cdot$ cm.

The effects due to imperfect E-field switching can also be constrained by direct measurements with trapped ^{225}Ra atoms. We use three E-field configurations (parallel, anti-parallel, and off) to directly measure both the linear and quadratic terms; the term that gives the phase a quadratic dependence on E-field allows us to place a limit on any potential E^2 systematics. The ability to place a limit on this effect is, therefore, limited by the statistical uncertainty of the spin precession fit − as this uncertainty improves, the limit placed on this effect will improve as well. For now, the quadratic effect was found to be below 2×10^{-23} e·cm for the 3 mCi experimental run and below 5×10^{-24} e·cm for the 6 mCi one.

8.2 Current Supply Correlations

Correlations between the HV power supply and the cosine theta coil current supply, which could potentially occur due to a ground loop, can produce a fake EDM by changing

the precession frequency linearly with the applied E-field. The false EDM can be written as

$$d_F = \frac{\mu B_0}{E_0}\frac{\Delta I}{I_0} \tag{8.1}$$

where $\mu = 0.7338\mu_N$. To measure potential correlations, the current supply output is continuously measured by a DMM and recorded. The correlation was measured twice; in January 2015 it was measured to be below 30 nA (1 ppm) at the 2-sigma level, and in April 2015 it was measured to be below 4 nA (0.1 ppm) at the 2-sigma level, in both cases consistent with zero; our ability to limit this effect was due to the measured noise on the current supply.

8.3 Blue Laser Frequency Correlations

Correlations between the blue probe frequency and the polarity of the HV represent a potential systematic. A change in the blue laser frequency would change the radium scattering rate, resembling an EDM. Transmission through a Zerodur cavity was used to measure the shift, as the Zerodur cavity's shape is expected to be insensitive to the HV. The laser was locked on resonance with a cavity mode, and transmission was measured with a battery-powered photodiode. No correlation was measured, with the systematic upper bound (a fractional scattering rate of 0.002 at the 2-sigma level) limited by the experimental sensitivity. As the statistical uncertainty of the EDM measurement improves, this technique can be made more sensitive by performing the measurement on the side of the transmission resonance rather than the peak. This effect would be 7.4×10^{-24} $e\cdot$ cm if measuring one point on the slope of the precession curve, but the effect is heavily suppressed by taking approximately equal amounts of data on slopes of either sign (i.e. data of approximately equal statistical sensitivity). This effect would then show up as a correlation between the HV and the amplitude of the precession curve, and is therefore suppressed by the correlation between those fit parameters. The fractional scattering rate correlation would change the observed precession amplitude by 0.015-sigma, resulting in a phase shift change of 0.002-sigma. There is an additional suppression because the E-field is mostly off by the time the image is taken (given by the 160 ms 1/e time and the 390 ms between the beginning of the ramp down and the

image), resulting in a suppression factor of 0.09. With these suppressions the effect is less than 9×10^{-26} e·cm.

8.4 Leakage Current

Leakage current between the electrodes is a particularly troubling systematic, as it mimics an EDM in almost every way. We assume the most conservative model for the leakage current, in which an electron beam passes next to (but not through) the atom cloud, producing a magnetic field over the atomic ensemble. The electron's acceleration is set by the strength of the electric field, so we know the time it takes for the beam to travel between the gaps:

$$\frac{1}{2}\frac{eV_0}{lm_e}t^2 = l \tag{8.2}$$

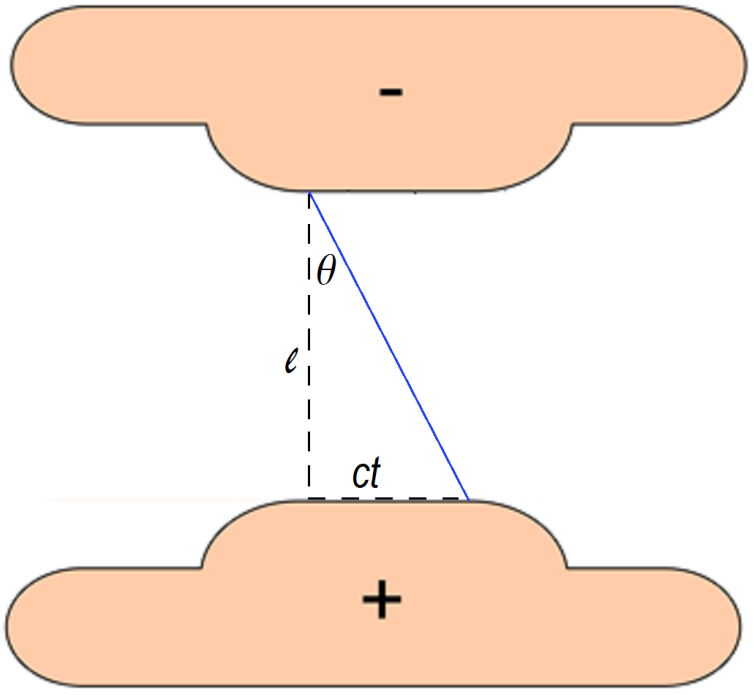

FIGURE 8.1: The geometry used in the calculation of the leakage current systematic, due to a potential electron beam between the electrodes.

The simplest case is that the electron beam travels directly between the two electrodes, along a path parellel to the electric field lines. However, if the electron beam does not

travel at an angle with respect to the electric field lines, the magnetic field it produces will be perpendicular to the electric field so it won't produce a systematic (the magnetic field will add in quadrature to the bias magnetic field, rather than linearly). Further, for a sufficiently high electric field this simple model would result in an electron velocity faster than the speed of light. Therefore we consider an electron beam with initial velocity of zero in the direction parallel to the electric field lines, and velocity equal to the speed of light perpendicular to that (see Figure 8.1. The angle of the beam with respect to the electric field lines is given by

$$\tan\theta = \frac{ct}{l} = \sqrt{2m_e c^2/eV_0} \tag{8.3}$$

The frequency shift is

$$\frac{2d_F E}{\hbar} = \frac{2\mu}{\hbar}\frac{\mu_0 I}{2\pi r}\sin\theta \tag{8.4}$$

The fake EDM is therefore given by

$$d_F = \frac{\mu}{E}\frac{\mu_0 I}{2\pi r}\sin\theta \tag{8.5}$$

The leakage current is recorded continuously by a computer. For $V_0 = 16$ kV, E-field of 80 kV/cm, r of 50 μm, and I of 2 pA (measured in December 2014) gives $d_F = 2\times10^{-27}$ e·cm. A comagnetometer would allow us to better constrain this effect.

8.5 Optical Lattice Power Correlations

Any residual circularly-polarized light from the standing-wave ODT beams would produce a vector shift, which would appear as a EDM-like signal if the ODT power was correlated with the polarity of the E-field. Even if uncorrelated with the E-field, such a vector shift could produce statistical noise. This effect is heavily suppressed, however, by ensuring the ellipticity is below 10^{-2}, and by ensuring the standing-wave k-vector is perpendicular to the B- and E-fields. The analysis used to calculate the vector shift $\Delta\nu$

due to the standing wave ODT follows from the treatment given in [51]; the vector shift is estimated to be 100 Hz. The form of the vector shift is

$$\Delta\nu = \pm\nu_V(|\epsilon_L|^2 - |\epsilon_R|^2)m\cos\theta \tag{8.6}$$

It is important to note that if one reverses the direction of the ODT (say by reflecting at normal incidence on a mirror), both the handedness and $\cos\theta$ will change sign. This means that the effect is enhanced, rather than suppressed, by using a retroreflected ODT beam. The fake EDM signal due to this effect will be

$$d_F = \eta\frac{\Delta\nu}{2\pi}\frac{\Delta P}{P_0}\frac{\hbar}{2E} \tag{8.7}$$

where η represents the various suppressions. The ODT power correlations were measured to be less than 153 ppm (2-sigma), resulting in a fake EDM of $d_F = 4\times10^{-26}$ e·cm.

8.6 External B-field Correlations

Another concern is our imperfect magnetic shielding; if the HV is somehow able to affect the magnetic field environment in the lab, then this new B-field would bypass our magnetic shielding and lead to an EDM-like signal, given by

$$d_F = \frac{\mu B_{internal}}{E_0}\frac{\eta\Delta B_{external}}{B_{internal}} \tag{8.8}$$

where η is the shielding factor of our mu-metal. Here "internal" refers to the bias field within the mu-metal shields, and "external" refers to the ambient magnetic field outside the shields. Therefore a fluxgate as placed in the lab outside the magnetic shields to measure the HV-induced magnetic field, and the shielding factor of the mu-metal (20,000) was used to convert that into an estimate of the B-field at the atoms. The external magnetic field of 250 mG was found to correlate with the HV below 96 ppm.

8.7 E × v Effects

E × v effects are a potential systematic arising from the motional B-field of a particle, which couples linearly to the applied E-field. Using the Doppler velocity of 2.3 cm/s and a field of 100 kV/cm we find that this effect is equivalent to a magnetic field of 25 nG, or 20 μHz. This systematic is heavily suppressed by the low temperature of our atoms, and additionally suppressed by aligning the E- and B-fields to be (nearly) parallel. There is an additional effect not included in this analysis which should further suppress the effect, which is that the effect is identically zero if the atom's motion is purely harmonic and separable.

8.8 E-field Pulsing

In these two experimental runs the E-field was ramped up in 160 ms, left on for 1.2 s, then ramped down in 160 ms. This was done to suppress the frequency shift in the probe transition due to the DC electric field. However, pulsing the E-field will produce a small induced magnetic field which is a potential EDM systematic. The dominant effect comes from the induced B-field due to the increasing local E-field (a second effect due to the charging current in the long wires connected to the electrodes turns out to be a much smaller effect). The induced B-field is given by

$$\oint \vec{B} \cdot d\vec{l} = \frac{1}{c^2} \int \frac{\partial E}{\partial t} \cdot d\vec{S} \tag{8.9}$$

We consider a loop defining a plane normal to the electric field; the above equation then becomes

$$B(2\pi r) = \frac{1}{c^2} \frac{\partial E}{\partial t} (\pi r^2) \tag{8.10}$$

Here r is the displacement of the atoms from the center of the electrodes. Solving for B and assuming a linear ramp for simplicity gives

$$B = \frac{r}{2c^2} \frac{\partial E}{\partial t} = \frac{r E_0}{2c^2 t_0} \tag{8.11}$$

Note that this B-field will be perpendicular to the electric field, and thus will be nearly perpendicular to the bias B-field, and there will be a large (at least factor of 10) supppression due to geometry, which we do not incude here. The phase error in spin precession will be

$$\phi = \frac{2\mu B t_0}{\hbar} = \frac{r\mu E_0}{c^2\hbar} \tag{8.12}$$

This phase error will result in a fake EDM signal of

$$d_F = \frac{2\hbar\phi}{E_0 T} \tag{8.13}$$

This effect is suppressed by using opposite polarities of nearly the same magnitude, with the suppression given by the E-field reversal imbalance of 0.7%. The effect of a single ramp is predicted to be $d_F = 3 \times 10^{-27}$ e·cm, for a displacement of 1 cm (which is unrealistically large). Additionally, there will be a suppression due to the fact that in each measurement cycle we will ramp up and down; this suppression is not included in the above analysis.

8.9 Stark Interference

Stark interference is an effect linear in both the DC electric field and the E-field of the standing-wave ODT beam, due to interference between the fields of the laser and the DC E-field. The analysis used to quantify this effect follows from the treatment given in [51]; the Matlab code used to calculate this effect is given in Appendix D. The analysis was worked out in detail by Matt Dietrich, and is overviewed here. The functional form of the effect can be written as a sum of two vector products:

$$\Delta E = \nu_1(\hat{b}\cdot\hat{\sigma})(\hat{\epsilon}\cdot\hat{\epsilon_s}) + \nu_2(\hat{b}\cdot\hat{\epsilon_s})(\hat{\epsilon}\cdot\hat{\sigma}) \tag{8.14}$$

Figure 8.2 shows six Feynmann diagrams that are the dominant contributions to the Stark interference effect. Of these, only the top two involve the magntic moment of the excited state; the bottom four involve the magnetic moment of the ground state, which is smaller by a factor of 10^3 in our case. Therefore only the top two plots are included in the analysis. We also choose to consider only the two dominant transitions from the

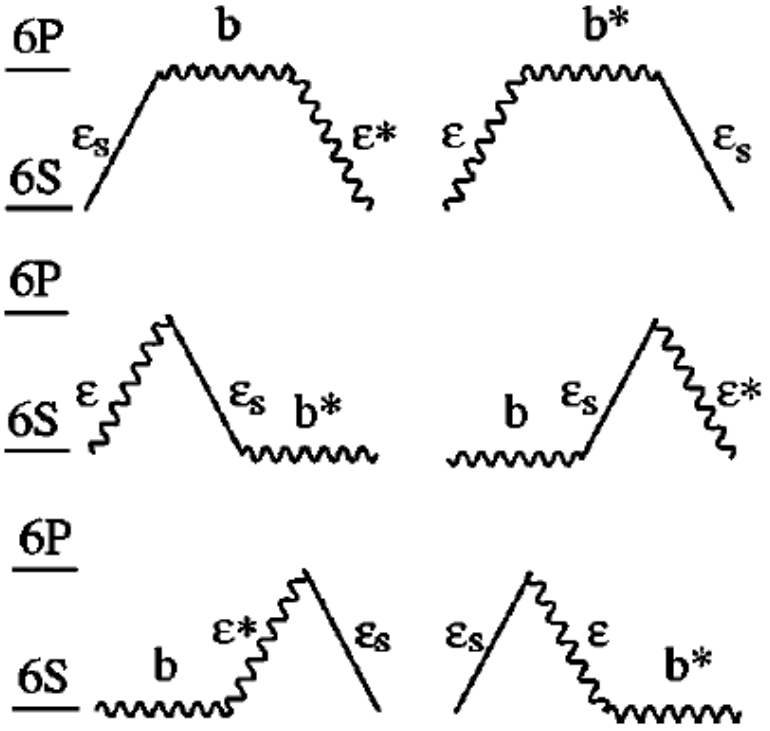

FIGURE 8.2: Six Feynmann diagrams relevant to the calculation of the Stark interference systematic. Adapted from [51].

ground state; to ${}^1P_1$ and to ${}^3P_1$. The upper left diagram results in an energy shift given by

$$\Delta E = \frac{\mu_B E_s E_0^2}{4c\hbar^2} \sum_{S,F,m_F,F',m_{F'},F'',m_{F''}} [\frac{1}{(\omega'_F-\omega)(\omega''_F-\omega)} \left\langle {}^1S_0 F m_F \right| \epsilon^\star \cdot r \left| {}^{2S+1}P_1 F'' m''_F \right\rangle$$
$$\left\langle {}^{2S+1}P_1 F'' m_{F''} \right| b \cdot (L+2S) \left| {}^{2S+1}P_1 F' m'_F \right\rangle \left\langle {}^{2S+1}P_1 F' m_{F'} \right| \epsilon_s \cdot r \left| {}^1S_0 F m_F \right\rangle + c.r.] \tag{8.15}$$

The other diagram results in an energy shift of similar functional form, except that ϵ and ϵ_s are switched, b becomes $b^\star$, and $\epsilon^\star$ becomes ϵ. This equation can be rewritten in terms of spherical tensor operators:

$$\Delta E = \frac{\mu_B E_s E_0^2}{4c\hbar^2} \sum_{S,F,m_F,F',m_{F'},F'',m_{F''}} [\frac{(-1)^{n_\epsilon}}{(\omega'_F-\omega)(\omega''_F-\omega)} \left\langle {}^1S_0 F m_F \right| T^1_{-n_\epsilon} \left| {}^{2S+1}P_1 F'' m''_F \right\rangle$$
$$\left\langle {}^{2S+1}P_1 F'' m_{F''} \right| T^1_{-n_b} \left| {}^{2S+1}P_1 F' m'_F \right\rangle \left\langle {}^{2S+1}P_1 F' m_{F'} \right| T^1_{-n_s} \left| {}^1S_0 F m_F \right\rangle + c.r.] \quad (8.16)$$

where we have used the relation $(T^1_n)^\star = (-1)^n T^1_{-n}$. The Wigner-Eckhart theorem states:

$$\left\langle \alpha'; j', m' \right| T^{(k)}_q \left| \alpha; j, m \right\rangle = \left\langle \alpha'; j' \right| |T^{(k)}_q| \left| \alpha; j \right\rangle \left\langle j' m' \right| |kq; jm\rangle \quad (8.17)$$

Where the first term on the right hand side is the reduced matrix element, and the second term on the right hand side is the Clebsch-Gordon coefficient. It is then possible to write the energy shift as

$$\Delta E(F, m_F, n_s, n_b, n_\epsilon) = \frac{\mu_B E_s E_0^2}{4c\hbar^2} \sum_{S,F',m_{F'},F'',m_{F''}} [\frac{(-1)^{n_\epsilon} G(-n_\epsilon, n_b, n_s)}{(\omega'_F-\omega)(\omega''_F-\omega)} +$$
$$\frac{(-1)^{n_b} G(n_\epsilon, -n_b, n_s)}{(\omega'_F+\omega)(\omega''_F+\omega)} + \frac{(-1)^{n_b} G(n_s, n_b, n_\epsilon)}{(\omega'_F-\omega)(\omega''_F-\omega)} + \frac{(-1)^{n_\epsilon} G(n_s, n_b, -n_\epsilon)}{(\omega'_F+\omega)(\omega''_F+\omega)}] \quad (8.18)$$

Where G is defined to be

$$G(F, m_F, F', m'_F, F'', m''_F, n_1, n_b, n_2) = (2F'+1)(2F''+1)$$
$$(-1)^{1+3F''+7I+J''+2j'-m_F-m'_F-m''_F+3F'} \times \left\{ \begin{array}{ccc} J'' & 1 & J' \\ F' & I & F'' \end{array} \right\} \left(\begin{array}{ccc} I & 1 & F'' \\ -m_F & n_1 & m''_F \end{array} \right)$$
$$\left(\begin{array}{ccc} F'' & 1 & F' \\ -m''_F & n_b & m'_F \end{array} \right) \left(\begin{array}{ccc} F' & 1 & I \\ -m'_F & n_2 & m_F \end{array} \right) \times |\left\langle {}^1S_0 \right| |d| \left| {}^{2S+1}P_1 \right\rangle|^2 \times \left\{ \begin{array}{ll} \sqrt{2/3} & \text{if } S=0; \\ 3/\sqrt{6} & \text{if } S=1. \end{array} \right. \quad (8.19)$$

This is sufficient information to calculate the total energy shift; however, we would like to write it in terms of ν_1 and ν_2. Recognizing that $x = \sqrt{1/2}(T^{(1)}_{-1} - T^{(1)}_{+1})$, we can finish by writing

$$\nu_1 = -1/2[\Delta E(1/2,-1,0,-1)+\Delta E(1/2,1,0,1)-\Delta E(1/2,-1,0,1)-\Delta E(1/2,1,0,-1)- [\Delta E(-1/2,-1,0,-1)+\Delta E(-1/2,1,0,1)-\Delta E(-1/2,-1,0,1)-\Delta E(-1/2,1,0,-1)]] \tag{8.20}$$

and

$$\nu_2 = 1/2[\Delta E(1/2,0,-1,-1)+\Delta E(1/2,0,1,1)-\Delta E(1/2,0,-1,1)-\Delta E(1/2,0,1,-1)- [\Delta E(-1/2,0,-1,-1)+\Delta E(-1/2,0,1,1)-\Delta E(-1/2,0,-1,1)-\Delta E(-1/2,0,1,-1)]] \tag{8.21}$$

We are finally ready to determine the size of the effect. Figure 8.3 shows the magnitude of the Stark interference systematic after all suppressions have been included. At 1550 nm, the expected size for a 40 W traveling wave beam with a 100 micron waist is 500 μHz. The effect is identically zero in a perfect standing wave; given measurements of the relative powers in our first-pass and second-pass ODTs we estimate that we have retroreflected more than 95% of our ODT beam, giving us a conservative suppression of 10^{-1}. Further, Stark interference is also zero when the standing wave polarization is perpendicular to the static electric field; estimates of the relative alignment of the E- and B-fields give us a suppression of 10^{-2}.

8.10 Geometric Phase

Geometric phase effects are due to the atoms sampling B-field inhomogeneities, leading to a geometric phase that results in an apparent frequency shift. The effect is negligible for atoms moving in a harmonic well unless the harmonic frequency is near the Larmor frequency. This effect is quantified by [52]:

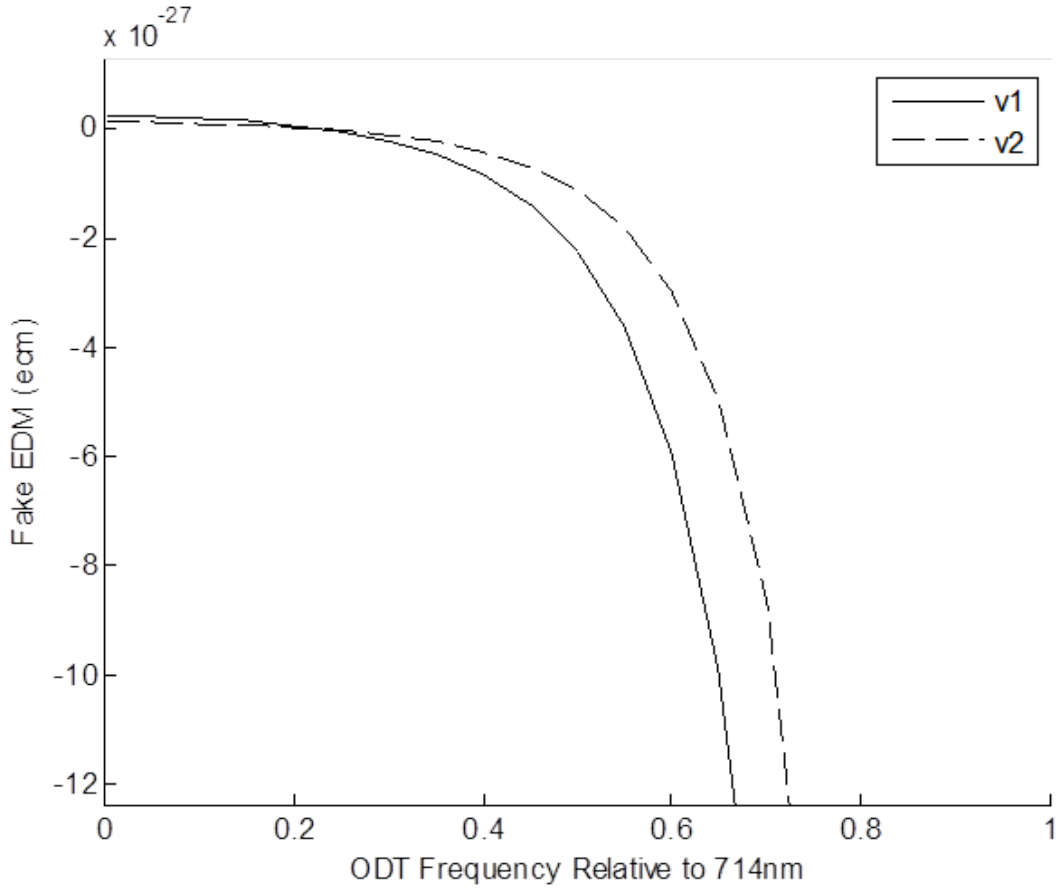

FIGURE 8.3: Size of the Stark interference systematic as a function of standing wave ODT frequency, including all suppressions. We operate with a 1550 nm ODT, putting us at 0.46 on the x-axis.

$$d_{af} = -\frac{J\hbar}{2}\left(\frac{\partial B_{0z}/\partial z}{B_{0z}^2}\right)\frac{v_{xy}^2}{c^2}\left[1-\frac{\omega_r^2}{\omega_0^2}\right]^{-1} \tag{8.22}$$

where ω_0 is the Larmor frequency and ω_r is the trap frequency. The effect is suppressed by using trap frequencies much higher than our precession frequency, as well the B-field gradient over our relatively small atom cloud (the B-field gradient is < 0.1 %/cm). Currently our Larmor precession frequency varies between 10 Hz and 30 Hz, depending on the bias B-field we apply, and our axial trap frequency is about 10 kHz. If in the future we chose to operate with a traveling wave trap this will move the trap frequency much closer to the precession frequency, and the effect will increase; the false EDM in that case is given by

$$d_{af} = -\frac{J\hbar}{2}\left(\frac{\partial B_{0z}}{\partial z}\right)\frac{\gamma^2 R^2}{c^2}\left[1 - \frac{\omega_0^2}{\omega_r^2}\right]^{-1} \tag{8.23}$$

where γ is the gyromagnetic ratio and R is the radius of trap. The size of the effect depends on the specific choices of trap frequency and precession frequency; if they are within 1% of each other the size of the systematic can increase by 1-2 orders of magnitude.

8.11 Result

Recognizing that the systematic effects are all negligible at the present level of sensitivity, we combine the October and December runs together and calculate an EDM $d(^{225}\mathrm{Ra}) = -(0.5 \pm 2.5_{\mathrm{stat}} \pm 0.2_{\mathrm{syst}}) \times 10^{-22}$ e·cm, and, hence, set an upper limit: $|d(^{225}\mathrm{Ra})| < 5.0 \times 10^{-22}$ e·cm (95% confidence).

Chapter 9

Discussion of EDM Results

Using our experimental result of $|d(^{225}\text{Ra})| < 5.0 \times 10^{-22}$ e·cm (95% confidence) and the estimate of the electron cloud shielding given in equation 3.12, $d(^{225}Ra) = -8.5 \times 10^{-17}(\frac{S}{e \cdot fm^3})e \cdot cm$, we can place a limit on the Schiff moment of ^{225}Ra to be $|S(^{225}Ra)| \leq 5.9 \times 10^{-6}$ e fm^3. To constrain the CP violating parameters that make up the Schiff moment, we require estimates of the sensitivity of the Schiff moment to each term, given by

$$S(^{225}Ra) = \alpha_0 g_\pi^0 + \alpha_1 g_\pi^1 + \alpha_2 g_\pi^2 \tag{9.1}$$

We use estimates taken from [36], with $\alpha_0 = -1.5$ e fm^3, $\alpha_1 = 6.0$ e fm^3, and $\alpha_2 = -4.0$ e fm^3. As no current beyond SM theory expects a significant contribution from g_π^2, that term is typically neglected. Even though ^{225}Ra itself is primarily sensitive to CP violation in pion-nucleon couplings, it is noted in Ref. [53] that since the sensitivities to the various terms are coupled, including ^{225}Ra in the existing collection of EDM searches can also help further constrain the pseudotensor electron-nucleon coupling (C_T) and short-range neutron EDM terms ($\bar{d}_n$). A detailed analysis is worked out in Ref. [53]; the results are reproduced here in Figure 9.1.

We see that once a ^{225}Ra measurement has reached the $10^{-25} e\cdot$ cm level, constraints are placed on all four relevant CP violating parameters, most notably on the pseudotensor electron-nucleon coupling. However, our experimental limit right now is $|d(^{225}\text{Ra})| < 5.0 \times 10^{-22}$ e·cm, so it is worth considering the constraints on CP violating parameters

			d_e (e-cm)	C_S	C_T	$\bar{g}_\pi^{(0)}$	$\bar{g}_\pi^{(1)}$	$\bar{d}_n$ (e-cm)
Current Limits (95%)			5.4×10^{-27}	4.5×10^{-7}	2×10^{-6}	8×10^{-9}	1.2×10^{-9}	12×10^{-23}
System	Current (e-cm)	Projected	Projected sensitivity					
ThO	5×10^{-29}	5×10^{-30}	4.0×10^{-27}	3.2×10^{-7}				
Fr		$d_e < 10^{-28}$	2.4×10^{-27}	1.8×10^{-7}				
^{129}Xe	3×10^{-27}	3×10^{-29}			3×10^{-7}	3×10^{-9}	1×10^{-9}	5×10^{-23}
Neutron/Xe	2×10^{-26}	$10^{-28}/3 \times 10^{-29}$			1×10^{-7}	1×10^{-9}	4×10^{-10}	2×10^{-23}
Ra		10^{-25}			5×10^{-8}	4×10^{-9}	1×10^{-9}	6×10^{-23}
Ra		10^{-26}			1×10^{-8}	1×10^{-9}	3×10^{-10}	2×10^{-24}
Neutron/Xe/Ra		$10^{-28}/3 \times 10^{-29}/10^{-27}$			6×10^{-9}	9×10^{-10}	3×10^{-10}	1×10^{-24}

FIGURE 9.1: Table showing how various new EDM measurements could constrain underlying CP violating parameters. Note ^{225}Ra at the $1 \times 10^{-25} e$·cm and $1 \times 10^{-26} e$·cm levels. Taken from [53].

that can be placed with the current measurement; the constraints on the four relevant parameters are plotted in Figure 9.2 as a function of ^{225}Ra EDM sensitivity [54].

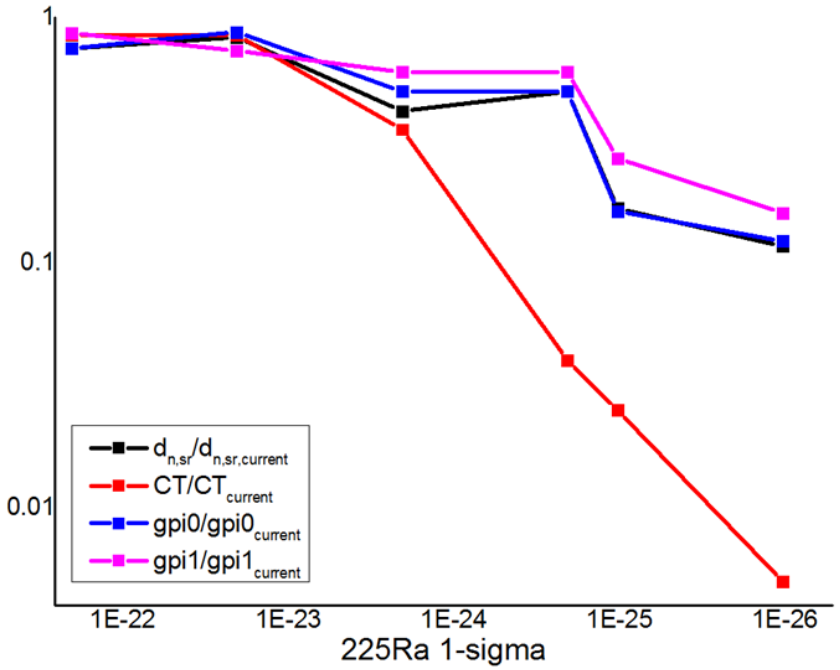

FIGURE 9.2: This plot shows how an EDM measurement with ^{225}Ra would help constrain CP violating parameters, for a range of EDM sensitivities. Significant constraints are made around the $2 \times 10^{-25} e$·cm level. Taken from [54].

From Figure 9.2 we see that a radium EDM measurement begins to significantly constrain the CP violating parameters once the sensitivity of the experiment is improved by at least 2 orders of magnitude. This is to be expected, as the measurement discussed in this thesis represents a proof-of-principle, and there are many avenues forward for improved sensitivity. These options will be discussed in the next chapter.

Chapter 10

Future Upgrades

With the first EDM measurement of ^{225}Ra complete, we consider ways to improve the apparatus. The guiding philosophy of the experiment in the last few years was to get an EDM measurement done as soon as possible (to prove to ourselves that it could be done and gain experience), rather than waiting and trying to do the best EDM measurement that could ever be done. In this chapter we discuss five possible avenues for improvement to the system, potentially improving our EDM sensitivity by many orders of magnitude.

10.1 Spin Precession Time

As shown in Equation 7.1, the EDM sensitivity scales linearly with the precession time in our current regime, and therefore that is a logical place to hunt for improvements. The lifetime in the holding trap depends on the aligment of the retroreflection and the pressure in the science chamber, and was typically 3-4 seconds in the two EDM runs. Typical lifetime data is shown in Figure 10.1. Due to a leak in the vacuum system, the pressure in the science chamber was 3×10^{-10} Torr, more than an order of magnitude worse than the best that been achieved in the science chamber a year prior. Our current experimental approach, in which we take two spin precession images each cycle (one with HV on and one with HV off), means that we are limited to a spin precession time of about 2 seconds.

After the two EDM runs, the leak in the vacuum system was found and fixed, and the glass tube was baked again to remove water. The pressure is currently below 3×10^{-11}

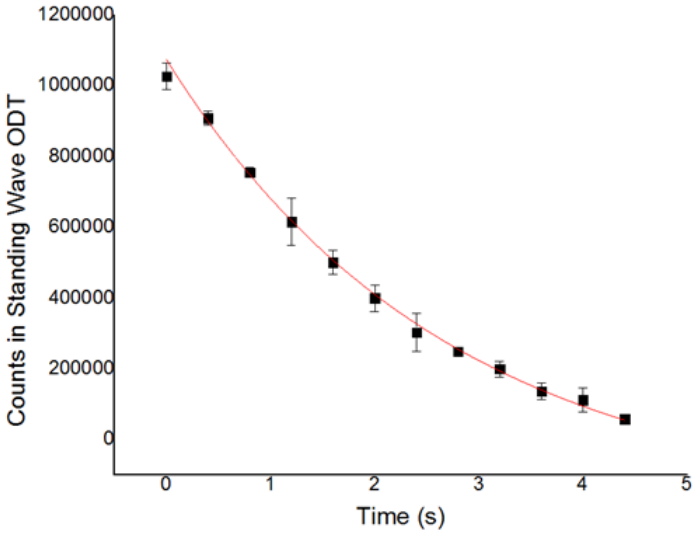

FIGURE 10.1: Lifetime of atoms in the holding ODT, measured with ^{226}Ra. Currently the decay is well-described by a single exponential.

Torr, limited by the sensitivity of our vacuum gauges. If our system is limited by background gas collisions, then we expect this will directly result in an order of magnitude improvement in our holding ODT lifetime, and therefore an order of magnitude improvement in our EDM sensitivity. If our system is limited by another source of noise then that source of noise will have to be identified and suppressed. Pointing noise and phase noise of the ODT can be suppressed by a servo monitoring an interferometer signal comparing the two beams in our holding ODT, and applying feedback as needed to a piezo mounted on the retroreflection mirror. Intensity noise can be suppressed by adding an AOM into the beam path before the vacuum chamber, and using a servo to adjust the RF power in the AOM to compensate for fluctuations in the fiber laser output power.

10.2 Electric Field

The EDM sensitivity is also linear in the applied electric field. In the EDM runs described previously, the electric field was applied for 1.2 seconds, out of a total spin precession time of 2 seconds. The maximum value of the E-field was 67 kV/cm, but averaged over the precession time the effective E-field was 40 kV/cm. The time required for the E-field to be ramped up and down limits the duration for which it can be kept on at its maximum value. As the precession time is increased (see previous section), the ramping

time will become less significant, and the effective E-field will approach the maximum E-field.

The maximum E-field is determined by the voltage difference at which discharges occur, 80 kV/cm for our current pair of electrodes. Any roughness on the electrode surface will provide a point of high electric field, potentially resulting in discharges from that point. Numerous techniques exist to "condition" electrodes so that they may be operated at high voltages without sparking; using copper electrodes groups have been able to demonstrate up to 500 kV/cm without discharges using a plasma glow discharge to condition the electrodes first [55].

10.3 STIRAP Upgrade

Another improvement currently being explored is an improvement to the detection efficiency of our system, using a coherent population transfer technique called STIRAP (Stimulated Raman Adiabatic Passage). Before discussing how this technique will assist in a radium EDM measurement, we first briefly describe some key points about STIRAP. The basic idea of STIRAP is to use two coherent pulses of light to transfer population between two long-lived states. In particular, it uses two lasers coupling three states instead of one laser coupling two states.

In a two-level system, one may use an incoherent light source to transfer up to 50% of the ground state population to the excited state, limited by spontaneous emission. With a coherent light source, one can induce Rabi oscillations that will periodically transfer 100% of the population to the excited state. Alternatively, one can use adiabtic passage (for example, by sweeping slowly across the resonance with the frequency of the laser source) to transfer 100% of the population to the excited state after a few Rabi flops.

In STIRAP one couples three states together in a Λ configuration (see Figure 10.2). A Stokes laser (1429 nm in our case) couples the final state with the middle state, and a Pump laser (483 nm in our case) couples the middle state with the initial state. A full mathematical treatment can be found in [56]. By applying a pulse with the Stokes laser first, then applying a second pulse with the Pump laser, population can be transferred adiabatically from the initial state to the final state, without ever actually occupying the

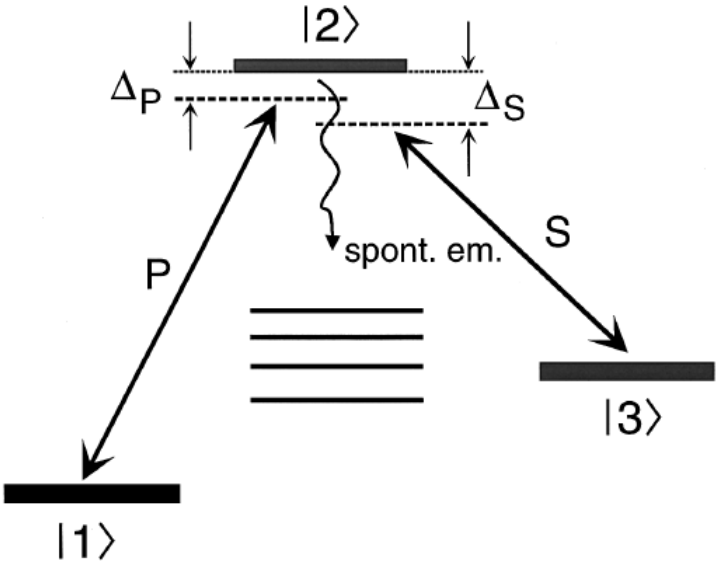

FIGURE 10.2: The common three-level scheme used in STIRAP. Initially only state $|1\rangle$ is populated. In the STIRAP pulse sequence, first states $|3\rangle$ and $|2\rangle$ are coupled with the Stokes laser. Then states $|1\rangle$ and $|2\rangle$ are coupled with the Pump laser. With appropriate choice of experimental parameters the majority of the population can be shelved to state $|3\rangle$. Adapted from [56].

middle state–meaning the atoms will not undergo spontaneous decay from the middle state. The so-called counter-intuitive pulse sequence is shown in Figure 10.3.

To remain in the adiabatic regime, the time required for a Rabi flop, given by the Rabi frequency Ω, should be much smaller than the time Δt needed for the transfer. In practice, it has been found by other groups [56] that a good criterion for efficient STIRAP is

$$\Omega \Delta t > 10 \text{ radians}$$

where the Rabi frequency is given in Hz. The two lasers are not required to be on-resonance with the middle transition, but the lasers are required to be equally detuned from that state to conserve energy. The dependence of the efficiency of the population transfer on the relative detuning Δ between the two lasers is given by [57]:

$$P = e^{\frac{-\Gamma T \Delta^2}{3\Omega^2}}$$

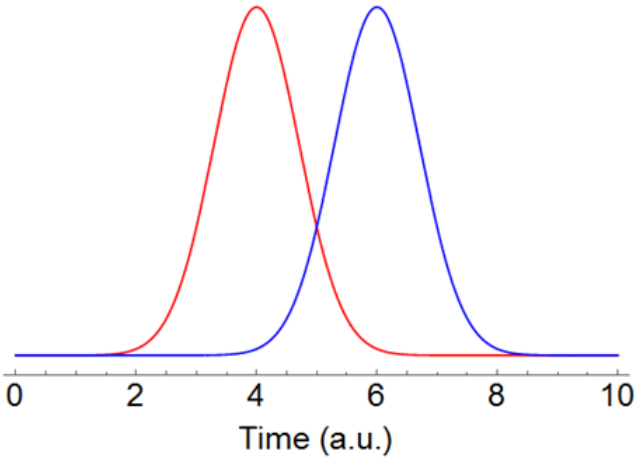

FIGURE 10.3: "Counter-intuitive" pulse sequence used in STIRAP. The red curve is the power in the 1429 nm laser; the blue curve is the power in the 483 nm laser.

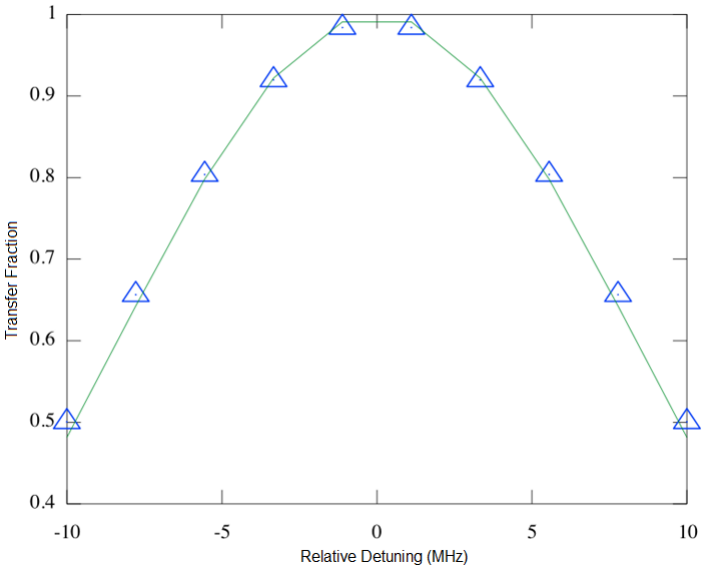

FIGURE 10.4: Sensitivity of the STIRAP technique to relative detuning between the Stokes and Pump lasers. The line is from the analytic solution given in [57]. The triangles are numerical solution to the optical Bloch equation.

where Γ is the 1/lifetime of the excited state. This result implies that STIRAP is a reasonably robust technique, somewhat insensitive to small changes in the relative frequency of the two lasers. The sensitivity of the relative detuning for our system is shown in Figure 10.4.

The key advantage to using STIRAP in our application is the ability to select a specific magnetic sublevel of the ground state, thereby enabling spin-sensitive detection. So for our particular implementation of STIRAP, shown in Figure 10.5, the plan is to transfer population in ^{225}Ra from one of the two magnetic sublevels to the $^3D_1$ state, using the

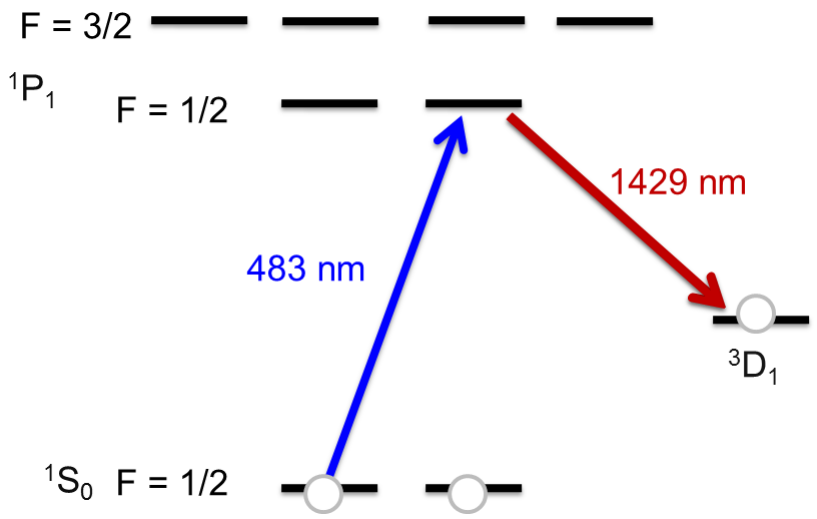

FIGURE 10.5: The plan for STIRAP with ^{225}Ra. Atoms will be shelved from one of the two magnetic sublevels to the $^3D_1$ state, without actually populating the $F = 1/2$ $^1P_1$ state.

$F = 1/2$ $^1P_1$ state as an intermediary. Once accomplished, we can apply circularly polarized light on the $F = 1/2 \rightarrow F = 3/2$ transition for spin-sensitive detection. This transition will scatter about 1000 photons before the atoms decay to metastable states. This is a dramatic increase in the number of scattered photons per atom (up from 2-3 using the current scheme). We recall how our EDM sensitivity scales with the number of scattered photons per atom M:

$$\Delta d = \frac{\hbar\sqrt{2}}{4E\tau}\sqrt{\frac{5\bar{P}_L}{4M^2N^2} + \frac{1}{4N}}\sqrt{\frac{\tau + T_d}{T}} \tag{10.1}$$

To take full advantage of the factor-of-300 gain in scattered photons per atom, we will also need to increase the number of photons in the background by the same factor, because we will now need to expose the probe beam for longer (or equivaltenly, use a higher-intensity probe beam). This results in an overall improvement in EDM sensitivity of about $\sqrt{300} = 17$. After the upgrade, we expect to be limited by atom shot noise, simplifying our EDM sensitivity formula to

$$\Delta d = \frac{\hbar}{4E\tau}\sqrt{\frac{1}{2N}}\sqrt{\frac{\tau + T_d}{T}} \tag{10.2}$$

10.4 Blue Upgrade

As mentioned earlier, the 483 nm transition is stronger than the 714 nm transition, but leaks to many of the D-states, and therefore it was decided not to attempt a preliminary EDM measurement with a Zeeman slower or transverse cooling on the 483 nm transition. With the first EDM measurement complete, we now consider the potential gain from using a slower on the blue transition. The flux of atoms out of the oven at a particular velocity is given by

$$n(v) = \int_{v=0}^{V_{cap}} \frac{v^3}{2(\bar{v}/2)^4} exp(\frac{-v^2}{2 \cdot (\bar{v}/2)^2}) dv$$

$$\bar{v} = 2\sqrt{k_B T/m}$$

For the 714 nm transition with a 1 meter Zeeman slower the capture velocity V_{cap} is expected to be about 60 m/s, whereas for the 483 nm transition with a 20 cm Zeemen slower it is expected to be about 300 m/s. By intergrating the velocity distribution at these two capture velocities, we see that we can potentially capture two orders of magnitude more atoms using the 483 nm transition. The blue slower can be added upstream to the current red slower, and it can be designed such that its output velocity is not 0 m/s but about 60 m/s, so that atoms can be captured and further slowed by the existing red slower. In this way, there will be a 3D MOT even if the blue slower is not optimized, so the experimenters can tune to increase a non-zero MOT, rather than searching blindly without a signal.

The technical challenge to this comes from the number of repump lasers required, and the requirement that atoms be pumped out of these states before they are lost by the Zeeman slower (by no longer being in resonance with the 483 nm laser by the time they return to the ground state). Lasers will need to pump atoms out of $^1D_2$, $^3D_2$, and $^3D_1$. As the g-factors for the various states are different, the repump lasers will in general not all be resonant with the atoms as they experience the spatially-dependent magnetic field. It is therefore expected that the repump lasers will need to be chirped in order to guarantee they are on-resonance with the atoms during the deceleration.

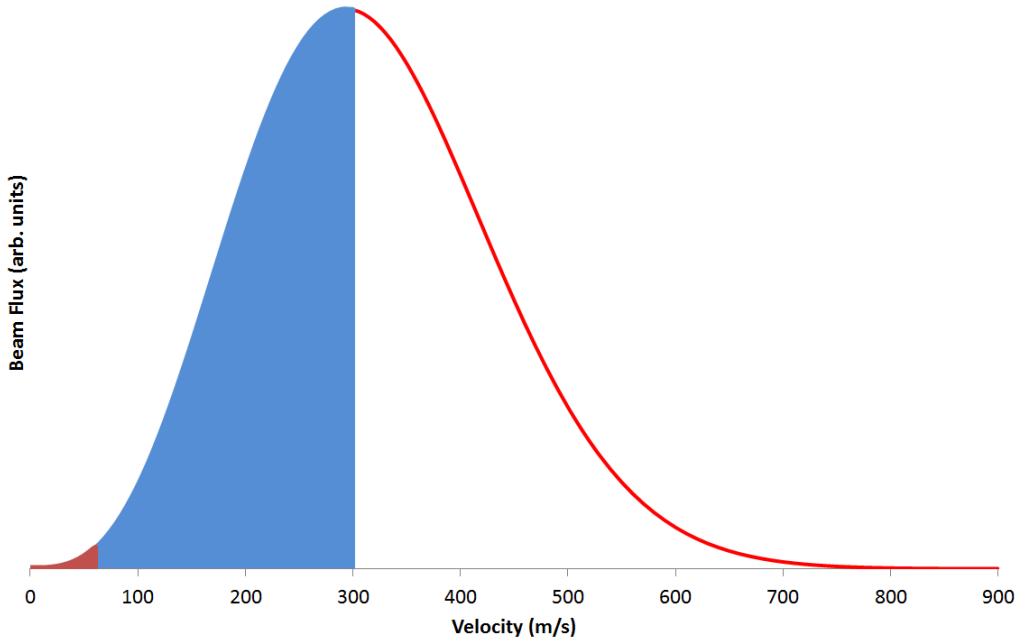

FIGURE 10.6: Predicted thermal distribution of velocities out of the oven, for 500 degrees C. The purple shaded area indicates what we can expect to capture using the 714 nm transition; the blue represents what we expect to capture with the 483 nm transition.

10.5 ^{225}Ra Source Upgrade

The amount of ^{225}Ra loaded into our system is currently limited simply by the conservative desire to gradually increase the loaded activity each run, rather than dramatically increase the loaded activity. It is expected that after a few years of operating with the algorithm, we will eventually be limited by the amount of ^{225}Ra that Oakridge National Laboratory can provide. The flux of atoms out of our oven depends on ovem temperature, oven age, and loaded activity, but is typically at the level of 10^8 atoms per second.

Stronger sources of ^{225}Ra are under development at various nuclear physics accelerator facilities, including the Facility for Rare Isotope Beams [58]. For example, it has been calculated that spallation of a thorium target induced by a 1 mA beam of deuterons at 1 GeV will yield ^{225}Ra at the rate of 10^{13} s^{-1} [59], which is 5 orders of magnitude stronger than the currently available supply. This would be an enormous improvement in the EDM sensitivity of the experiment.

Appendix A

2D Focusing Simulation

```
%2D-MOT Simulation (in 1D)

close all
clear all
clc
figure
hold on

%All in SI units
% for j=1:1:4

for i=-.0254:.001:.0254
InitialPos = i;
InitialVel = 0;
Gamma =  1/(420*10^-9);
snumber = 5;
hbar = 1.05*10^-34;
k = 1/(714*10^-9);
delta = -1/(420*10^-9);      %Negative is to the red
Bgrad = -.3;                 %This is in G/cm, negative is trapping
Bgrada = Bgrad;
Bgrad = Bgrad*1/10000*100;   %This is in T/m
```

```
g = 1.5;
mf = 1;
mu = g*mf*9.27*10^-24;
m = 226*1.66*10^-27;
Vparallel = 60;
FocalLength = 1.3;
Length2DMOT = 2*.0254;
Time2DMOT = Length2DMOT/Vparallel;
Time3DMOT = FocalLength/Vparallel;

Initial = [InitialPos InitialVel Gamma snumber hbar k delta Bgrad mu m Time2DMOT];

[time,xdot] = ode45(@scattering,0:.0001:Time3DMOT,Initial);

pos = xdot(:,1);
vel = xdot(:,2);

% subplot(4,1,j)
plot(time,pos,'b-')
xlabel('Time (s)')
ylabel('Transverse Position')
title(['Bgrad (G/cm) = ' num2str(-Bgrada)])
% subplot(2,1,2)
% plot(time,vel,'b-')
% plot(time,pos,'b-',time,vel,'r.')

end

% end
hold off

This is a separate file:

function xdot = scattering(t,x)
```

```
Gamma = x(3);

snumber = x(4);

hbar = x(5);

k = x(6);

delta = x(7);

Bgrad = x(8);

mu = x(9);

m = x(10);

Time2DMOT = x(11);


if t<Time2DMOT

xdot = [x(2) ; hbar*k*Gamma/(2*m)*(snumber/(1+snumber+4/Gamma^2*

(delta-k*x(2)+mu*Bgrad*x(1)/hbar)^2)-snumber/(1+snumber+4/Gamma^2*

(delta+k*x(2)-mu*Bgrad*x(1)/hbar)^2)) ; 0 ; 0 ; 0 ; 0 ; 0 ; 0 ; 0 ; 0];

else

xdot = [x(2) ; 0 ; 0 ; 0 ; 0 ; 0 ; 0 ; 0 ; 0 ; 0];


end

%x(1) is position

%x(2) is velocity


%First row of xdot is vel, second row is accel
```

Appendix B

ODT Transport Simulation

```
This code is written in Python. The first version of this code was written by Ibrahim

import numpy as np;
import pylab as plt;
import pickle;

pi = np.pi
amu = 1.66*10**(-27);
uK = 10**(-6);
x0 = 0; #trap initial pos
v0 = 0; #trap initial vel
a0 = 0; #trap initial accel
zR = 5; # Rayleigh length in mm (the radius, not the diameter),
for (maybe) 100um waist diameter
U0 = 400*uK   # Depth of trap micro kelvin
Temp = 40;    #Temperature in micro Kelvin
m = 226*amu
kb = 1.38*10**(-23)
Npos = 50;  #Number of atoms sampled for each velocity
freq = 1/(2*pi)*np.sqrt((2*kb*U0)/(m*(.001*zR)**2)) #Trap Frequency for
a given U0 and zR.
omega = 2*pi*freq;
```

```
tau = 100;   # Timestep of 1/tau second
wd = np.sqrt(1*kb*Temp/(2*m*omega*omega));
wv = 1000*np.sqrt(Temp*1E-6*kb/m);  #width in velocity spread for atoms of a
particular temperature
vinitial = 10; #lowest velocity to simulate in mm/s
vfin = 225;  #Maximum velocity in simulation in mm/s
steps = 50; #number of velocities you want to plot
ts = vfin/steps;
velset = range(vinitial,int(vfin),int(ts)) #Creating an array of velocities
Cond = 300/100; #Condition for being bound, max dist from trap center at any
time during trip, in mm
noise = 1000000000; #larger means less noise (noise is xM/noise)
Amp = 225/noise;
Errorbars = 0; #0=no, 1=yes

##def getU(xg):
##    #return kb*1E6*U0*np.exp(-0.5*((xg-x0)/zR)**2)
##    #return kb*1E6*U0*1/(1+(xg/zR)**2)
##    if xg<-8.43875:
##        return 0
##    elif xg>8.43875:
##        return 0
##    else:
##        return kb*1E6*U0*(2*(10**(-4))*(xg**4-xg**2)-1)

def getF(xg):
    #One Power of 1E3 to convert from mm t0 m in (x/zR^2). One Power
    #1E3 to convert force to kg*mm/s^2
    return -2*kb*1E3*1E3*U0*((xg-x0)/(zR*zR))/((1+((xg-x0)/zR)**2)**2)
##    if xg-x0<-8.43875:
##        return 0
##    elif xg-x0>8.43875:
##        return 0
##    else:
```

```
##        return -kb*1E6*U0*(.0008*(xg-x0)**3-.0004*(xg-x0))

def rk4(x, v, a, dt):
#Returns final (position, velocity) tuple after
#time dt has passed.

    #x: initial position (number-like object)
#v: initial velocity (number-like object)
#a: acceleration function a(x,v,dt) (must be callable)
#dt: timestep (number)"""
x1 = x
v1 = v
a1 = a(x1, x0, v1, 0)

x2 = x + 0.5*v1*dt
v2 = v + 0.5*a1*dt
a2 = a(x2, x0, v2, dt/2.0)

x3 = x + 0.5*v2*dt
v3 = v + 0.5*a2*dt
a3 = a(x3, x0, v3, dt/2.0)

x4 = x + v3*dt
v4 = v + a3*dt
a4 = a(x4, x0, v4, dt)

xf = x + (dt/6.0)*(v1 + 2*v2 + 2*v3 + v4)
vf = v + (dt/6.0)*(a1 + 2*a2 + 2*a3 + a4)

return xf, vf

def accel(x, x0, v, dt):
    #Determines acceleration from current position,
    #velocity, and timestep. This particular acceleration
```

```
    #function models a spring. X0 is the position of the trap center
    #cast to reproduce 5Hz.
    return getF(x)/m

################## MAIN  PROGRAM ###################

xind = 150; #Trip distance
MeanData = [];
ErrData = [];
Ptrap=[];
stateRec = [];
Ptrap_TravelTime = [];
for vel in velset:
    xM = xind;   #Maximum Displacement
    TRun = 2*xM/vel; #Time of motion  (round trip)
    Ptrap_TravelTime.append(TRun/2);
    ftrap = 0.5/TRun;
    t = 0
    dt = 1.0/tau # Timestep of 1/tau second
    bstate = 0;
    for ij in range(1,Npos):
        pos = np.random.normal(loc = 0, scale = wd)  #Drawing from a normal
distribution with width wd
        vstate = np.random.normal(loc = 0, scale = wv) #Drawing from a normal
distribution with width wv
        state = pos, vstate # Position, velocity
        stateRec.append(vstate);
        print("Initial    -position: %6.2f, velocity: %6.2f" %state)
        Ptrap=[];
        data = [];
        Data2 = [];
        nStep = 2;
        for ik in range(1,nStep):
            trSiz = 0
```

```
            t = 0;
            TR = []
            PR = []
            PRv = [];
            PRa = [];
            while t < TRun:

                #  Profile 1
                #x0 = xM*np.sin(2*pi*ftrap*t);
##                v0 = xM*2*pi*ftrap*np.cos(2*pi*ftrap*t);
##                a0 = -xM*2*pi*ftrap*2*pi*ftrap*np.sin(2*pi*ftrap*t);
##                PR.append(x0);
##                PRv.append(v0);
##                PRa.append(a0);
                # Profile 2

                #x0 = (xM*np.sin(4.0*pi*ftrap*t - pi/2) + xM)/2.0;
                x0 = (xM*np.sin(4.0*pi*ftrap*t - pi/2) + xM +
0*np.random.normal(loc = 0, scale=xM/noise))
                #v0 = (xM*4.0*pi*ftrap*np.sin(4.0*pi*ftrap*t))/2.0;
                #a0 = (xM*4.0*pi*ftrap*4.0*pi*ftrap*np.cos(4.0*pi*ftrap*t))/2.0;
                #v0 = (PR[int(tau*t)]-PR[int(tau*t-1)])/dt;
                #a0 =(PR[int(tau*t)]-2*PR[int(tau*t-1)]+PR[int(tau*t-2)])/dt**2;
                PR.append(x0);
                #PRv.append(v0);
                #PRa.append(a0);
                t += dt;
                state = rk4(state[0], state[1], accel, dt);
                Data2.append(state)
                tr = np.abs(state[0] - x0);
                if tr > trSiz:
                    trSiz = (state[0] - x0);
                TR.append(tr)
        Ptrap.append(xM*2/TRun);
```

```
        data.append(trSiz);
        TR = np.transpose(np.array(TR))
        if np.max(TR)<Cond:   #Condition for being bound, in mm
            bstate = bstate + 1; #update the number of bound states
    for il in range(0, nStep-1):
        MeanData.append(np.sqrt(bstate/(Npos-1)));
        ErrData.append(Errorbars*0.2/np.sqrt(bstate));
    sz = np.size(np.transpose(Data2)[0]);
    tm = np.linspace(0,TRun,sz)
MeanData150 = MeanData;
ErrData150 = ErrData;
Ptrap_TravelTime150 = Ptrap_TravelTime;

##########################################################

xind = 225; #Trip distance
MeanData = [];
ErrData = [];
Ptrap=[];
stateRec = [];
Ptrap_TravelTime = [];
for vel in velset:
    xM = xind;   #Maximum Displacement
    TRun = 2*xM/vel; #Time of motion  (round trip)
    Ptrap_TravelTime.append(TRun/2);
    ftrap = 0.5/TRun;
    t = 0
    dt = 1.0/tau # Timestep of 1/tau second
    bstate = 0;
    for ij in range(1,Npos):
        pos = np.random.normal(loc = 0, scale = wd)  #Drawing from a normal
distribution with width wd
        vstate = np.random.normal(loc = 0, scale = wv) #Drawing from a normal
distribution with width wv
```

```
        state = pos, vstate # Position, velocity
        stateRec.append(vstate);
        print("Initial    -position: %6.2f, velocity: %6.2f" %state)
        Ptrap=[];
        data = [];
        Data2 = [];
        nStep = 2;
        for ik in range(1,nStep):
            trSiz = 0
            t = 0;
            TR = []
            PR = []
            while t < TRun:
                #x0 = (xM*np.sin(4.0*pi*ftrap*t - pi/2) + xM)/2.0;
                x0 = (xM*np.sin(4.0*pi*ftrap*t - pi/2) + xM +
0*np.random.normal(loc = 0, scale=xM/noise))
                PR.append(x0)
                t += dt;
                state = rk4(state[0], state[1], accel, dt);
                Data2.append(state)
                tr = np.abs(state[0] - x0);
                if tr > trSiz:
                    trSiz = (state[0] - x0);
                TR.append(tr)
        Ptrap.append(xM*2/TRun);
        data.append(trSiz);
        TR = np.transpose(np.array(TR))
        if np.max(TR)<Cond:   #Condition for being bound
            bstate = bstate + 1; #update the number of bound states
    for il in range(0, nStep-1):
        MeanData.append(np.sqrt(bstate/(Npos-1)));
        ErrData.append(Errorbars*0.2/np.sqrt(bstate));
    sz = np.size(np.transpose(Data2)[0]);
    tm = np.linspace(0,TRun,sz)
```

```
MeanData225 = MeanData;
ErrData225 = ErrData;
Ptrap_TravelTime225 = Ptrap_TravelTime;

########################################################

xind = 300; #Trip distance
MeanData = [];
ErrData = [];
Ptrap=[];
stateRec = [];
Ptrap_TravelTime=[];
for vel in velset:
    xM = xind;   #Maximum Displacement
    TRun = 2*xM/vel; #Time of motion  (round trip)
    Ptrap_TravelTime.append(TRun/2);
    ftrap = 0.5/TRun;
    t = 0
    dt = 1.0/tau # Timestep of 1/tau second
    bstate = 0;
    for ij in range(1,Npos):
        pos = np.random.normal(loc = 0, scale = wd)  #Drawing from a normal
distribution with width wd
        vstate = np.random.normal(loc = 0, scale = wv) #Drawing from a normal
distribution with width wv
        state = pos, vstate # Position, velocity
        stateRec.append(vstate);
        print("Initial    -position: %6.2f, velocity: %6.2f" %state)
        Ptrap=[];
        data = [];
        Data2 = [];
        nStep = 2;
        for ik in range(1,nStep):
            trSiz = 0
```

```
            t = 0;
            TR = []
            PR = []
            while t < TRun:
                #x0 = xM*np.sin(2*pi*ftrap*t);
                #x0 = (xM*np.sin(4.0*pi*ftrap*t - pi/2) + xM)/2.0;
                x0 = (xM*np.sin(4.0*pi*ftrap*t - pi/2) + xM +
0*np.random.normal(loc = 0, scale=xM/noise))
                PR.append(x0)
                t += dt;
                state = rk4(state[0], state[1], accel, dt);
                Data2.append(state)
                tr = np.abs(state[0] - x0);
                if tr > trSiz:
                    trSiz = (state[0] - x0);
                TR.append(tr)
        Ptrap.append(xM*2/TRun);
        data.append(trSiz);
        TR = np.transpose(np.array(TR))
        if np.max(TR)<Cond:   #Condition for being bound
            bstate = bstate + 1; #update the number of bound states
    for il in range(0, nStep-1):
        MeanData.append(np.sqrt(bstate/(Npos-1)));
        ErrData.append(Errorbars*0.2/np.sqrt(bstate));
    sz = np.size(np.transpose(Data2)[0]);
    tm = np.linspace(0,TRun,sz)
MeanData300 = MeanData;
ErrData300 = ErrData;
Ptrap_TravelTime300 = Ptrap_TravelTime;

Vmax = np.multiply(3.14/2,velset);
#Amax=D/2*(pi/(D/Vavg))^2; Conversion formula
Ptrap = velset;
Ptrap150 = 2*np.square(Vmax)/150000;
```

```
Ptrap225 = 2*np.square(Vmax)/225000;
Ptrap300 = 2*np.square(Vmax)/300000;

from pylab import *
subplot(211)
plt.errorbar(Ptrap150, MeanData150, ErrData150,fmt = 'ks');
plt.errorbar(Ptrap225, MeanData225, ErrData225,fmt = 'ro');
plt.errorbar(Ptrap300, MeanData300, ErrData300,fmt = 'b^');
plt.grid(False)
capt = 'Round-trip survival fraction'
plt.title(capt)
plt.axis([0,Ptrap150[-1]+.05,0,1.1])
plt.xlabel('Maximum Acceleration (m/s2)')
plt.ylabel('Bound Fraction')

subplot(212)
plt.errorbar(Ptrap, MeanData150, ErrData150,fmt = 'ks');
plt.errorbar(Ptrap, MeanData225, ErrData225,fmt = 'ro');
plt.errorbar(Ptrap, MeanData300, ErrData300,fmt = 'b^');
plt.grid(False)
capt = 'Round-trip survival fraction'
plt.title(capt)
plt.axis([vinitial-10,vfin+10,0,1.2])
plt.xlabel('Average Velocity (mm/s)')
plt.ylabel('Bound Fraction')
plt.show()

plt.figure
plt.errorbar(Ptrap_TravelTime150, MeanData150, ErrData150,fmt = 'ks');
plt.errorbar(Ptrap_TravelTime225, MeanData225, ErrData225,fmt = 'ro');
plt.errorbar(Ptrap_TravelTime300, MeanData300, ErrData300,fmt = 'b^');
plt.grid(False)
capt = 'Round-trip survival fraction'
plt.title(capt)
```

```
plt.axis([0,16,0,1])
plt.xlabel('Transport Time (s)')
plt.ylabel('Bound Fraction')
plt.show()

##plt.plot(tm, PR, 'r-')
##plt.plot(tm, PRv, 'b-')
##plt.plot(tm, PRa, 'g-')
###capt = 'Red=x, Blue=v, Green=a
Original Profile, with large begin/end spikes'
##plt.title(capt)
```

Appendix C

Rate Equation Model

This code is written in Mathematica.

```
(*State Labels:
 1 = 1S0;
2 = 3P0;
3 = 3D1;
4 = 3D2;
5 = 3P1;
6 = 3D3;
7 = 3P2;
8 = 1D2;
9 = 1P1;
*)

BBR = 1;
sP1 = 0*.05*1;
tP1 = 20;
repump = 0;
red = 0;
ODT = 0;
MMWAVE = 0;
```

```
A19 = 1.793*10^8*sP1/(1 + sP1);

A15 = 2.374*10^6*tP1/(1 + tP1);

A39 = 3.282*10^4*repump/(1 + repump) + 5*ODT;

A14 = .25*red;

A21 = 2.935*10^-2;

A51 = 2.374*10^6;

A52 = 1.334*10^-2;

A53 = 8.794*10^1 + 29.63*BBR;

A35 = 29.63*BBR;

A54 = 1.775*10^-3 + .11*BBR;

A45 = .04*BBR + MMWavePumpRate*MMWAVE;

A49 = 68.6*ODT;

A72 = 1.185*10^-2;

A73 = 4.310*10^3;

A74 = 4.602*10^4 + .09*BBR;

A47 = .09*BBR;

A76 = 1.044*10^5 + 9.59*BBR;

A67 = 4.89*BBR;

A91 = 1.793*10^8;

A93 = 3.282*10^4;

A94 = 9.793*10^4;

A98 = 3.241*10^5;

A32 = 1.390*10^3 + 21.89*BBR;

A23 = 196.98*BBR;

A41 = 2.524*10^-1*(1 + red);

A42 = 3.021*10^-13;

A43 = 5.082*10^-4;

A64 = 6.352*10^-3 + .7*ODT;

A63 = .05*ODT;

A81 = 2.710*10^1;

A85 = 6.960*10^2;

A87 = 5.930 + 1.03*BBR;

A78 = 1.03*BBR;
```

```
eq1 = N1[t] + N2[t] + N3[t] + N4[t] + N5[t] + N6[t] + N7[t] + N8[t] +
    N9[t] == 1;
eq2 = D[N2[t], t] ==
   A52*N5[t] + A72*N7[t] + A32*N3[t] + A42*N4[t] - (A21 + A23)*N2[t];
eq3 = D[N3[t], t] ==
   A53*N5[t] + A73*N7[t] + A93*N9[t] + A23*N2[t] + A43*N4[t] +
    A63*N6[t] - (A39 + A32 + A35) N3[t];
eq4 = D[N4[t], t] ==
   A14 *N1[t] + A54*N5[t] + A74*N7[t] + A94*N9[t] +
    A64*N6[t] - (A41 + A42 + A43 + A45 + A47 + A49) N4[t];
eq5 = D[N5[t], t] ==
   A15 *N1[t] + A85*N8[t] + A35*N3[t] +
    A45*N4[t] - (A51 + A52 + A53 + A54) N5[t] - A15*N5[t] -
    A85*N5[t] - A35*N5[t] - A45*N5[t];
eq6 = D[N6[t], t] == A76 *N7[t] - (A64 + A67 + A63)*N6[t];
eq7 = D[N7[t], t] ==
   A87* N8[t] + A47*N4[t] +
    A67*N6[t] - (A72 + A73 + A74 + A76 + A78)* N7[t];
eq8 = D[N8[t], t] == A98*N9[t] + A78*N7[t] - (A81 + A85 + A87)*N8[t];
eq9 = D[N9[t], t] ==
   A19*N1[t] + A39*N3[t] + A49*N4[t] - (A91 + A93 + A94 + A98)*N9[t] -
     A19*N9[t] - A39*N9[t] - A49*N9[t];
sol = NDSolve[{eq1, eq2, eq3, eq4, eq5, eq6, eq7, eq8, eq9,
    N1[0] == 1, N2[0] == 0; N3[0] == 0, N4[0] == 0, N5[0] == 0,
    N6[0] == 0, N7[0] == 0, N8[0] == 0, N9[0] == 0}, {N1[t], N2[t],
    N3[t], N4[t], N5[t], N6[t], N7[t], N8[t], N9[t]}, {t, 10^-10,
    100}];
LogLogPlot[{N1[t] /. sol, N2[t] /. sol, N3[t] /. sol, N4[t] /. sol,
  N5[t] /. sol, N6[t] /. sol, N8[t] /. sol, N9[t] /. sol}, {t, 10^-9,
  1}, Axes -> False, Frame -> True, PlotRange -> {.000001, 1.1},
 PlotStyle -> {Red, Cyan, Blue, Green, Purple, Black, Orange, Pink},
 PlotLegends -> {"1S0", "3P0", "3D1", "3D2", "3P1", "3D3", "1D2",
   "1P1"}]
```

Appendix D

Stark Interference

This code is written in Matlab.

```
clear all
clc
%Stark Interference

hbar = 1.05E-34; %SI
mub = 9.27E-24; %SI
lambda = 1550E-9; %SI
c = 3E8; %SI
freq = c/lambda;
F = 1/2;
omega = (2*3.14*freq);
Es = 100*1000*100; %Static E-field in V/m
Eo = 42.6*1000*100; %ODT E-field (according to Matt's notes)
Eo = 1.3857e+06; %ODT E-field (according to Matt's function)
v1vector = [];
v2vector = [];
omega714 = 2*3.14*c/(714E-9);
steps = 20;
omegavector = 0:omega714/steps:omega714;
```

```
for omega = 0:omega714/steps:omega714

v1 = 0;

mF = 1/2;
ns = -1;
nb = 0;
nepsilon = -1;
shift = deltaE(F,mF,ns,nb,nepsilon,omega,Es,Eo);
v1 = v1-1/2*shift;

mF = 1/2;
ns = 1;
nb = 0;
nepsilon = 1;
shift = deltaE(F,mF,ns,nb,nepsilon,omega,Es,Eo);
v1 = v1-1/2*shift;

mF = 1/2;
ns = -1;
nb = 0;
nepsilon = 1;
shift = deltaE(F,mF,ns,nb,nepsilon,omega,Es,Eo);
v1 = v1+1/2*shift;

mF = 1/2;
ns = 1;
nb = 0;
nepsilon = -1;
shift = deltaE(F,mF,ns,nb,nepsilon,omega,Es,Eo);
v1 = v1+1/2*shift;

mF = -1/2;
```

```
ns = -1;
nb = 0;
nepsilon = -1;
shift = deltaE(F,mF,ns,nb,nepsilon,omega,Es,Eo);
v1 = v1+1/2*shift;

mF = -1/2;
ns = 1;
nb = 0;
nepsilon = 1;
shift = deltaE(F,mF,ns,nb,nepsilon,omega,Es,Eo);
v1 = v1+1/2*shift;

mF = -1/2;
ns = -1;
nb = 0;
nepsilon = 1;
shift = deltaE(F,mF,ns,nb,nepsilon,omega,Es,Eo);
v1 = v1-1/2*shift;

mF = -1/2;
ns = 1;
nb = 0;
nepsilon = -1;
shift = deltaE(F,mF,ns,nb,nepsilon,omega,Es,Eo);
v1 = v1-1/2*shift;

v1vector(end+1) = v1;

end



for omega = 0:omega714/steps:omega714
```

```
v2 = 0;

mF = 1/2;
ns = 0;
nb = -1;
nepsilon = -1;
shift = deltaE(F,mF,ns,nb,nepsilon,omega,Es,Eo);
v2 = v2+1/2*shift;

mF = 1/2;
ns = 0;
nb = 1;
nepsilon = 1;
shift = deltaE(F,mF,ns,nb,nepsilon,omega,Es,Eo);
v2 = v2+1/2*shift;

mF = 1/2;
ns = 0;
nb = -1;
nepsilon = 1;
shift = deltaE(F,mF,ns,nb,nepsilon,omega,Es,Eo);
v2 = v2-1/2*shift;

mF = 1/2;
ns = 0;
nb = 1;
nepsilon = -1;
shift = deltaE(F,mF,ns,nb,nepsilon,omega,Es,Eo);
v2 = v2-1/2*shift;

mF = -1/2;
ns = 0;
nb = -1;
```

```
nepsilon = -1;
shift = deltaE(F,mF,ns,nb,nepsilon,omega,Es,Eo);
v2 = v2-1/2*shift;

mF = -1/2;
ns = 0;
nb = 1;
nepsilon = 1;
shift = deltaE(F,mF,ns,nb,nepsilon,omega,Es,Eo);
v2 = v2-1/2*shift;

mF = -1/2;
ns = 0;
nb = -1;
nepsilon = 1;
shift = deltaE(F,mF,ns,nb,nepsilon,omega,Es,Eo);
v2 = v2+1/2*shift;

mF = -1/2;
ns = 0;
nb = 1;
nepsilon = -1;
shift = deltaE(F,mF,ns,nb,nepsilon,omega,Es,Eo);
v2 = v2+1/2*shift;

v2vector(end+1) = v2;

end

v1vector; %In Joules
h = 2*3.14*hbar;
v1vectorHz = v1vector./h; %In Hz
v2vectorHz = v2vector./h; %In Hz
```

```
C=1.6*10^-19;
Sup = 1E-3;
fakeEDM1 = Sup*2*pi*hbar*v1vectorHz/(Es/100*C); %In ecm
fakeEDM2 = Sup*2*pi*hbar*v2vectorHz/(Es/100*C); %In ecm
convert = Sup*2*pi*hbar/(Es/100*C);

figure
hold on
% plot(omegavector./omega714,v1vectorHz,'k-')
% plot(omegavector./omega714,v2vectorHz,'k--')
plot(omegavector./omega714,fakeEDM1,'k-')
plot(omegavector./omega714,fakeEDM2,'k--')
hold off
legend('v1','v2')
xlabel('ODT Frequency Relative to 714nm')
ylabel('Fake EDM (ecm)')
axis([0 1 -.0003*convert .00003*convert])
% axis([0 1 -.001 .001])




function energyshift = deltaE(F,mF,ns,nb,nepsilon,omega,Es,Eo)

hbar = 1.05E-34; %SI
mub = 9.27E-24; %SI
c = 3E8; %SI
lambda3P1 = 714E-9; %SI
lambda1P1 = 483E-9;
omegavector = [2*10357.7927 13999.759 2*10357.8618 13999.269]; %in cm^-1 This
% is the correct one

center226 = 2*10357.801;
center1P1 = center226+2.236E9./(30E9);
```

```
atwo = 2.7965e9; %hyperfine constant in Hz
%30E9Hz is 1cm^-1
katwo = atwo./(30E9); %in cm^-1

% omegavector = [center1P1-katwo 13999.759 center1P1+3/2*katwo 13999.269]; %in cm^-1
% omegavector = [center1P1+2/2*katwo 13999.759 center1P1-3/2*katwo 13999.269]; %in cm

% omegavector = 1./(100*omegavector); %in m
omegavector = 2*pi*c*100*omegavector; %in radian-Hz
prefactor = (mub*Es*Eo^2)/(4*c*hbar^2);
innersum = 0;



for S = [0 1]
for Fprime = [1/2 3/2];
for Fprimeprime = [1/2 3/2];

if Fprime == 1/2
    mFprimevec = [1/2 -1/2];
elseif Fprime == 3/2
    mFprimevec = [3/2 1/2 -1/2 -3/2];
end

if Fprimeprime == 1/2
    mFprimeprimevec = [1/2 -1/2];
elseif Fprimeprime == 3/2
    mFprimeprimevec = [3/2 1/2 -1/2 -3/2];
end

for mFprime = mFprimevec;

for mFprimeprime = mFprimeprimevec;
```

```
%Four possible omegaFprime's--two Fprimes, two S's
if Fprime==1/2 && S==0
    omegaFprime = omegavector(1);
%     omegaFprime =  2*pi*c*100*(center1P1+katwo*(Fprime*(Fprime+1)-11/4)/2);
elseif Fprime==1/2 && S==1
    omegaFprime = omegavector(2);
elseif Fprime==3/2 && S==0
    omegaFprime = omegavector(3);
%     omegaFprime =  2*pi*c*100*(center1P1+katwo*(Fprime*(Fprime+1)-11/4)/2);
elseif Fprime==3/2 && S==1
    omegaFprime = omegavector(4);
end

if Fprimeprime==1/2 && S==0
    omegaFprimeprime = omegavector(1);
%     omegaFprimeprime =  2*pi*c*100*(center1P1+katwo*(Fprimeprime*(Fprimeprime+1)-11
elseif Fprimeprime==1/2 && S==1
    omegaFprimeprime = omegavector(2);
elseif Fprimeprime==3/2 && S==0
    omegaFprimeprime = omegavector(3);
%     omegaFprimeprime =  2*pi*c*100*(center1P1+katwo*(Fprimeprime*(Fprimeprime+1)-11
elseif Fprimeprime==3/2 && S==1
    omegaFprimeprime = omegavector(4);
end

g = G(F,mF,Fprime,mFprime,Fprimeprime,mFprimeprime,-nepsilon,nb,ns,S);
newpiece1 = ((-1)^(nepsilon)*g)/((omegaFprime - omega)*(omegaFprimeprime - omega));
g = G(F,mF,Fprime,mFprime,Fprimeprime,mFprimeprime,nepsilon,-nb,ns,S);
newpiece2 = ((-1)^(nb)*g)/((omegaFprime + omega)*(omegaFprimeprime + omega));
g = G(F,mF,Fprime,mFprime,Fprimeprime,mFprimeprime,ns,-nb,nepsilon,S);
newpiece3 = ((-1)^(nb)*g)/((omegaFprime - omega)*(omegaFprimeprime - omega));
g = G(F,mF,Fprime,mFprime,Fprimeprime,mFprimeprime,ns,nb,-nepsilon,S);
newpiece4 = ((-1)^(nepsilon)*g)/((omegaFprime + omega)*(omegaFprimeprime + omega));
```

```
newpiece = newpiece1 + newpiece2 + newpiece3 + newpiece4;
innersum = innersum + newpiece;

end
end
end
end
end


energyshift = prefactor*innersum;




function g = G(F,mF,Fprime,mFprime,Fprimeprime,mFprimeprime,n1,nb,n2,S)

conv = 8.5E-30; %Coulomb meter
singletreducedmattrixelement = 5.504; %in a.u.
tripletreducedmattrixelement = 1.218; %in a.u.
singletreducedmattrixelement = singletreducedmattrixelement^2*conv^2; %in SI
tripletreducedmattrixelement = tripletreducedmattrixelement^2*conv^2; %in SI
Jprime = 1;
Jprimeprime = 1;
I = 1/2;

prefector = (2*Fprime+1)*(2*Fprimeprime+1)*(-1)^(1+3*Fprimeprime+7*I+Jprimeprime+2*Jp

if S==0
    Sfactor = sqrt(2/3);
    mattrixelement = singletreducedmattrixelement;
elseif S==1
    Sfactor = 3/sqrt(6);
    mattrixelement = tripletreducedmattrixelement;
```

```
end

factor1 = w6j(Jprimeprime,1,Jprime,Fprime,I,Fprimeprime);

factor2 = w3j(I,-mF,1,n1,Fprimeprime,mFprimeprime);

factor3 = w3j(Fprimeprime,-mFprimeprime,1,nb,Fprime,mFprime);

factor4 = w3j(Fprime,-mFprime,1,n2,I,mF);


g = prefector*factor1*factor2*factor3*factor4*mattrixelement*Sfactor;
```

Appendix E

Beam Fluorescence

```
This code is written in Mathematica

Pow = 250; (*In uW, with 1MHz on*)

Temp = 435; (*In degrees C*)

SizeofFluorSignal = 200; (*In Smartcounts*)

DP = Integrate[Exp[\[Minus]t /420], {t, 0, 500}]/
   Integrate[Exp[\[Minus]t /420], {t, 0, \[Infinity]}] // N

0.695924

vbar = Sqrt[kB T / M]; FullSimplify[
 Integrate[
  v^3/(2 vbar^4) Exp[\[Minus]v^2/(2 vbar^2)]*1/v, {v,
   0, \[Infinity]}],
 Assumptions -> {Re[ M/(kB T)] > 0, M > 0, kB > 0, T > 0}]

1/2 Sqrt[\[Pi]/2] Sqrt[M/(kB T)]
```

```
FullSimplify[
 Integrate[(s0 / 2)/(1 + s0 +
     4 \[Delta]^2/\[Gamma]^2), {\[Delta], \[Minus]\[Infinity], \
\[Infinity]}], Assumptions -> {\[Gamma] > 0, s0 > 0}]

(\[Pi] s0 \[Gamma])/(4 Sqrt[1 + s0])

lorArea = (\[Pi] s0 \[Gamma])/(
  4 Sqrt[1 + s0]) /. {s0 -> Pow/220, \[Gamma] -> 1/ 420.*^-9}

1.45385*10^6

flArea = SizeofFluorSignal*Sqrt[\[Pi]/(1/(2 \[Pi]*1*^6*2*1.84366))^2]

8.21288*10^9

n0 = flArea/(QE * \[Eta] *IntTime *f *DP *lorArea *1/2*Len*
     Sqrt[\[Pi]*M/(2 kB T)]) /. {QE -> .1, M -> 226 *1.66*^-27,
   kB -> 1.38*^-23, T -> 273 + Temp, \[Eta] -> (1*^-2*.5), f -> 1*^6,
   IntTime -> .5, Len -> .003, s0 -> Pow/220}

2.78721*10^6

Flux = n0/.0012

2.32268*10^9
```

Bibliography

[1] C. S. Wu, E. Ambler, R. W. Hayward, D. D. Hoppes, and R. P. Hudson. Experimental test of parity conservation in beta decay. *Phys. Rev.*, 105:1413–1415, Feb 1957. doi: 10.1103/PhysRev.105.1413.

[2] Richard L. Garwin, Leon M. Lederman, and Marcel Weinrich. Observations of the failure of conservation of parity and charge conjugation in meson decays: the magnetic moment of the free muon. *Phys. Rev.*, 105:1415–1417, Feb 1957. doi: 10.1103/PhysRev.105.1415.

[3] L. Landau. On the conversation laws for weak interactions. *Nuclear Physics*, 3: 127–131, 1957.

[4] J. H. Christenson, J. W. Cronin, V. L. Fitch, and R. Turlay. Evidence for the 2π decay of the k_2^0 meson. *Phys. Rev. Lett.*, 13:138–140, Jul 1964. doi: 10.1103/PhysRevLett.13.138.

[5] James Marris. Cp violation and the dominance of matter. *Reviews in Undergraduate Research*, 1:38, 2002. URL http://www.ruf.rice.edu/~rur/issue1_files/PDF_Final/morris.pdf.

[6] A. Alavi-Harati, I. F. Albuquerque, T. Alexopoulos, M. Arenton, K. Arisaka, S. Averitte, A. R. Barker, L. Bellantoni, A. Bellavance, J. Belz, R. Ben-David, D. R. Bergman, E. Blucher, G. J. Bock, C. Bown, S. Bright, E. Cheu, S. Childress, R. Coleman, M. D. Corcoran, G. Corti, B. Cox, M. B. Crisler, A. R. Erwin, R. Ford, A. Glazov, A. Golossanov, G. Graham, J. Graham, K. Hagan, E. Halkiadakis, K. Hanagaki, S. Hidaka, Y. B. Hsiung, V. Jejer, J. Jennings, D. A. Jensen, R. Kessler, H. G. E. Kobrak, J. LaDue, A. Lath, A. Ledovskoy, P. L. McBride, A. P. McManus, P. Mikelsons, E. Monnier, T. Nakaya, U. Nauenberg, K. S. Nelson, H. Nguyen, V. O'Dell, M. Pang, R. Pordes, V. Prasad, C. Qiao,

B. Quinn, E. J. Ramberg, R. E. Ray, A. Roodman, M. Sadamoto, S. Schnetzer, K. Senyo, P. Shanahan, P. S. Shawhan, W. Slater, N. Solomey, S. V. Somalwar, R. L. Stone, I. Suzuki, E. C. Swallow, R. A. Swanson, S. A. Taegar, R. J. Tesarek, G. B. Thomson, P. A. Toale, A. Tripathi, R. Tschirhart, Y. W. Wah, J. Wang, H. B. White, J. Whitmore, B. Winstein, R. Winston, J.-Y. Wu, T. Yamanaka, and E. D. Zimmerman. Observation of direct cp violation in $k_{S,L} \to \pi\pi$ decays. *Phys. Rev. Lett.*, 83:22–27, Jul 1999. doi: 10.1103/PhysRevLett.83.22. URL http://link.aps.org/doi/10.1103/PhysRevLett.83.22.

[7] V. Fanti, A. Lai, D. Marras, L. Musa, A.J. Bevan, T.J. Gershon, B. Hay, R.W. Moore, K.N. Moore, D.J. Munday, M.D. Needham, M.A. Parker, S.F. Takach, T.O. White, S.A. Wotton, G. Barr, H. Blümer, G. Bocquet, J. Bremer, A. Ceccucci, J. Cogan, D. Cundy, N. Doble, W. Funk, L. Gatignon, A. Gianoli, A. Gonidec, G. Govi, P. Grafström, G. Kesseler, W. Kubischta, A. Lacourt, S. Luitz, J.P. Matheys, A. Norton, S. Palestini, B. Panzer-Steindel, B. Peyaud, D. Schinzel, H. Taureg, M. Velasco, O. Vossnack, H. Wahl, G. Wirrer, A. Gaponenko, V. Kekelidze, D. Madigojine, A. Mestvirishvili, Yu. Potrebenikov, G. Tatishvili, A. Tkatchev, A. Zinchenko, L. Bertolotto, O. Boyle, I.G. Knowles, V.J. Martin, H.L.C. Parsons, K.J. Peach, C. Talamonti, M. Contalbrigo, P. Dalpiaz, J. Duclos, A. Formica, P.L. Frabetti, M. Martini, F. Petrucci, M. Savrié, A. Bizzeti, M. Calvetti, G. Collazuol, G. Graziani, E. Iacopini, M. Lenti, A. Michetti, H.G. Becker, P. Buchholz, D. Coward, C. Ebersberger, H. Fox, A. Kalter, K. Kleinknecht, U. Koch, L. Köpke, B. Renk, J. Scheidt, J. Schmidt, V. Schönharting, Y. Schué, R. Wilhelm, M. Wittgen, J.C. Chollet, S. Crépé, L. Fayard, L. Iconomidou-Fayard, J. Ocariz, G. Unal, D. Vattolo, I. Wingerter-Seez, G. Anzivino, F. Bordacchini, P. Cenci, P. Lubrano, A. Nappi, M. Pepe, M. Punturo, L. Bertanza, A. Bigi, P. Calafiura, R. Carosi, R. Casali, C. Cerri, M. Cirilli, F. Costantini, R. Fantechi, S. Giudici, B. Gorini, I. Mannelli, V. Marzulli, G. Pierazzini, F. Raffaelli, M. Sozzi, J.B. Cheze, M. De Beer, P. Debu, R. Granier de Cassagnac, P. Hristov, E. Mazzucato, S. Schanne, R. Turlay, B. Vallage, I. Augustin, M. Bender, M. Holder, M. Ziolkowski, R. Arcidiacono, C. Biino, R. Cester, F. Marchetto, E. Menichetti, N. Pastrone, J. Nassalski, E. Rondio, M. Szleper, W. Wislicki, S. Wronka, H. Dibon, G. Fischer, M. Jeitler, M. Markytan, I. Mikulec, G. Neuhofer, M. Pernicka, and A. Taurok. A new measurement of direct cp violation in two

pion decays of the neutral kaon. *Physics Letters B*, 465(1–4):335 – 348, 1999. ISSN 0370-2693. doi: http://dx.doi.org/10.1016/S0370-2693(99)01030-8. URL http://www.sciencedirect.com/science/article/pii/S0370269399010308.

[8] Aubert, B et al. Observation of *CP* violation in the b^0 meson system. *Phys. Rev. Lett.*, 87:091801, Aug 2001. doi: 10.1103/PhysRevLett.87.091801.

[9] Abe, K et al. Observation of large *CP* violation in the neutral B meson system. *Phys. Rev. Lett.*, 87:091802, Aug 2001. doi: 10.1103/PhysRevLett.87.091802.

[10] Angelo Carbone. A search for time-integrated cp violation in $d^0 \to h^- h^+$ decays, 2012.

[11] A. Angelopoulos, A. Apostolakis, E. Aslanides, G. Backenstoss, P. Bargassa, O. Behnke, A. Benelli, V. Bertin, F. Blanc, P. Bloch, P. Carlson, M. Carroll, E. Cawley, S. Charalambous, M.B. Chertok, M. Danielsson, M. Dejardin, J. Derre, A. Ealet, C. Eleftheriadis, L. Faravel, W. Fetscher, M. Fidecaro, A. Filipčič, D. Francis, J. Fry, E. Gabathuler, R. Gamet, H.-J. Gerber, A. Go, A. Haselden, P.J. Hayman, F. Henry-Couannier, R.W. Hollander, K. Jon-And, P.-R. Kettle, P. Kokkas, R. Kreuger, R. Le Gac, F. Leimgruber, I. Mandić, N. Manthos, G. Marel, M. Mikuž, J. Miller, F. Montanet, A. Muller, T. Nakada, B. Pagels, I. Papadopoulos, P. Pavlopoulos, A. Policarpo, G. Polivka, R. Rickenbach, B.L. Roberts, T. Ruf, C. Santoni, M. Schäfer, L.A. Schaller, T. Schietinger, A. Schopper, L. Tauscher, C. Thibault, F. Touchard, C. Touramanis, C.W.E. Van Eijk, S. Vlachos, P. Weber, O. Wigger, M. Wolter, D. Zavrtanik, and D. Zimmerman. First direct observation of time-reversal non-invariance in the neutral-kaon system. *Physics Letters B*, 444(1–2):43 – 51, 1998. ISSN 0370-2693. doi: http://dx.doi.org/10.1016/S0370-2693(98)01356-2. URL http://www.sciencedirect.com/science/article/pii/S0370269398013562.

[12] J. P. Lees, V. Poireau, V. Tisserand, J. Garra Tico, E. Grauges, A. Palano, G. Eigen, B. Stugu, D. N. Brown, L. T. Kerth, Yu. G. Kolomensky, G. Lynch, H. Koch, T. Schroeder, D. J. Asgeirsson, C. Hearty, T. S. Mattison, J. A. McKenna, R. Y. So, A. Khan, V. E. Blinov, A. R. Buzykaev, V. P. Druzhinin, V. B. Golubev, E. A. Kravchenko, A. P. Onuchin, S. I. Serednyakov, Yu. I. Skovpen, E. P. Solodov, K. Yu. Todyshev, A. N. Yushkov, M. Bondioli, D. Kirkby, A. J. Lankford, M. Mandelkern, H. Atmacan, J. W. Gary, F. Liu, O. Long, G. M. Vitug, C. Campagnari,

T. M. Hong, D. Kovalskyi, J. D. Richman, C. A. West, A. M. Eisner, J. Kroseberg, W. S. Lockman, A. J. Martinez, B. A. Schumm, A. Seiden, D. S. Chao, C. H. Cheng, B. Echenard, K. T. Flood, D. G. Hitlin, P. Ongmongkolkul, F. C. Porter, A. Y. Rakitin, R. Andreassen, Z. Huard, B. T. Meadows, M. D. Sokoloff, L. Sun, P. C. Bloom, W. T. Ford, A. Gaz, U. Nauenberg, J. G. Smith, S. R. Wagner, R. Ayad, W. H. Toki, B. Spaan, K. R. Schubert, R. Schwierz, D. Bernard, M. Verderi, P. J. Clark, S. Playfer, D. Bettoni, C. Bozzi, R. Calabrese, G. Cibinetto, E. Fioravanti, I. Garzia, E. Luppi, M. Munerato, L. Piemontese, V. Santoro, R. Baldini-Ferroli, A. Calcaterra, R. de Sangro, G. Finocchiaro, P. Patteri, I. M. Peruzzi, M. Piccolo, M. Rama, A. Zallo, R. Contri, E. Guido, M. Lo Vetere, M. R. Monge, S. Passaggio, C. Patrignani, E. Robutti, B. Bhuyan, V. Prasad, C. L. Lee, M. Morii, A. J. Edwards, A. Adametz, U. Uwer, H. M. Lacker, T. Lueck, P. D. Dauncey, U. Mallik, C. Chen, J. Cochran, W. T. Meyer, S. Prell, A. E. Rubin, A. V. Gritsan, Z. J. Guo, N. Arnaud, M. Davier, D. Derkach, G. Grosdidier, F. Le Diberder, A. M. Lutz, B. Malaescu, P. Roudeau, M. H. Schune, A. Stocchi, G. Wormser, D. J. Lange, D. M. Wright, C. A. Chavez, J. P. Coleman, J. R. Fry, E. Gabathuler, D. E. Hutchcroft, D. J. Payne, C. Touramanis, A. J. Bevan, F. Di Lodovico, R. Sacco, M. Sigamani, G. Cowan, D. N. Brown, C. L. Davis, A. G. Denig, M. Fritsch, W. Gradl, K. Griessinger, A. Hafner, E. Prencipe, R. J. Barlow, G. Jackson, G. D. Lafferty, E. Behn, R. Cenci, B. Hamilton, A. Jawahery, D. A. Roberts, C. Dallapiccola, R. Cowan, D. Dujmic, G. Sciolla, R. Cheaib, D. Lindemann, P. M. Patel, S. H. Robertson, P. Biassoni, N. Neri, F. Palombo, S. Stracka, L. Cremaldi, R. Godang, R. Kroeger, P. Sonnek, D. J. Summers, X. Nguyen, M. Simard, P. Taras, G. De Nardo, D. Monorchio, G. Onorato, C. Sciacca, M. Martinelli, G. Raven, C. P. Jessop, J. M. LoSecco, W. F. Wang, K. Honscheid, R. Kass, J. Brau, R. Frey, N. B. Sinev, D. Strom, E. Torrence, E. Feltresi, N. Gagliardi, M. Margoni, M. Morandin, A. Pompili, M. Posocco, M. Rotondo, G. Simi, F. Simonetto, R. Stroili, S. Akar, E. Ben-Haim, M. Bomben, G. R. Bonneaud, H. Briand, G. Calderini, J. Chauveau, O. Hamon, Ph. Leruste, G. Marchiori, J. Ocariz, S. Sitt, M. Biasini, E. Manoni, S. Pacetti, A. Rossi, C. Angelini, G. Batignani, S. Bettarini, M. Carpinelli, G. Casarosa, A. Cervelli, F. Forti, M. A. Giorgi, A. Lusiani, B. Oberhof, E. Paoloni, A. Perez, G. Rizzo, J. J. Walsh, D. Lopes Pegna, J. Olsen, A. J. S. Smith, A. V. Telnov, F. Anulli, R. Faccini, F. Ferrarotto, F. Ferroni, M. Gaspero, L. Li Gioi, M. A. Mazzoni, G. Piredda, C. Bünger,

O. Grünberg, T. Hartmann, T. Leddig, H. Schröder, C. Voss, R. Waldi, T. Adye, E. O. Olaiya, F. F. Wilson, S. Emery, G. Hamel de Monchenault, G. Vasseur, Ch. Yèche, D. Aston, D. J. Bard, R. Bartoldus, J. F. Benitez, C. Cartaro, M. R. Convery, J. Dorfan, G. P. Dubois-Felsmann, W. Dunwoodie, M. Ebert, R. C. Field, M. Franco Sevilla, B. G. Fulsom, A. M. Gabareen, M. T. Graham, P. Grenier, C. Hast, W. R. Innes, M. H. Kelsey, P. Kim, M. L. Kocian, D. W. G. S. Leith, P. Lewis, B. Lindquist, S. Luitz, V. Luth, H. L. Lynch, D. B. MacFarlane, D. R. Muller, H. Neal, S. Nelson, M. Perl, T. Pulliam, B. N. Ratcliff, A. Roodman, A. A. Salnikov, R. H. Schindler, A. Snyder, D. Su, M. K. Sullivan, J. Va'vra, A. P. Wagner, W. J. Wisniewski, M. Wittgen, D. H. Wright, H. W. Wulsin, C. C. Young, V. Ziegler, W. Park, M. V. Purohit, R. M. White, J. R. Wilson, A. Randle-Conde, S. J. Sekula, M. Bellis, P. R. Burchat, T. S. Miyashita, E. M. T. Puccio, M. S. Alam, J. A. Ernst, R. Gorodeisky, N. Guttman, D. R. Peimer, A. Soffer, P. Lund, S. M. Spanier, J. L. Ritchie, A. M. Ruland, R. F. Schwitters, B. C. Wray, J. M. Izen, X. C. Lou, F. Bianchi, D. Gamba, S. Zambito, L. Lanceri, L. Vitale, J. Bernabeu, F. Martinez-Vidal, A. Oyanguren, P. Villanueva-Perez, H. Ahmed, J. Albert, Sw. Banerjee, F. U. Bernlochner, H. H. F. Choi, G. J. King, R. Kowalewski, M. J. Lewczuk, I. M. Nugent, J. M. Roney, R. J. Sobie, N. Tasneem, T. J. Gershon, P. F. Harrison, T. E. Latham, H. R. Band, S. Dasu, Y. Pan, R. Prepost, and S. L. Wu. Observation of time-reversal violation in the B^0 meson system. *Phys. Rev. Lett.*, 109:211801, Nov 2012. doi: 10.1103/PhysRevLett.109.211801. URL http://link.aps.org/doi/10.1103/PhysRevLett.109.211801.

[13] E. M. Purcell and N. F. Ramsey. On the possibility of electric dipole moments for elementary particles and nuclei. *Phys. Rev.*, 78:807–807, Jun 1950. doi: 10.1103/PhysRev.78.807.

[14] J. H. Smith, E. M. Purcell, and N. F. Ramsey. Experimental limit to the electric dipole moment of the neutron. *Phys. Rev.*, 108:120–122, Oct 1957. doi: 10.1103/PhysRev.108.120. URL http://link.aps.org/doi/10.1103/PhysRev.108.120.

[15] C. Baker, D. Doyle, P. Geltenbort, K. Green, M. van der Grinten, P. Harris, P. Iaydjiev, S. Ivanov, D. May, J. Pendlebury, J. Richardson, D. Shiers, and K. Smith. Improved experimental limit on the electric dipole moment of the neutron. *Phys. Rev. Lett.*, 97:131801, Sep 2006. doi: 10.1103/PhysRevLett.97.131801. URL http://link.aps.org/doi/10.1103/PhysRevLett.97.131801.

[16] T. S. Stein, J. P. Carrico, E. Lipworth, and M. C. Weisskopf. Permanent electric dipole moment of the cesium atom. an upper limit to the electric dipole moment of the electron. *Phys. Rev.*, 186:39–51, Oct 1969. doi: 10.1103/PhysRev.186.39. URL http://link.aps.org/doi/10.1103/PhysRev.186.39.

[17] B. C. Regan, Eugene D. Commins, Christian J. Schmidt, and David DeMille. New limit on the electron electric dipole moment. *Phys. Rev. Lett.*, 88:071805, Feb 2002. doi: 10.1103/PhysRevLett.88.071805. URL http://link.aps.org/doi/10.1103/PhysRevLett.88.071805.

[18] J. J. Hudson, D. M. Kara, I. J. Smallman, B. E. Sauer, M. R. Tarbutt, and E. A. Hinds. Improved measurement of the shape of the electron. *Nature*, 473(7348): 493–496, 2011. URL http://dx.doi.org/10.1038/nature10104.

[19] Y J Kim, C-Y Liu, S K Lamoreaux, and G Reddy. Experimental search for the electron electric dipole moment using solid state techniques. *Journal of Physics: Conference Series*, 312(10):102009, 2011. URL http://stacks.iop.org/1742-6596/312/i=10/a=102009.

[20] The ACME Collaboration, J. Baron, W. C. Campbell, D. DeMille, J. M. Doyle, G. Gabrielse, Y. V. Gurevich, P. W. Hess, N. R. Hutzler, E. Kirilov, I. Kozyryev, B. R. O'Leary, C. D. Panda, M. F. Parsons, E. S. Petrik, B. Spaun, A. C. Vutha, and A. D. West. Order of magnitude smaller limit on the electric dipole moment of the electron. *Science*, 343(6168):269–272, 2014. doi: 10.1126/science.1248213. URL http://www.sciencemag.org/content/343/6168/269.abstract.

[21] M. Swallows, T. Loftus, W. Griffith, B. Heckel, E. Fortson, and M. Romalis. Techniques used to search for a permanent electric dipole moment of the ^{199}hg atom and the implications for *CP* violation. *Phys. Rev. A*, 87:012102, Jan 2013. doi: 10.1103/PhysRevA.87.012102. URL http://link.aps.org/doi/10.1103/PhysRevA.87.012102.

[22] V. F. Dmitriev and R. A. Sen'kov. Schiff moment of the mercury nucleus and the proton dipole moment. *Phys. Rev. Lett.*, 91:212303, Nov 2003. doi: 10.1103/PhysRevLett.91.212303. URL http://link.aps.org/doi/10.1103/PhysRevLett.91.212303.

[23] G. Bennett et al. Improved limit on the muon electric dipole moment. *Phys. Rev. D*, 80:052008, Sep 2009. doi: 10.1103/PhysRevD.80.052008. URL http://link.aps.org/doi/10.1103/PhysRevD.80.052008.

[24] K. Inami, K. Abe, K. Abe, R. Abe, T. Abe, I. Adachi, H. Aihara, M. Akatsu, Y. Asano, T. Aso, V. Aulchenko, T. Aushev, A.M. Bakich, Y. Ban, E. Banas, P.K. Behera, I. Bizjak, A. Bondar, T.E. Browder, P. Chang, Y. Chao, B.G. Cheon, R. Chistov, Y. Choi, Y.K. Choi, L.Y. Dong, S. Eidelman, V. Eiges, Y. Enari, C. Fukunaga, N. Gabyshev, A. Garmash, T. Gershon, B. Golob, C. Hagner, F. Handa, T. Hara, H. Hayashii, M. Hazumi, I. Higuchi, T. Higuchi, T. Hokuue, Y. Hoshi, W.-S. Hou, H.-C. Huang, T. Igaki, T. Iijima, A. Ishikawa, H. Ishino, R. Itoh, H. Iwasaki, H.K. Jang, J.H. Kang, J.S. Kang, N. Katayama, H. Kawai, Y. Kawakami, N. Kawamura, T. Kawasaki, H. Kichimi, H.O. Kim, Hyunwoo Kim, J.H. Kim, S.K. Kim, S. Korpar, P. Krokovny, R. Kulasiri, A. Kuzmin, Y.-J. Kwon, J.S. Lange, G. Leder, S.H. Lee, J. Li, D. Liventsev, R.-S. Lu, J. MacNaughton, F. Mandl, T. Matsuishi, S. Matsumoto, T. Matsumoto, W. Mitaroff, H. Miyake, H. Miyata, T. Nagamine, Y. Nagasaka, T. Nakadaira, E. Nakano, M. Nakao, J.W. Nam, S. Nishida, T. Nozaki, S. Ogawa, T. Ohshima, T. Okabe, S. Okuno, S.L. Olsen, W. Ostrowicz, H. Ozaki, P. Pakhlov, H. Park, K.S. Park, L.S. Peak, J.-P. Perroud, L.E. Piilonen, K. Rybicki, H. Sagawa, S. Saitoh, Y. Sakai, M. Satapathy, O. Schneider, S. Semenov, K. Senyo, M.E. Sevior, H. Shibuya, B. Shwartz, V. Sidorov, J.B. Singh, N. Soni, S. Stanič, M. Starič, A. Sugi, A. Sugiyama, K. Sumisawa, T. Sumiyoshi, S. Suzuki, S.Y. Suzuki, T. Takahashi, F. Takasaki, K. Tamai, N. Tamura, J. Tanaka, M. Tanaka, G.N. Taylor, Y. Teramoto, S. Tokuda, T. Tomura, T. Tsuboyama, T. Tsukamoto, S. Uehara, Y. Unno, S. Uno, G. Varner, K.E. Varvell, C.C. Wang, Y. Watanabe, B.D. Yabsley, Y. Yamada, A. Yamaguchi, Y. Yamashita, Y. Yusa, Z.P. Zhang, V. Zhilich, and D. Žontar. Search for the electric dipole moment of the τ lepton. *Physics Letters B*, 551(1–2):16 – 26, 2003. ISSN 0370-2693. doi: http://dx.doi.org/10.1016/S0370-2693(02)02984-2. URL http://www.sciencedirect.com/science/article/pii/S0370269302029842.

[25] L. Pondrom, R. Handler, M. Sheaff, P. T. Cox, J. Dworkin, O. E. Overseth, T. Devlin, L. Schachinger, and K. Heller. New limit on the electric dipole moment of the λ hyperon. *Phys. Rev. D*, 23:814–816, Feb 1981. doi: 10.1103/PhysRevD.23.814. URL http://link.aps.org/doi/10.1103/PhysRevD.23.814.

[26] F. del Aguila and Marc Sher. The electric dipole moment of the tau. *Physics Letters B*, 252(1):116 – 118, 1990. ISSN 0370-2693. doi: http://dx.doi.org/10.1016/0370-2693(90)91091-O. URL http://www.sciencedirect.com/science/article/pii/037026939091091O.

[27] Tarek Ibrahim and Pran Nath. Large tau and tau neutrino electric dipole moments in models with vectorlike multiplets. *Phys. Rev. D*, 81:033007, Feb 2010. doi: 10.1103/PhysRevD.81.033007. URL http://link.aps.org/doi/10.1103/PhysRevD.81.033007.

[28] L. Schiff. Measurability of nuclear electric dipole moments. *Phys. Rev.*, 132:2194–2200, Dec 1963. doi: 10.1103/PhysRev.132.2194. URL http://link.aps.org/doi/10.1103/PhysRev.132.2194.

[29] J. Engel, J. L. Friar, and A. C. Hayes. Nuclear octupole correlations and the enhancement of atomic time-reversal violation. *Phys. Rev. C*, 61:035502, Feb 2000. doi: 10.1103/PhysRevC.61.035502. URL http://link.aps.org/doi/10.1103/PhysRevC.61.035502.

[30] J.S.M. Ginges and V.V. Flambaum. Violations of fundamental symmetries in atoms and tests of unification theories of elementary particles. *Physics Reports*, 397(2):63 – 154, 2004. ISSN 0370-1573. doi: http://dx.doi.org/10.1016/j.physrep.2004.03.005. URL http://www.sciencedirect.com/science/article/pii/S0370157304001322.

[31] P. A. Butler and W. Nazarewicz. Intrinsic reflection asymmetry in atomic nuclei. *Rev. Mod. Phys.*, 68:349–421, Apr 1996. doi: 10.1103/RevModPhys.68.349. URL http://link.aps.org/doi/10.1103/RevModPhys.68.349.

[32] P. Moller, J.R. Nix, W.D. Myers, and W.J. Swiatecki. Nuclear ground-state masses and deformations. *Atomic Data and Nuclear Data Tables*, 59(2):185 – 381, 1995. ISSN 0092-640X. doi: http://dx.doi.org/10.1006/adnd.1995.1002. URL http://www.sciencedirect.com/science/article/pii/S0092640X85710029.

[33] R.G. Helmer, M.A. Lee, C.W. Reich, and I. Ahmad. Intrinsic reflection asymmetry in 225ra: Additional information from a study of the α-decay scheme of 229th. *Nuclear Physics A*, 474(1):77 – 113, 1987. ISSN 0375-9474. doi: http://dx.doi.org/

10.1016/0375-9474(87)90195-3. URL http://www.sciencedirect.com/science/article/pii/0375947487901953.

[34] M.A. Preston and R.K. Bhaduri. Structure of the nucleus. *Addison-Wesley Publishing Company*, 1975.

[35] Ibrahim Sulai. *PRECISION SPECTROSCOPY OF LASER TRAPPED HELIUM AND RADIUM ATOMS*. PhD thesis, University of Chicago, Chicago, USA, 2011.

[36] Jonathan Engel, Michael J. Ramsey-Musolf, and U. van Kolck. Electric dipole moments of nucleons, nuclei, and atoms: The standard model and beyond. *Progress in Particle and Nuclear Physics*, 71(0):21 – 74, 2013. ISSN 0146-6410. doi: http://dx.doi.org/10.1016/j.ppnp.2013.03.003. URL http://www.sciencedirect.com/science/article/pii/S0146641013000227. Fundamental Symmetries in the Era of the {LHC}.

[37] V. Dzuba, V. Flambaum, J. Ginges, and M. Kozlov. Electric dipole moments of hg, xe, rn, ra, pu, and tlf induced by the nuclear schiff moment and limits on time-reversal violating interactions. *Phys. Rev. A*, 66:012111, Jul 2002. doi: 10.1103/PhysRevA.66.012111. URL http://link.aps.org/doi/10.1103/PhysRevA.66.012111.

[38] J. R. Guest, N. D. Scielzo, I. Ahmad, K. Bailey, J. P. Greene, R. J. Holt, Z.-T. Lu, T. P. O'Connor, and D. H. Potterveld. Laser trapping of ^{225}Ra and ^{226}Ra with repumping by room-temperature blackbody radiation. *Phys. Rev. Lett.*, 98:093001, Feb 2007. doi: 10.1103/PhysRevLett.98.093001. URL http://link.aps.org/doi/10.1103/PhysRevLett.98.093001.

[39] J. Bieroń, P. Indelicato, and P. Jönsson. Multiconfiguration dirac-hartree-fock calculations of transition rates and lifetimes of the eight lowest excited levels of radium. *The European Physical Journal Special Topics*, 144(1):75–84, 2007. ISSN 1951-6355. doi: 10.1140/epjst/e2007-00110-3. URL http://dx.doi.org/10.1140/epjst/e2007-00110-3.

[40] Eric D. Black. An introduction to pound–drever–hall laser frequency stabilization. *American Journal of Physics*, 69(1), 2001.

[41] Evan lally. *A Narrow-Linewidth Laser at 1550 nm Using the Pound-Drever-Hall Stabilization Technique*. PhD thesis, Virginia Polytechnic Institute and State University, Virginia, USA, 2006.

[42] H.J. Metcalf and P. van der Straten. *Laser Cooling and Trapping*. Graduate Texts in Contemporary Physics. Springer New York, 1999. ISBN 9780387987286. URL http://books.google.com/books?id=i-40VaXqrj0C.

[43] G. Scoles. *Atomic and Molecular Beam Methods*. Number v. 1 in Atomic and Molecular Beam Methods. Oxford University Press, 1988. ISBN 9780195042801. URL http://books.google.com/books?id=uEeyQgAACAAJ.

[44] C. Tuchendler, A. M. Lance, A. Browaeys, Y. R. P. Sortais, and P. Grangier. Energy distribution and cooling of a single atom in an optical tweezer. *Phys. Rev. A*, 78: 033425, Sep 2008. doi: 10.1103/PhysRevA.78.033425. URL http://link.aps.org/doi/10.1103/PhysRevA.78.033425.

[45] M. E. Gehm, K. M. O'Hara, T. A. Savard, and J. E. Thomas. Dynamics of noise-induced heating in atom traps. *Phys. Rev. A*, 58:3914–3921, Nov 1998. doi: 10.1103/PhysRevA.58.3914. URL http://link.aps.org/doi/10.1103/PhysRevA.58.3914.

[46] V A Dzuba and V V Flambaum. Calculation of energy levels and transition amplitudes for barium and radium. *Journal of Physics B: Atomic, Molecular and Optical Physics*, 40(1):227, 2007. URL http://stacks.iop.org/0953-4075/40/i=1/a=021.

[47] V. A. Dzuba. Private communications.

[48] R. Parker, M. Dietrich, K. Bailey, J. Greene, R. Holt, M. Kalita, W. Korsch, Z.-T. Lu, P. Mueller, T. O'Connor, J. Singh, I. Sulai, and W. Trimble. Efficient, tightly-confined trapping of ^{226}ra. *Phys. Rev. C*, 86:065503, Dec 2012. doi: 10.1103/PhysRevC.86.065503. URL http://link.aps.org/doi/10.1103/PhysRevC.86.065503.

[49] Jaideep Singh. *Alkali-Hybrid Spin-Exchange Optically-Pumped Polarized 3He Targets Used for Studying Neutron Structure*. PhD thesis, University of virginia, Virginia, USA, 2010.

[50] C. Ockeloen, A. Tauschinsky, R. Spreeuw, and S. Whitlock. Detection of small atom numbers through image processing. *Phys. Rev. A*, 82:061606, Dec 2010. doi: 10.1103/PhysRevA.82.061606. URL http://link.aps.org/doi/10.1103/PhysRevA.82.061606.

[51] M. Romalis and E. Fortson. Zeeman frequency shifts in an optical dipole trap used to search for an electric-dipole moment. *Phys. Rev. A*, 59:4547–4558, Jun 1999. doi: 10.1103/PhysRevA.59.4547. URL http://link.aps.org/doi/10.1103/PhysRevA.59.4547.

[52] J. M. Pendlebury, W. Heil, Yu. Sobolev, P. G. Harris, J. D. Richardson, R. J. Baskin, D. D. Doyle, P. Geltenbort, K. Green, M. G. D. van der Grinten, P. S. Iaydjiev, S. N. Ivanov, D. J. R. May, and K. F. Smith. Geometric-phase-induced false electric dipole moment signals for particles in traps. *Phys. Rev. A*, 70:032102, Sep 2004. doi: 10.1103/PhysRevA.70.032102. URL http://link.aps.org/doi/10.1103/PhysRevA.70.032102.

[53] Timothy Chupp and Michael Ramsey-Musolf. Electric dipole moments: A global analysis, 2014.

[54] Timothy Chupp. *University of Michigan, private communication.*

[55] F. Le Pimpec, R. Ganter, and R. Betemps. Field emission dark current of technical metallic electrodes. *Nuclear Instruments and Methods in Physics Research Section A: Accelerators, Spectrometers, Detectors and Associated Equipment*, 574(1):7 – 16, 2007. ISSN 0168-9002. doi: http://dx.doi.org/10.1016/j.nima.2007.01.087. URL http://www.sciencedirect.com/science/article/pii/S0168900207001209.

[56] K. Bergmann, H. Theuer, and B. Shore. Coherent population transfer among quantum states of atoms and molecules. *Rev. Mod. Phys.*, 70:1003–1025, Jul 1998. doi: 10.1103/RevModPhys.70.1003. URL http://link.aps.org/doi/10.1103/RevModPhys.70.1003.

[57] V.I. Romanenko and L.P. Yatsenko. Adiabatic population transfer in the three-level lambda-system: two-photon lineshape. *Optics Communications*, 140(4–6):231 – 236, 1997. ISSN 0030-4018. doi: http://dx.doi.org/10.1016/S0030-4018(97)00152-1. URL http://www.sciencedirect.com/science/article/pii/S0030401897001521.

[58] A. B. Balantekin, J. Carlson, D. J. Dean, G. M. Fuller, R. J. Furnstahl, M. Hjorth-Jensen, R. V. F. Janssens, Bao-An Li, W. Nazarewicz, F. M. Nunes, W. E. Ormand, S. Reddy, and B. M. Sherrill. Nuclear theory and science of the facility for rare isotope beams. *Modern Physics Letters A*, 29(11):1430010, 2014. doi: 10.1142/S0217732314300109.

[59] D. M. Asner, P. C. Bhat, S. Henderson, R. Plunkett, D. W. Wootan, M. A. Peterson, D. Senor, R. Tschirhart, A. Grasselino, A. Romanenko, G. MacDougall, and R. H. Heffner. Project X: Broader Impacts, 2013.